Land Cover Change, Vegetation Dynamics and the Global Carbon Cycle: Experiments with the UVic Earth System Climate Model

by

H. Damon Matthews
B.Sc., Simon Fraser University, 1999

A Dissertation Submitted in Partial Fulfillment of the
Requirements for the Degree of

Doctor of Philosophy

in the School of Earth and Ocean Sciences

University of Victoria

Supervisor: Dr. A. J. Weaver

Abstract

This thesis explores the role of terrestrial vegetation in the global climate system in a series of modelling studies using the University of Victoria Earth System Climate Model (UVic ESCM). The ways that vegetation affects climate, as well as the feedbacks that operate between changing climate and vegetation distributions, are investigated within the framework of three foci: 1) historical land cover changes that have resulted from human modification of natural vegetation cover; 2) historical land cover change and the dynamics of terrestrial vegetation in the context of anthropogenic and natural climate change; and 3) the role of terrestrial vegetation in the global carbon cycle.

First, the radiative effect of changing human land-use patterns on the climate of the past 300 years is discussed through analysis of a series of equilibrium and transient climate simulations using the UVic ESCM. These experiments highlight the biogeophysical effects of historical land cover change on climate: those that result from physical changes to the land surface under altered vegetation cover. Results show a global cooling in the range of –0.06 to –0.22 °C, though this effect is not found to be detectable in observed temperature trends. Using a global carbon cycle the climatic effects of land cover change emissions (the biogeochemical effect of historical land cover change) are assessed. The resultant warming is found to exceed the biogeophysical cooling by 0.15 °C.

Second, the effect of historical land cover change is compared with the effects of natural forcings (volcanic aerosols, solar insolation variability and orbital changes) and other anthropogenic forcings (greenhouse gases and sulphate aerosols). Transient model runs from the year 1700 to 2000 are presented for each forcing individually as well as for combinations of forcings. I find that the UVic model reproduces well the global temperature data when all forcings are included. In the context of these anthropogenic and natural climate influences, the response of vegetation distributions to changing climate is explored through the use of a dynamic global vegetation model coupled interactively to the UVic ESCM. Transient simulations of the past 300 years are repeated using this new model so as to isolate the biogeophysical feedbacks that operate between vegetation and climate. Dynamic vegetation is found to act as a positive feedback to climate, amplifying both warming and cooling climate trends.

Third, the development of a global carbon cycle model allows for investigation of the role of terrestrial carbon cycle dynamics under past and future climate change. When forced by historical emissions of CO_2 from fossil fuels and land-use change, the coupled carbon cycle model accurately reproduces historical atmospheric CO_2 trends, as well as terrestrial and oceanic uptake for the past two decades. Under six 21^{st} century CO_2 emissions scenarios, both terrestrial and oceanic carbon sinks continue to increase, though terrestrial uptake slows in the latter half of the century. The modelled positive feedback between the carbon cycle and climate is relatively small, resulting in an increase in simulated CO_2 of 60 ppmv at the year 2100. Including non-CO_2 greenhouse gas forcing and increasing the model's climate sensitivity increases the effect of this feedback to 140 ppmv. The UVic model does not, however, simulate a switch from a terrestrial carbon sink to a source during the 21^{st} century, as earlier studies have suggested. This can be explained by a lack of substantial reductions in simulated vegetation productivity due to climate changes.

Table of Contents

List of Tables

List of Figures

Acknowledgements

I would like to extend my sincere thanks to my supervisor, Dr. Andrew Weaver. I am very grateful for his availability and support in developing my graduate programme and research objectives and for his superior guidance and mentorship. I would also like to gratefully acknowledge my committee members, Norm McFarlane, Greg Flato and Nigel Livingston as well as Vivek Arora and Katrin Meissner, for their thoughtful commentary on my research and dissertation.

Special thanks to Michael Eby, Ed Wiebe, Mike Roth, Tracy Ewen, Nathan Gillett, Daithi Stone, Jeff Lewis, Hannah Hickey, Jackie Dumas and Wanda Lewis for ongoing assistance with the various modelling, programming, computing, scientific and administrative challenges that I have encountered over the course of my studies. I am also grateful to Andrew Weaver, Katrin Meissner, Shawn Marshall and Francis Zwiers for their time and contributions to my numerous funding and university applications.

I really appreciate my family for their support and encouragement of my academic pursuits and for occasional lunches, childcare, editing and squash games along the way; my deep thanks to Kathleen, Wayne, Blake and Quinn Matthews, Winifred Matthews (in memory), Paula Ramsay, Jane Chapman, Nancy, Bob, Molly, Kate and Isabella Turner, and Jan and Dave Renfroe. I would particularly like to thank Sarah Turner for always being there and for being wonderfully supportive of my studies, as well as Shea Turner-Matthews for his understanding of my occasional absences and for the recent inspiration he has brought into my life.

Funding for this research has come from the from National Science and Engineering Research Council (NSERC) Post-Graduate Scholarships Programme, the University of Victoria David F. Strong, Howard E. Petch and President's Research Scholarships, the Edward Bassett Family Scholarship, the Climate Variability and Predictability Research Program (CLIVAR), and the Canadian Foundation for Climate and Atmospheric Studies (CFCAS).

~

I would like to dedicate this work to my parents

~

Chapter 1

Introduction

1.1 The Science of Climate Change

In 1996, the Intergovernmental Panel on Climate Change (IPCC) published its Second Assessment Report on the state of climate change science around the world. In the opening pages was the following statement representing a consensus opinion from the world's climate scientists:

> The balance of evidence suggests a discernible human influence on global climate (Houghton et al. 1996, p. 4).

This remarkable statement was strengthened five years later when the Third Assessment Report was released:

> There is new and stronger evidence that most of the warming observed over the last 50 years is attributable to human activities (Houghton et al. 2001, p. 10).

These statements form a clear message of the growing scientific understanding of climate change and the profound influence that human activities are having on the climate system. Instrumental records of temperature (shown in Figure 1.1a) over the past 150 years have documented a global temperature increase of 0.6 ± 0.2 °C since the beginning of the industrial revolution. Careful measurements of important atmospheric trace gases have shown a parallel increase in atmospheric concentrations of greenhouse gases such as carbon dioxide (CO_2), methane (CH_4) and nitrous oxide (N_2O). Figure 1.2 shows historical measurements of these gases compared to reconstructed estimates of their concentrations over the past 1000 years. In all cases, recent measurements show substantial increases over stable pre-industrial conditions.

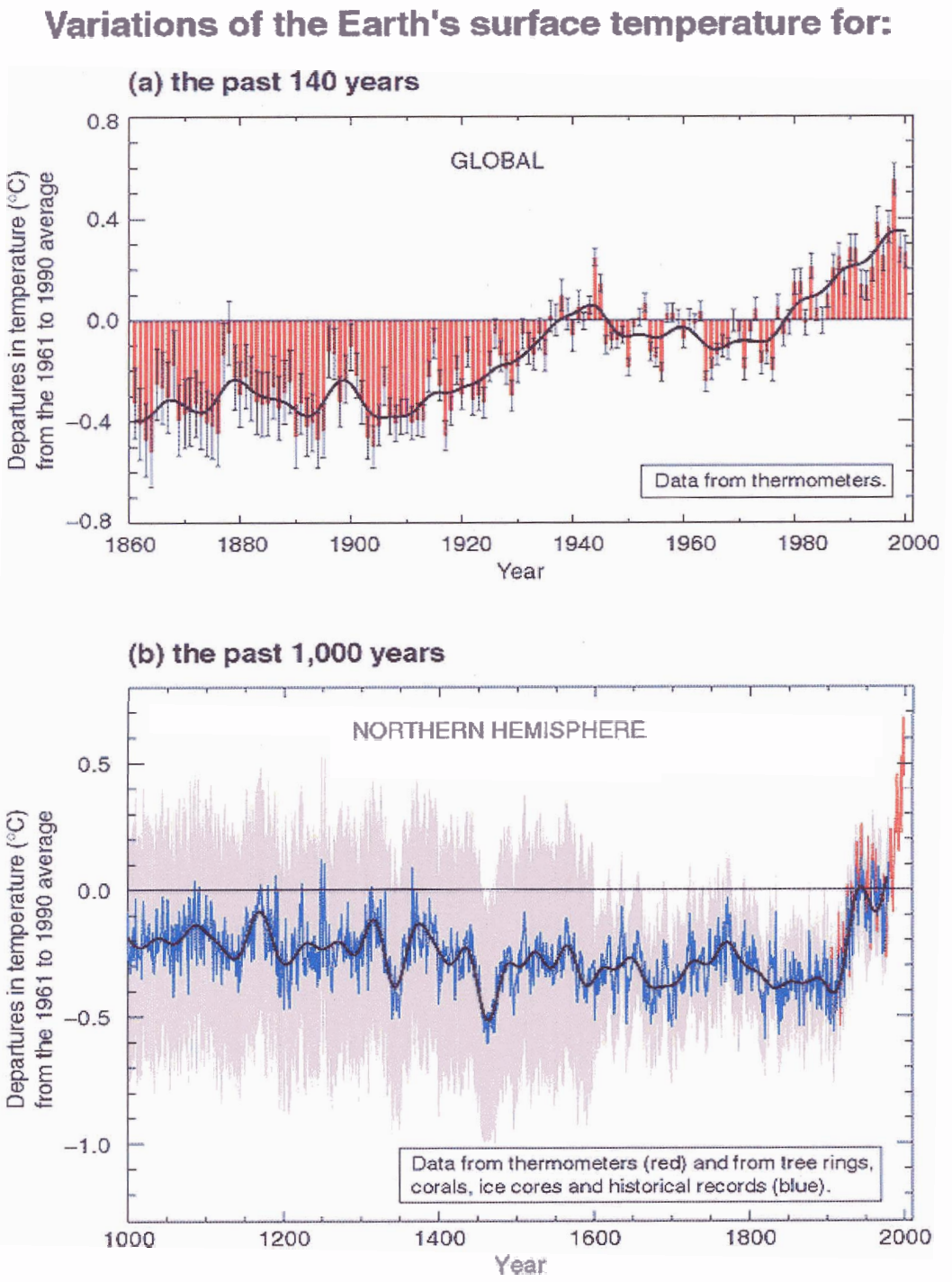

Figure 1.1: (a) Global temperature change from instrumental records and (b) Northern hemisphere temperature from proxy record reconstruction. Reprinted from Houghton et al. (2001, Summary for Policymakers, Figure 1).

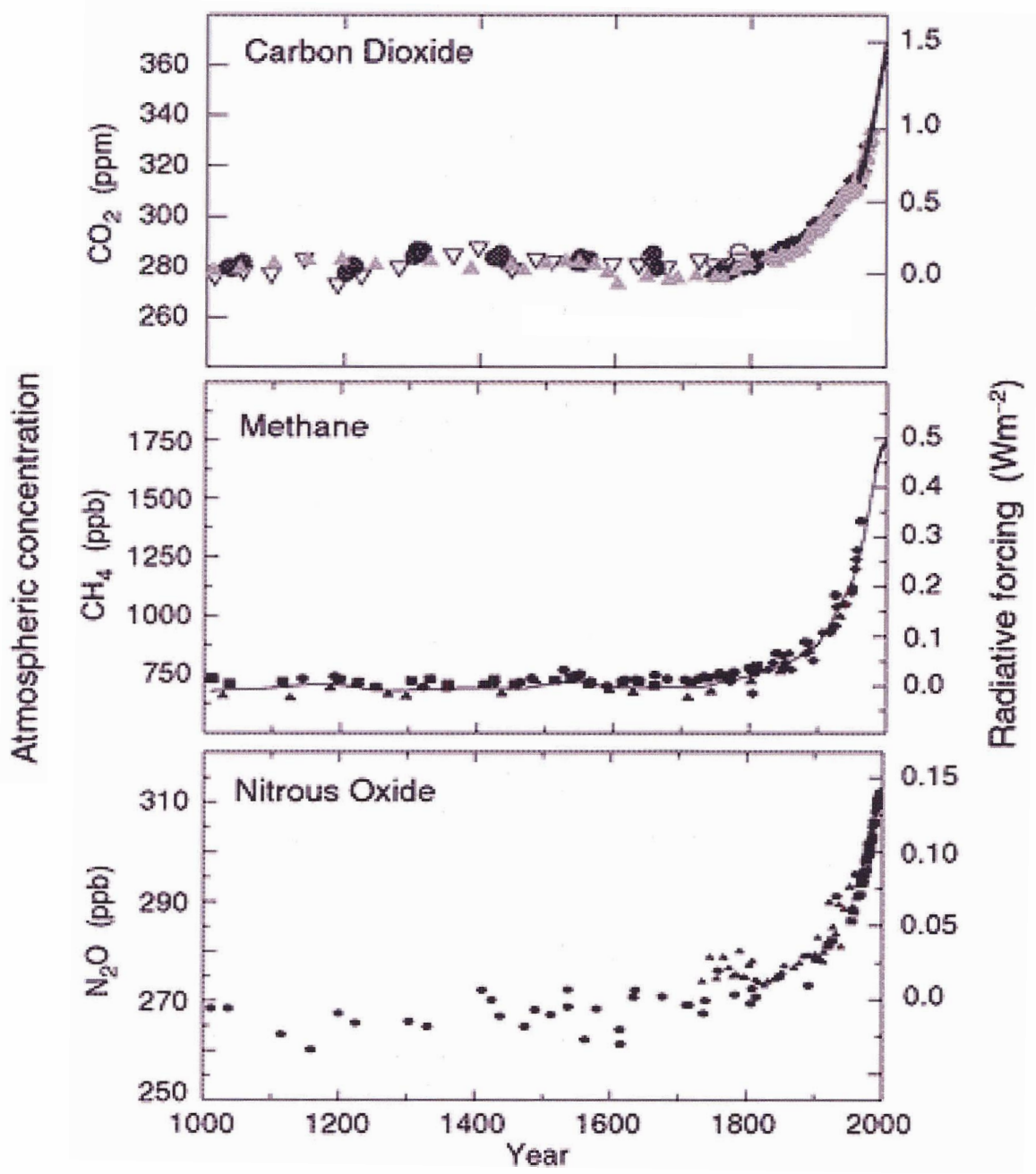

Figure 1.2: Recent measured trends in the atmospheric concentration of carbon dioxide, methane and nitrous oxide, superimposed on reconstructed estimates for the past 1000 years. Reprinted from Houghton et al. (2001, Summary for Policymakers, Figure 2).

Reconstructions of historical temperature and greenhouse gas records from climate proxies, such as tree rings, coral and ice cores, have shown that recent trends are a distinct anomaly. Mann et al.'s (1999) reconstruction (shown in Figure 1.1b) showed that recent Northern hemisphere mean surface temperatures exceed any that have occurred in the past 1000 years. Mann and Jones (2003) presented evidence that this conclusion may also hold for the past 2000 years. Longer records extracted from ice cores (see for example Petit et al. 1999) show that temperature and greenhouse gas changes have been tightly correlated for a least the last 400,000 years, a period that covers four glacial cycles. As shown in Figure 1.3, CO_2 concentrations have varied between 200 and 300 ppm across glacial-interglacial cycles, with methane also varying between about 400 and 700 ppb. This reconstruction revealed that current concentrations of CO_2 (370 ppm) and methane (1700 ppb) far exceed any that have occurred over this time span and this suggests that global temperatures are likely to continue to increase in response to current greenhouse gas levels.

It is well known that radiatively active gases (so-called greenhouse gases: CO_2, methane, nitrous oxide, halocarbons and tropospheric ozone) affect the global radiative budget by absorbing and re-emitting some amount of the outgoing longwave radiation emitted by the Earth's surface. The effect of radiatively active gases on the climate system can be described by the concept of *radiative forcing*, defined in the IPCC Second Assessment Report as:

> The radiative forcing of the surface-troposphere system due to the perturbation in or the introduction of an agent (say a change in greenhouse gas concentrations) is the change in net (down minus up) irradiance (solar plus long-wave; in Wm^{-2}) at the tropopause after allowing for stratospheric temperatures to readjust to radiative equilibrium but with surface and tropospheric temperatures and state held fixed at the unperturbed values (Ramaswamy et al. 2001, p. 352).

Greenhouse gases have had a positive radiative forcing on the climate system by decreasing outgoing longwave radiation at the top of the atmosphere by an amount on the order of 2.5 Wm^{-2} for the period from pre-industrial (1750) to present (2000).

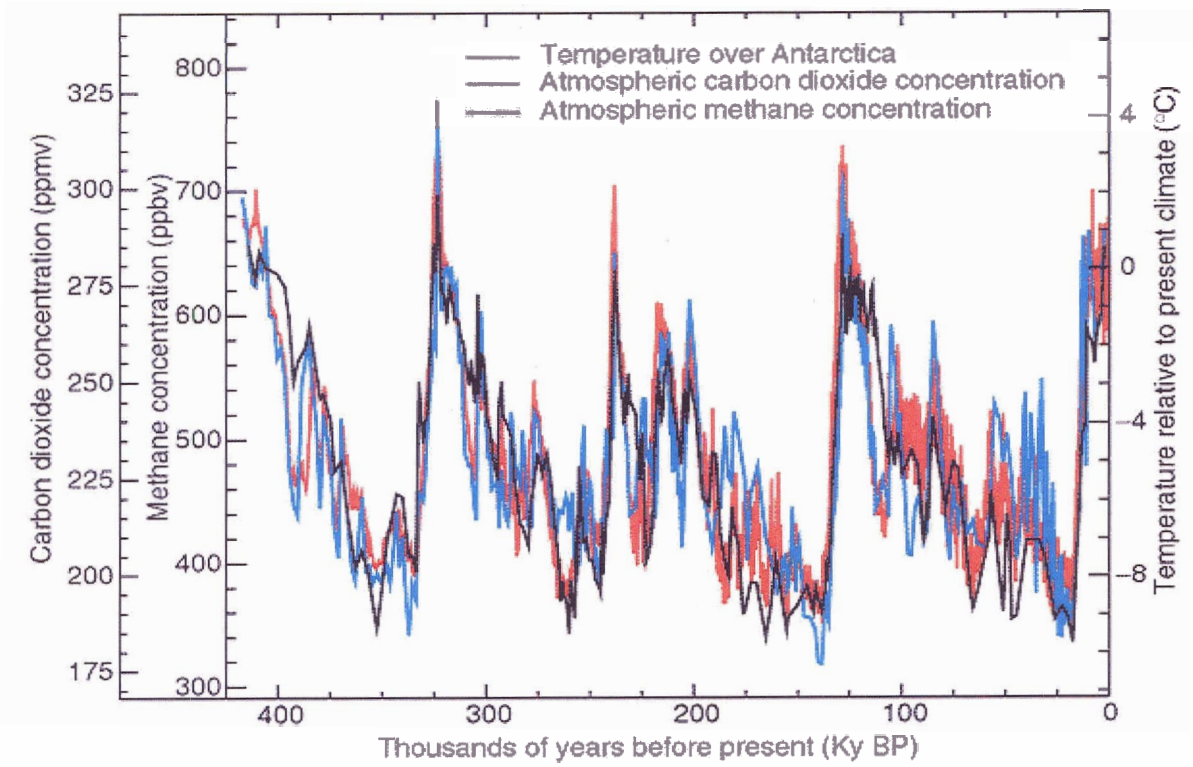

Figure 1.3: Temperature, carbon dioxide and methane reconstructions from Antarctic ice-core records of the past 400,000 years (Petit et al. 1999). Reprinted from Houghton et al. (2001, Figure 2.22).

Radiative forcings for greenhouse gases and a number of other agents are shown in Figure 1.4. Of the human influences shown here, only the effect of greenhouse gases carries a reasonable level of scientific understanding. The direct effect of sulphate aerosols (emitted from the combustion of fossil fuels along with greenhouse gases) is shown here to have a negative radiative forcing. This effect describes the role of sulphate aerosols in back-scattering incoming solar radiation, and has been shown to partially offset greenhouse-gas induced warming in a number of recent model simulations (see for example Johns et al. 2003). Johns et al. (2003) also incorporated the first indirect effect of sulphate aerosols, whereby the presence of anthropogenic sulphate aerosols increases cloud formation by providing additional cloud condensation nuclei. This study gave some support to the (very uncertain) negative radiative forcing estimate shown here, that is thought to result from increased cloud cover, and an associated decrease in net radiation at the surface.

Also shown in Figure 1.4 is an estimate of the small negative radiative forcing that has resulted from historical land-use and land cover change. Shown here is the effect of increases in surface albedo that have resulted from large-scale conversion of natural vegetation (forest) cover to agricultural areas or pasture. Changes in solar irradiance over the past 250 years are thought to have generated a small positive radiative forcing, as shown at the far right of Figure 1.4. Large volcanic eruptions are known to have strong periodic effects on climate through large-scale emissions of sulphate aerosols into the stratosphere. This results in a short term cooling (on the order of a few years) as a result of back-scattered incoming solar radiation (Robock 2000). The net long-term radiative forcing is small, however, and is not included in Figure 1.4.

These natural and anthropogenic climate forcings impose an external perturbation on the global climate system. The response of the climate system to these forcings is highly dependent on internal climate processes and feedbacks. Climate

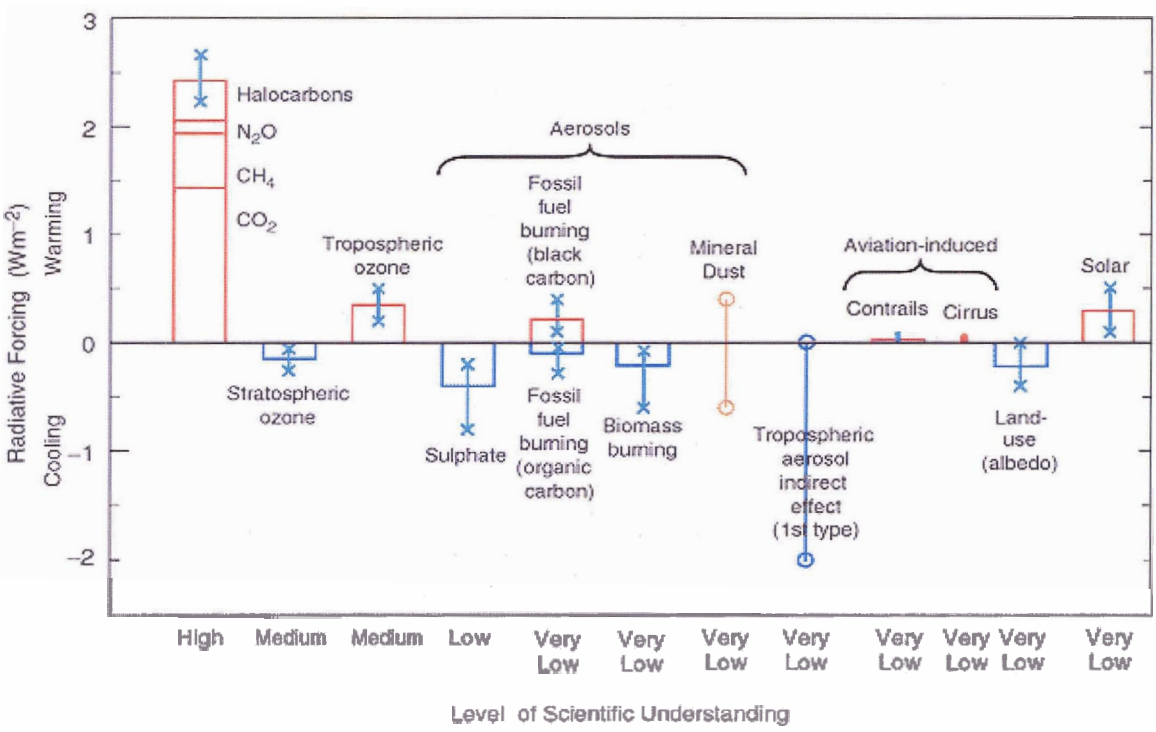

Figure 1.4: Global, annual mean radiative forcings (Wm^{-2}) for the period from pre-industrial (1750) to present (2000), along with their respective levels of scientific understanding. Reprinted from Houghton et al. (2001, Summary for Policymakers, Figure 9).

feedbacks have the potential to either amplify (positive feedback) or reduce (negative feedback) the effect of an external forcing leading to either an increased or lessened temperature response. Important internal climate feedbacks include the effects of changes in atmospheric water vapour (positive), changes in outgoing longwave radiation (negative), changes in ocean circulation and heat transport (positive or negative), changes in sea-ice and snow distributions (positive), dynamic vegetation distribution changes (usually positive), changes in plant photosynthesis under increased atmospheric CO_2 (negative) and the response of the terrestrial carbon cycle to climate warming (positive). The response of cloud abundances and distributions to climate change also constitutes a potentially important feedback to climate, though the sign of this feedback is as yet uncertain on account of the difficulty in parameterizing clouds in general circulation climate models and the highly varied responses that result from climate forcing in different models (Stocker et al. 2001). By necessity, the net effect of all feedbacks in the climate system is negative, resulting in an overall stabilizing response to external perturbations.

One of the first comprehensive simulations of the climate response to natural and anthropogenic forcings was carried out by Stott et al. (2000) using the HadCM3 dynamical climate model. Their study presented simulations of the climate response to natural forcings alone (volcanoes and solar variability), anthropogenic forcings alone (greenhouse gases, tropospheric and stratospheric ozone and sulphate aerosols) and all model forcings combined. The results of this simulation (shown in Figure 1.5) suggested a number of important conclusions. First, natural forcings alone can account for much of the climate warming that was observed in the early part of the 20^{th} century, as well as some of the cooling in mid-century. Second, natural forcings alone did not reproduce late 20^{th} century warming, whereas this trend was well captured by the simulation forced by anthropogenic processes. Third, the best fit to observed temperature trends was seen clearly in the model run that included

both natural and anthropogenic climate forcings.

Simulations such as these have also been used to statistically link observed temperature trends to specific causes, a process referred to as *detection and attribution.* First, model simulations are compared to observations to show that simulated temperature responses are statistically consistent with observations (the simulated trend is *detectable* in the observed trend). If a temperature signal is detected, the cause of the simulated trend (e.g. forcing by greenhouse gases) can be shown to be responsible for trends seen in observations (observed trends are *attributed* to a specific cause). Using simulations from the HadCM2 model, Tett et al. (1999) successfully attributed climate warming in the second half of the 20^{th} century to a combination of greenhouse gas and sulphate aerosol forcings. Warming in the early part of the century was also shown to result from a combination of anthropogenic and solar forcings. Stott et al. (2001) and Jones et al. (2003) extended this research and also showed that volcanic forcing could be detected in 20^{th} century temperature trends. Their research has played an important role in establishing scientific confidence that anthropogenic activities are having a measurable effect on the climate system.

Several reduced complexity climate models (suitable for longer simulations and sensitivity studies) have also been used to simulate the climate response to external forcings over the past 1000 years. Crowley (2000) incorporated solar irradiance and volcanism as well as anthropogenic changes in greenhouse gases and sulphate aerosols into simulations using an energy balance climate model. Crowley's (2000) results indicated that a large portion of pre-anthropogenic climate variability was a result of solar and volcanic forcing; Crowley (2000) was also able to reproduce much of the 20^{th} century warming from greenhouse gas forcing alone. Bauer et al. (2003) performed similar simulations using a climate model of intermediate complexity (CLIMBER-2), and extended Crowley's (2000) study by including the effects of historical land cover change. Bauer et al. (2003) reported a cooling associated with land cover change; this cool-

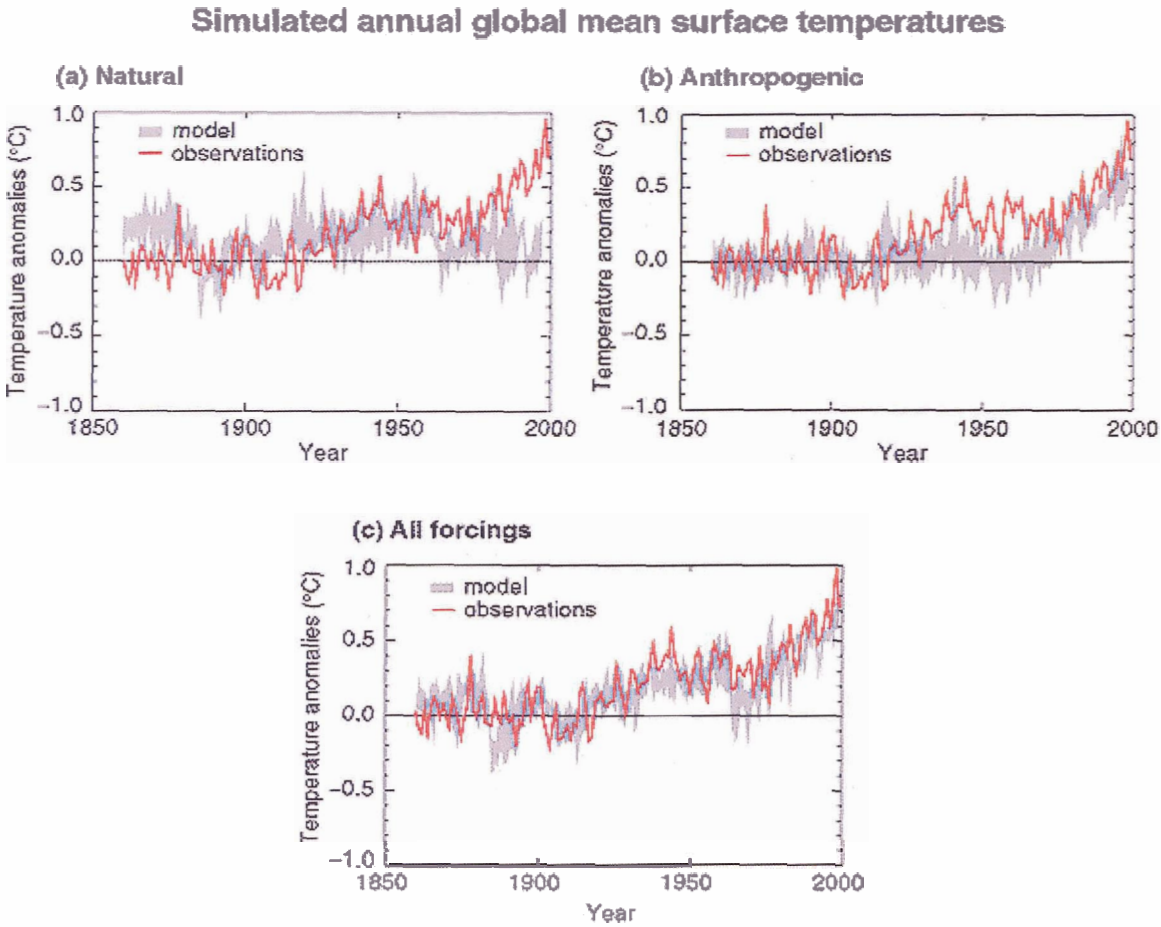

Figure 1.5: Climate response to (a) natural forcings (volcanoes and solar variability), (b) anthropogenic forcings (greenhouse gases, tropospheric and stratospheric ozone and sulphate aerosols) and (c) all model forcings, compared to observed temperature changes (Stott et al. 2000). Reprinted from Houghton et al. (2001, Summary for Policymakers, Figure 4).

ing resulted in more overall simulated cooling in the all-forcings model run than was reported by Crowley (2000), and brought the simulation into somewhat better agreement with historical temperature reconstructions. Bertrand et al. (2002) reported on a detailed sensitivity study using a two-dimensional sector-averaged climate model which was forced over the past millennium by solar changes, volcanism, deforestation, greenhouse gases and tropospheric sulphate aerosols. This study showed that, despite the uncertainties associated with reconstructions of natural climate forcings, natural influences were unable to generate a climate response of comparable magnitude to that observed in the late 20^{th} century. Bertrand et al. (2002) also argued that land cover changes and sulphate aerosols were both necessary to best match the simulation results with recently observed temperature trends.

Global climate models have also been used extensively to assess the likelihood and magnitude of continued climate warming in response to future emissions of anthropogenic greenhouse gases. The IPCC Third Assessment Report projected global temperature increases over the 21^{st} century to be in the range of 1.4 to 5.8 °C (Houghton et al. 2001). This projection (illustrated in Figure 1.6) was generated by averaging the results simulated by a number of climate models around the world, as well as by incorporating results from a simple climate model tuned to the climate sensitivities (the temperature response to a doubling of atmospheric CO_2) of a number of more complex models. All simulations presented in this figure make use of a range of emissions scenarios (provided by the IPCC Special Report on Emissions Scenarios (SRES) (Nakićenović et al. 2000)) that have been run through simple carbon cycle and atmospheric chemistry models to generate projected atmospheric greenhouse gas concentrations that can be used to force more sophisticated global climate models.

Recently, global climate models have been developed to include interactive global carbon cycles, and are now able to calculate atmospheric CO_2 prognostically as a function of anthropogenic emissions and fluxes of carbon between the atmosphere,

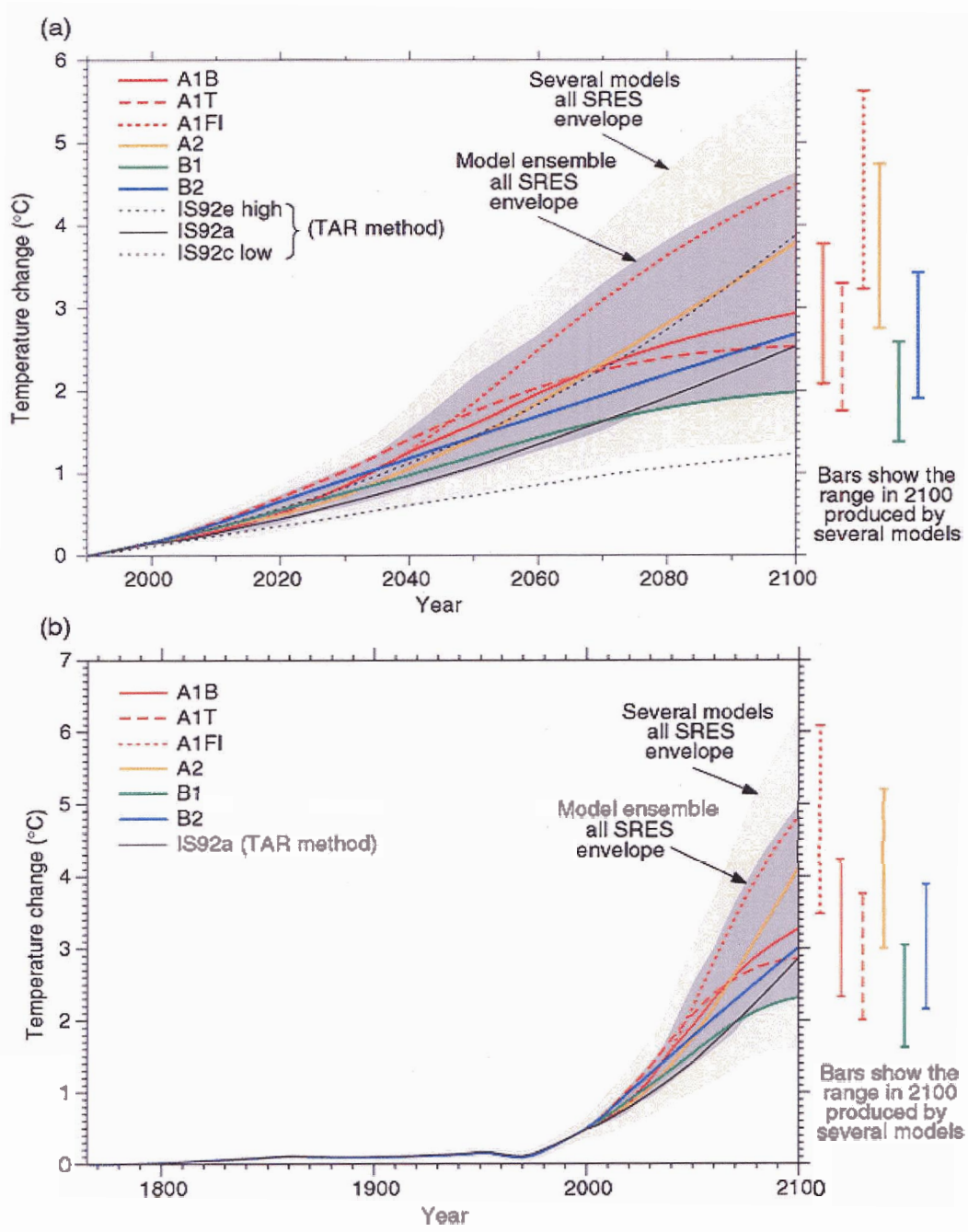

Figure 1.6: Projected 21st century temperature increases from the IPCC Third Assessment Report for a number of future emissions scenarios. Results are from simulations by a simple model tuned to the climate sensitivity of several more complex climate models ("Several models all SRES envelope") and by the average from these more complex models for the range of scenarios simulated ("Model ensemble all SRES envelope"). Results are shown for the 21st century alone (a), and also in relation to simulations of historical temperature changes (b). Reprinted from Houghton et al. (2001, Technical Summary, Figure 22).

ocean and terrestrial biosphere. These coupled climate carbon cycle models are now being used to explore potentially large positive feedbacks between the carbon cycle and climate that are not captured when simulations are forced by specified greenhouse gas levels (Cox et al. 2000, Dufresne et al. 2002). The two such models that have so far been developed have introduced a new layer of uncertainty into future projections of climate warming. In particular, the response of the terrestrial carbon cycle to anthropogenic climate change is currently a subject of much research and debate (see for example Friedlingstein et al. 2003).

1.2 Outline of Dissertation Research

In this dissertation, I focus on the role of terrestrial vegetation in the climate system, considering both the climate forcing that has resulted from human modification of global vegetation cover, and the mechanisms by which vegetation acts as an internal feedback to climate. I carried out climate simulations using the University of Victoria Earth System Climate Model (UVic ESCM), an intermediate complexity climate model that is particularly well situated to explore the role of external climate influences and internal climate feedbacks that operate over time scales of decades to centuries.

I begin in Chapter 2 by describing the UVic ESCM, along with details of the modifications and improvements that have been incorporated into the model for the purpose of the experiments presented in this dissertation. Chapter 3 is devoted to the climate effects of the historical land cover changes that have resulted from human conversion of natural vegetation types to areas of agriculture, pasture and other human land-use activities. I first investigate the climate forcing that results from physical changes to the land surface (such as increased albedo) by using a number of equilibrium and transient climate simulations under a variety of model configurations. I

also present simulations using a coupled climate carbon cycle model to assess the contribution of CO_2 emissions from historical land cover change to observed greenhouse warming.

In Chapter 4, I present transient simulations forced by historical land cover change in the context of other anthropogenic (greenhouse gases and sulphate aerosols) and natural (volcanic aerosols, solar insolation and orbital variability) climate forcings. I analyze simulations forced by each of these climate influences individually, as well as by combinations of forcings, both to assess the ability of the UVic ESCM to reproduce the historical temperature record, and investigate the contribution of individual and combined forcings to the simulated temperature trends. As part of this exploration, an attempt is made to detect the response of the climate model to historical land cover change in historical temperature observations. In this chapter, I also introduce transient simulations using a dynamic terrestrial vegetation model; these simulations highlight the role of vegetation dynamics as a positive feedback to climate under anthropogenic climate change.

Chapter 5 is dedicated to an investigation of the role of the terrestrial biosphere in the global carbon cycle under recent and future climate change. Experiments presented in this chapter use the coupled carbon cycle climate model introduced at the end of Chapter 3. Simulations of the 20^{th} century are presented and compared to available observations of atmospheric CO_2 increase and anthropogenic carbon uptake by land and ocean carbon sinks. These simulations are then extended into the future, forcing the model by six SRES scenarios of future CO_2 emissions. I compare the results of these experiments to other published simulations, focusing on the role of carbon cycle feedbacks to climate.

The results presented in this dissertation represent the work contained in three papers that have been submitted to or published in refereed journals. Matthews et al. (2003) covers the material presented in Chapter 3, Section 3.2.1, which has been

published in *Geophysical Research Letters*. Matthews et al. (2004b) (published in *Climate Dynamics*) covers the remainder of Chapter 3 and all of Chapter 4. Chapter 5 has been written for publication as Matthews et al. (2004a) and submitted to *Journal of Climate*. Chapter 2 contains the model descriptions that are included in all three papers. Chapter 6 summarizes the conclusions presented in this dissertation.

Chapter 2

Model Descriptions

This chapter describes several versions of the UVic Earth System Climate Model (ESCM). The standard version of the coupled climate model, consisting of atmosphere, ocean and sea-ice components, as well as radiative transfer and land surface model additions is described in Section 2.1. This version of the model is the basis for the experiments presented in Chapters 3 and 4 (Sections 3.2 and 4.2). Parameterizations for the inclusion of natural and anthropogenic climate forcings are described in Section 2.1.5 and applied to experiments presented in Chapter 4. The dynamic vegetation model used in Chapter 3 (Section 3.3), Chapter 4 (Section 4.3) and Chapter 5 is described in Section 2.2, along with a more sophisticated land surface model. Finally, the global carbon cycle model used in Chapters 3 (Section 3.3) and 5 is described in Section 2.3.

2.1 Coupled Climate Model

2.1.1 Ocean, Atmosphere and Sea-Ice Models

The UVic Earth System Climate Model (ESCM) is an intermediate complexity coupled atmosphere/ocean/sea-ice climate model. The core of the model is described in detail in Weaver et al. (2001). The ocean component of the model is version 2.2 of the GFDL Modular Ocean Model (Pacanowski 1995), a general circulation ocean model with 19 vertical levels. Sea-ice is represented by a dynamic/thermodynamic model, as described in Bitz et al. (2001). The atmosphere is a vertically integrated

energy/moisture balance model comprised of a single atmospheric layer that captures the climatic mean state in the absence of atmospheric variability. Surface wind stress as well as vertically-integrated atmospheric winds used for advection of moisture are specified from NCEP reanalysis data (Kalnay et al. 1996). A dynamic wind feedback parameterisation allows for wind perturbations to be applied when simulating past climates. CO_2 forcing is applied in the model through a decrease in outgoing longwave radiation, parameterised as:

$$F = F_0 ln \frac{C_{(t)}}{350} \tag{2.1}$$

where $C_{(t)}$ is the atmospheric CO_2 concentration at time t and F_0 is a constant that determines the strength of CO_2 forcing in the model. The coupled model has a resolution of 3.6° in longitude and 1.8° in latitude, and conserves both energy and water to machine precision without the use of flux adjustments (Weaver et al. 2001).

The version of the UVic ESCM used in this dissertation carries a number of differences from that described in Weaver et al. (2001). First, atmospheric moisture transport by diffusion and advection was adjusted to improve the simulation of precipitation over land. Second, an enhanced radiative transfer model allows for the separation of the planetary albedo used in previous versions of the model into surface and atmospheric components. Third, two independent land surface models are included: the first modelled after the bucket model of Manabe (1969), and the second a modified version of the MOSES (Met Office Surface Exchange Scheme) model (Cox et al. 1999). Fourth, modifications were made to allow for the inclusion of volcanic and sulphate aerosols. Fifth, the dynamic vegetation model TRIFFID (Top-down Representation of Interactive Foliage and Flora Including Dynamics) (Cox 2001) was coupled to the UVic ESCM. Last, the terrestrial carbon cycle component of TRIFFID and the inorganic ocean carbon cycle described in Weaver et al. (2001) were coupled.

These model improvements are described in the following sections. Sections 2.1.2 through 2.1.5 describe modifications to the standard version of the coupled model described in Weaver et al. (2001). These modifications represent the majority of the model development work that I carried out for the purposes of this research. Section 2.2 provides a brief description the dynamic vegetation model TRIFFID and associated land surface model MOSES. These were coupled to the UVic ESCM by K. Meissner, and are described fully in Meissner et al. (2003). My involvement in the early stages of this process was peripheral, though I did assist with the model tuning necessary to prepare the model for the simulations that I performed as part of this research project. Section 2.3 describes the process by which I coupled the carbon fluxes calculated within MOSES/TRIFFID and the inorganic ocean carbon cycle model described in Weaver et al. (2001), with the atmosphere. This work resulted in an operational global carbon cycle model coupled to the UVic ESCM.

2.1.2 Precipitation and Atmospheric Moisture Transport

The inclusion of a land-surface model in the UVic ESCM (as described below in Section 2.1.4), led to substantial improvements to the simulated precipitation over land, by allowing for moisture storage in the soil and subsequent recycling of moisture over continents through evaporation. However, in the original model version, surface winds from NCEP were specified and used for advection of moisture in the atmosphere. While this led to a very good simulation of precipitation over the oceans (see Weaver et al. (2001) for a comparison of modelled precipitation to NCEP precipitation), surface winds did not provide sufficient moisture transport over land. This situation was addressed by replacing the specified surface winds with a weighted integral of all available NCEP winds from the surface to the top of the troposphere. Winds were weighted with a negative exponential function to be consistent with the exponential decrease of moisture with height in the atmosphere. In addition, in the standard

version of the UVic ESCM, a prescribed lapse rate is used over topography on land to determine the atmospheric temperature at which precipitation occurs (Weaver et al. 2001). In a single-layer atmosphere however, this biases the model toward very high precipitation over mountains: colder temperatures lead to high precipitation rates, which create large horizontal moisture gradients and lead to unphysically high moisture diffusion from adjacent lower elevation gridcells. In an attempt to correct this situation, the lapse rate used to generate precipitation in the model was reduced by an amount that was varied according to the elevation at each gridcell. This serves to de-emphasize the role of mountains in the generation of precipitation in the model and improves the model's simulated hydrological cycle.

The simulated precipitation fields with and without the above modifications are shown in Figure 2.1. While there are small changes evident over the oceans, the most dramatic changes occur on land, particularly in the tropics. As can be seen in Figure 2.2, this new precipitation field still differs from NCEP precipitation in several important ways. Over the oceans, precipitation is too low along the inter-tropical convergence zone, and too high in eastern subtropical latitudes. These differences result in part from the use of vertically integrated rather than surface winds for the advection of moisture as described above. In addition, it is possible that the diffusion of atmospheric moisture is too high in tropical latitudes. Over land, notable discrepancies remain over mountains and in the interior of continents. Precipitation over mountains results primarily from the decrease in temperature associated with the specified lapse rate; reducing the lapse rate over mountains does decrease this effect, but this remains an outstanding problem in the simulation of precipitation in this model.

Due to the use of advection by mean winds and diffusion to supply moisture to the interior of continents (the UVic model does not simulate transient eddies in the atmosphere), precipitation over central Asia and North America is too low. This

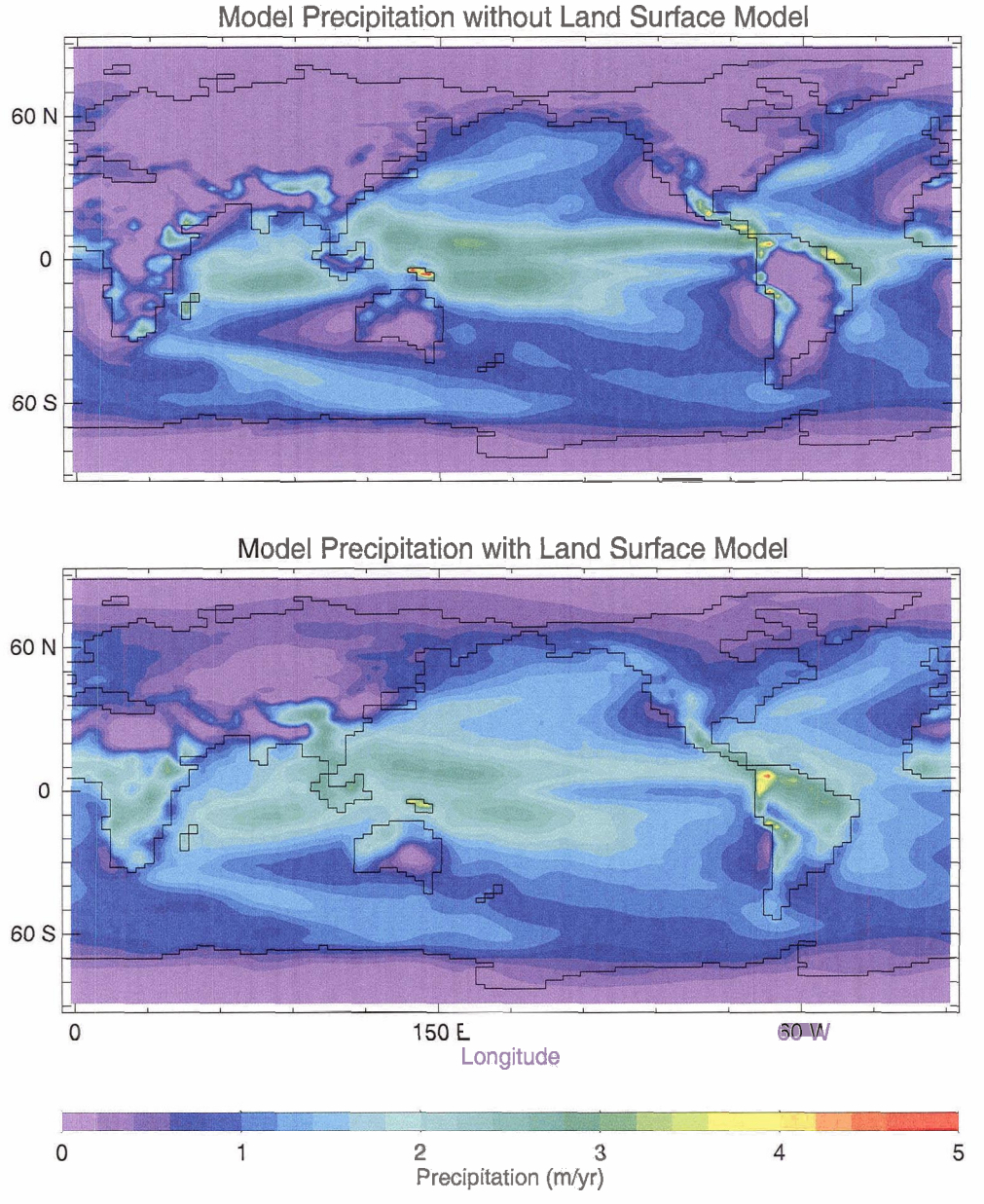

Figure 2.1: **Modelled annual mean precipitation from Weaver et al. (2001) without a land-surface model (top) compared to modelled annual mean precipitation after inclusion of the bucket land surface model (bottom).**

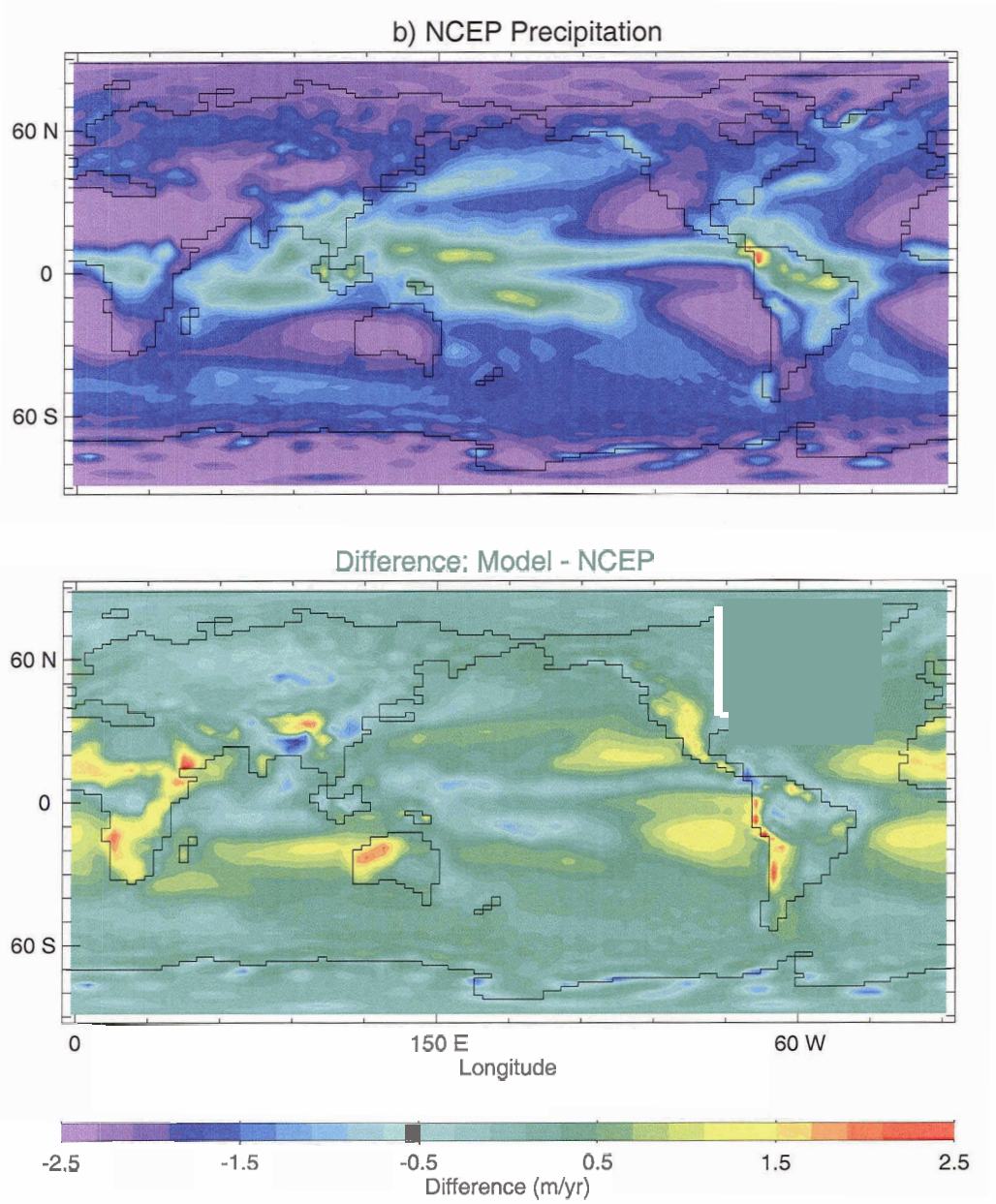

Figure 2.2: **NCEP annual mean precipitation (top); Difference between modelled annual mean precipation (Figure 2.1 (bottom)) and NCEP precipitation.**

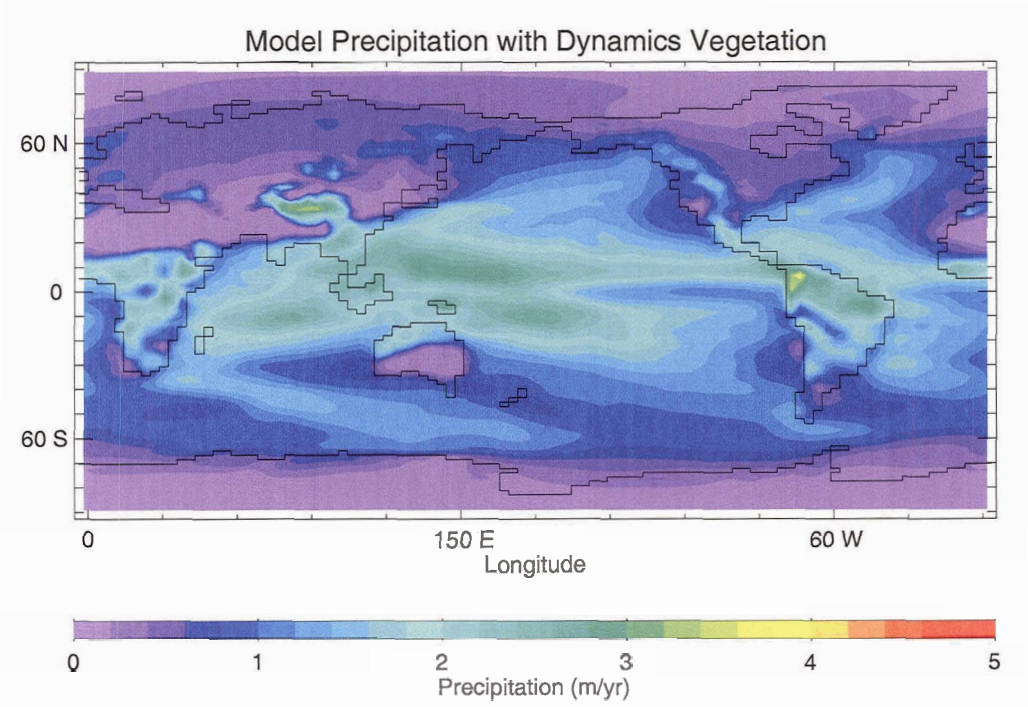

Figure 2.3: **Modelled annual mean precipiation for the model version including dynamic vegetation.**

becomes a problem when vegetation is simulated dynamically in the climate model, as is the case with the use of TRIFFID. To enable a realistic simulation of boreal forest in the climate model, it was necessary to increase zonal diffusion of moisture, particularly over Asia and North America. At the same time, meridional diffusion was decreased in the tropics, and this resulted in an improved simulation of precipitation in Northern Africa. The precipitation field that resulted from these changes (used only for simulations with the dynamic vegetation model described in Section 2.2) is shown in Figure 2.3.

2.1.3 Radiative Transfer Model

In previous versions of the UVic ESCM, a zonally averaged planetary albedo, $\alpha_{p(z)}$, was specified according to the parameters given in Graves et al. (1993). The net

shortwave radiation at the surface was calculated as:

$$\downarrow SW = (1.0 - \alpha_{p(z)}) \cdot I_s \tag{2.2}$$

where I_s is the incident shortwave radiation at the top of the atmosphere. For the current study, it was necessary to incorporate a more detailed radiative transfer model that would include an explicit representation of surface albedo and a subsequent calculation of a two-dimensional planetary albedo field.

The approach chosen was based on the theory outlined in Haney (1971) and illustrated in Gill (1982, p.10), where planetary albedo (α_p) is calculated as a function of surface albedo (α_s), atmospheric albedo (α_a) and atmospheric absorption (A_a):

$$\alpha_p = (1 - \alpha_a)(1 - A_a)\alpha_s + \alpha_a \tag{2.3}$$

In this radiative transfer model (shown in Figure 2.4), atmospheric albedo is made up of a clear sky albedo (set to 0.08) and a cloud albedo, which makes up the majority of the total albedo of the atmosphere.

As the UVic ESCM does not model clouds explicitly, a cloud albedo must be diagnosed rather than calculated dynamically by the model. In order to accomplish this, equation 2.3 is first rearranged to solve for atmospheric albedo as:

$$\alpha_a = \frac{\alpha_p - \alpha_s(1 - A_a)}{1 - \alpha_s(1 - A_a)} \tag{2.4}$$

In order to calculate atmospheric albedo at any specific point, this formula requires a known planetary albedo, surface albedo and atmospheric absorption. To maintain consistency with the previous version of the UVic ESCM, zonally averaged planetary albedo $\alpha_{p(z)}$ is specified from Graves et al. (1993). As this representation of planetary albedo does not include the albedo effect of snow at the surface, snow-free surface

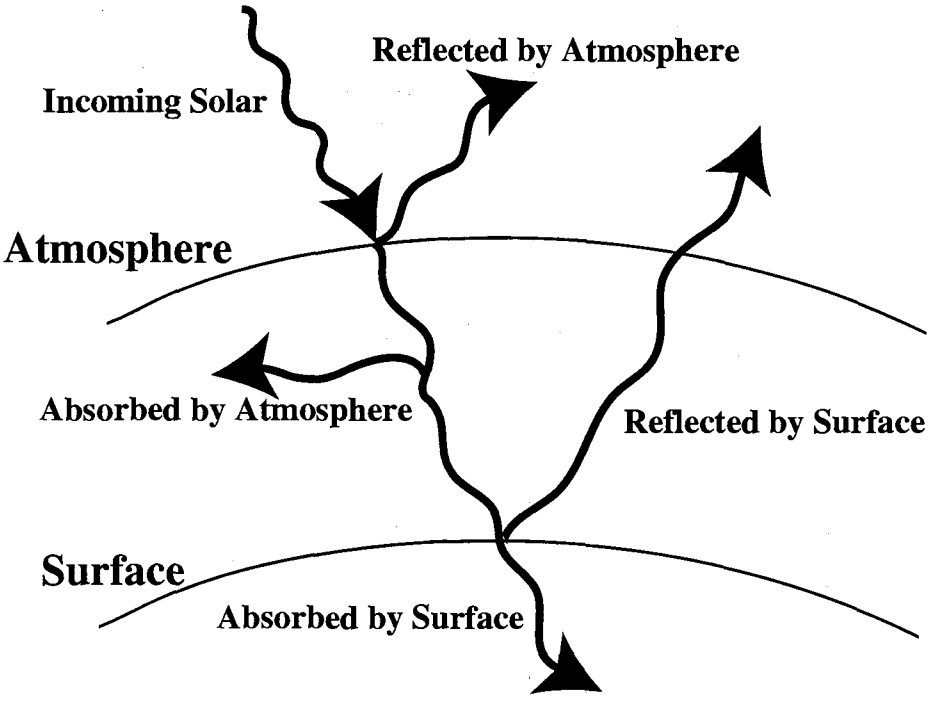

Figure 2.4: **Updated radiative transfer model used in the UVic ESCM**

albedo is then specified from ISLSCP data (Sellers et al. 1996). Ocean albedo is set to 0.06 equatorward of 30°, and increases sinusoidally to 0.17 poleward of 70°. Atmospheric absorption is set to a constant value of 0.3.

Given a surface albedo value at some gridcell, equation 2.4 can be used to calculate the atmospheric albedo necessary to reproduce the correct planetary albedo. However, in order that zonal variation in surface albedo are reflected in the planetary albedo field, equation 2.4 was averaged at each latitude to solve for a zonally averaged atmospheric albedo:

$$\alpha_{a(z)} = \frac{\alpha_{p(z)} - \alpha_{sf(z)}(1 - A_a)}{1 - \alpha_{sf(z)}(1 - A_a)} \tag{2.5}$$

where $\alpha_{sf(z)}$ is now the zonally averaged snow-free surface albedo. In this procedure, products of deviations from the zonal means can be removed from the equation, as α_p and A_a do not vary zonally.

Once a zonally averaged atmospheric albedo is obtained, it is inserted into equa-

tion 2.3 which becomes:

$$\alpha_p = (1 - \alpha_{a(z)})(1 - A_a)\alpha_s + \alpha_{a(z)} \tag{2.6}$$

Surface albedo is now generated by the land surface model and is allowed to change as a function of snow, ice or changing vegetation distributions. With atmospheric albedo held zonally constant, a new planetary albedo field can be calculated. The net shortwave radiation at the surface becomes:

$$\downarrow SW = (1.0 - \alpha_p) \cdot I_s \tag{2.7}$$

where α_p is now a two-dimensional field which reflects the underlying spatial variation in surface albedo. An example of the planetary albedo field generated by this procedure is shown in Figure 2.5. As a final note, a zonally constant atmospheric albedo implies that clouds are not represented dynamically in the model. As such, feedbacks between changing climate and clouds are not included.

2.1.4 Land Surface Model

The model described here is a version of the simple bucket model, first developed for use in a general circulation climate model by Manabe (1969). This model calculates soil moisture (W) using a bucket approach:

$$\frac{\delta W}{\delta t} = P_R + S_M - E - R \tag{2.8}$$

Inputs to the soil moisture bucket come in the form of precipitation (P_R) and snowmelt (S_M); outputs take the form of evapotranspiration (E) and runoff (R). The model uses a spatially uniform 15 cm bucket on land as a representation of the moisture holding capacity of the soil. Runoff occurs only when the bucket is full and the

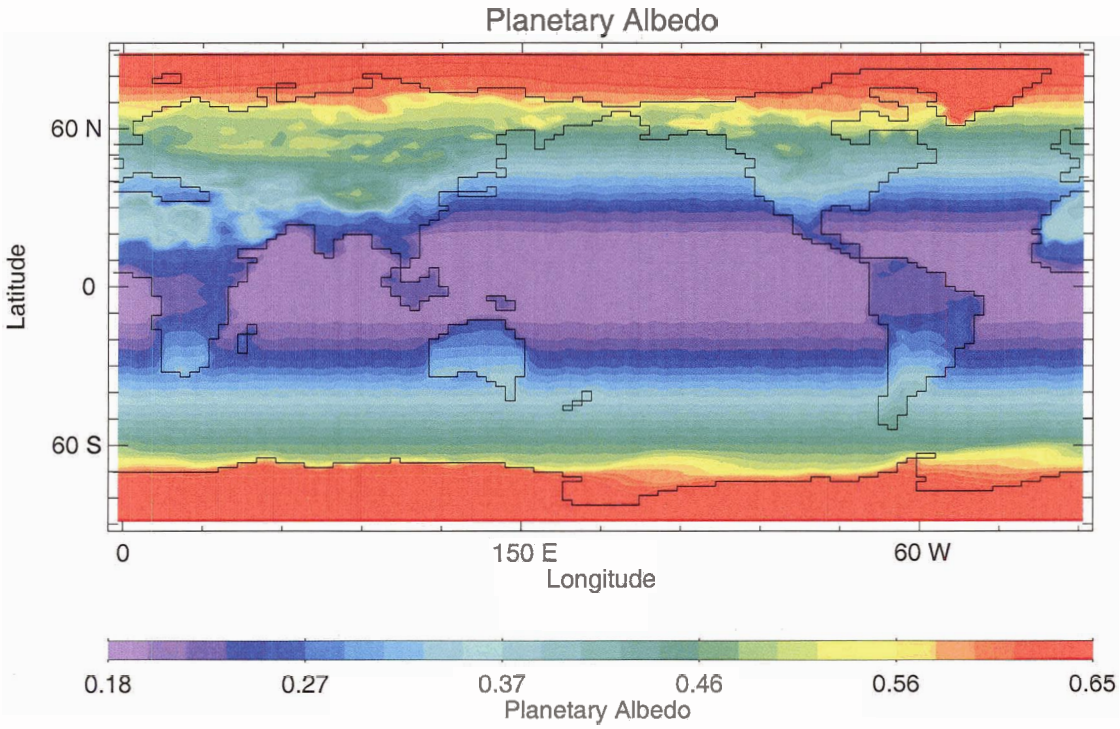

Figure 2.5: **Planetary albedo field generated by the updated radiative transfer model for a transient run at the year 2000, with cropland distributions specified at the surface (see Chapter 3).**

moisture holding capacity of the soil has been exceeded.

The simplest parameterisation of evaporation is that used in the original version of the bucket model and is based on a bulk formulation of potential evaporation. This formulation involves the specification of a surface resistance that reduces evaporation from its potential rate in cases where soil moisture is limiting. Following the methodology of a number of other land-surface models (see for example Dickinson 2001, Zeng et al. 2000, Cox et al. 1999), I modified the original bulk formulation of evaporation by parameterizing evapotranspiration as:

$$E_T = \rho_a \frac{\beta}{r_a + r_s}[q_{sat}(T_s) - q_a] \tag{2.9}$$

where ρ_a is the density of air, $q_{sat}(T_s)$ is the saturation specific humidity of air at the surface temperature and q_a is the atmospheric specific humidity. The term β imposes a dampening on evaporation as water availability decreases, and is calculated as $\beta = (W/W_0)^{1/4}$ where W is the soil moisture content and W_0 is the soil water holding capacity or bucket depth (15 cm) (Zeng et al. 2000).

The resistance terms r_a and r_s are the aerodynamic and surface resistances, which impose physical and physiological constraints on evapotranspiration. The first of these (r_a) is a function of the Dalton number for evaporation and the surface wind speed: $r_a = (C_D \cdot U)^{-1}$. The Dalton number is calculated from a specified surface roughness length (z_0) according to the methodology of Brutsaert (1982):

$$C_D = k^2(\ln \frac{z}{z_0})^{-1}(\ln \frac{z}{z_{0q}})^{-1} \tag{2.10}$$

where z is a reference height ($z = 10m$) and k is the von Karman constant ($k = 0.4$). The roughness lengths for moisture (z_{0q}) and heat (z_{0h}) are calculated as $z_{0q} = z_{0h} = e^{-2}z_0$ (Brutsaert 1982).

The inclusion of a specified surface resistance (r_s) allows for an additional surface

resistance that represents the role that vegetation plays in moderating moisture fluxes to the atmosphere. The values of surface resistance chosen for this study follow the relative magnitudes of those given by Dickinson (2001), but have been reduced in absolute magnitude to put them in the range of those given by Cox et al. (1999). As there is substantial discrepancy between these two sources, a compromise was chosen to allow variability between vegetation types, while at the same time producing a climatology for evapotranspiration that is comparable to reanalysis data (Figure 2.6: (a) and (b)). As can be seen in Figure 2.6c, discrepancies between modelled evaporation and NCEP reanalysis data largely reflect the differences in precipitation shown in Figure 2.2b.

Vegetation is specified in the land surface model using the vegetation data set of DeFries and Townsend (1994). Eight vegetation types were chosen to represent the range of vegetation provided in the dataset (shown in Table 2.1), noting that cropland differs from grassland/savanna only in its surface resistance. In the absence of cropland, a single vegetation type was specified at each gridcell, and in addition to surface resistance, the vegetation type determines the roughness length and the surface albedo. The values for these two parameters were determined by spatially and annually averaging roughness length and surface albedo data fields provided by Sellers et al. (1996) according to the specified vegetation types. The surface albedo field generated by this process is shown in Figure 2.7, along with the original Sellers et al. (1996) dataset. Vegetation type-dependent parameter values are shown in Table 2.1, and are consistent with values given in the literature (see for example Wilson and Henderson-Sellers 1985, Cox et al. 1999, Dickinson 2001).

When snow is present in a gridcell, the surface albedo is determined on the basis of the underlying vegetation albedo and a fractional snow cover. Using vegetation-specific snow-masking depths ($S.M.D.$, also shown in Table 2.1), the fractional area

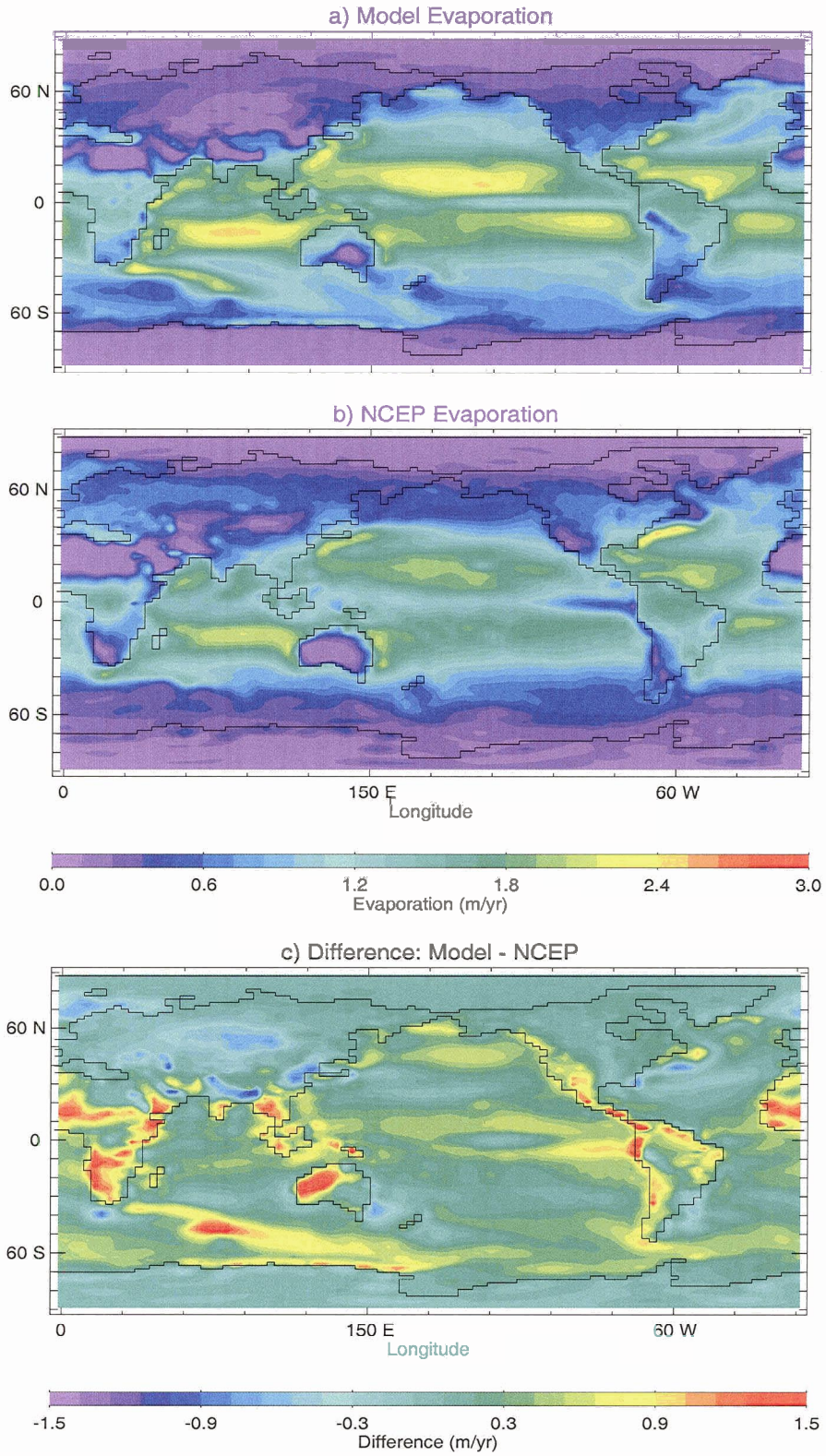

Figure 2.6: a) Modelled annual mean evaporation using the modified bucket land surface model with surface resistance included, b) NCEP annual mean evapitation, and c) Model-NCEP difference.

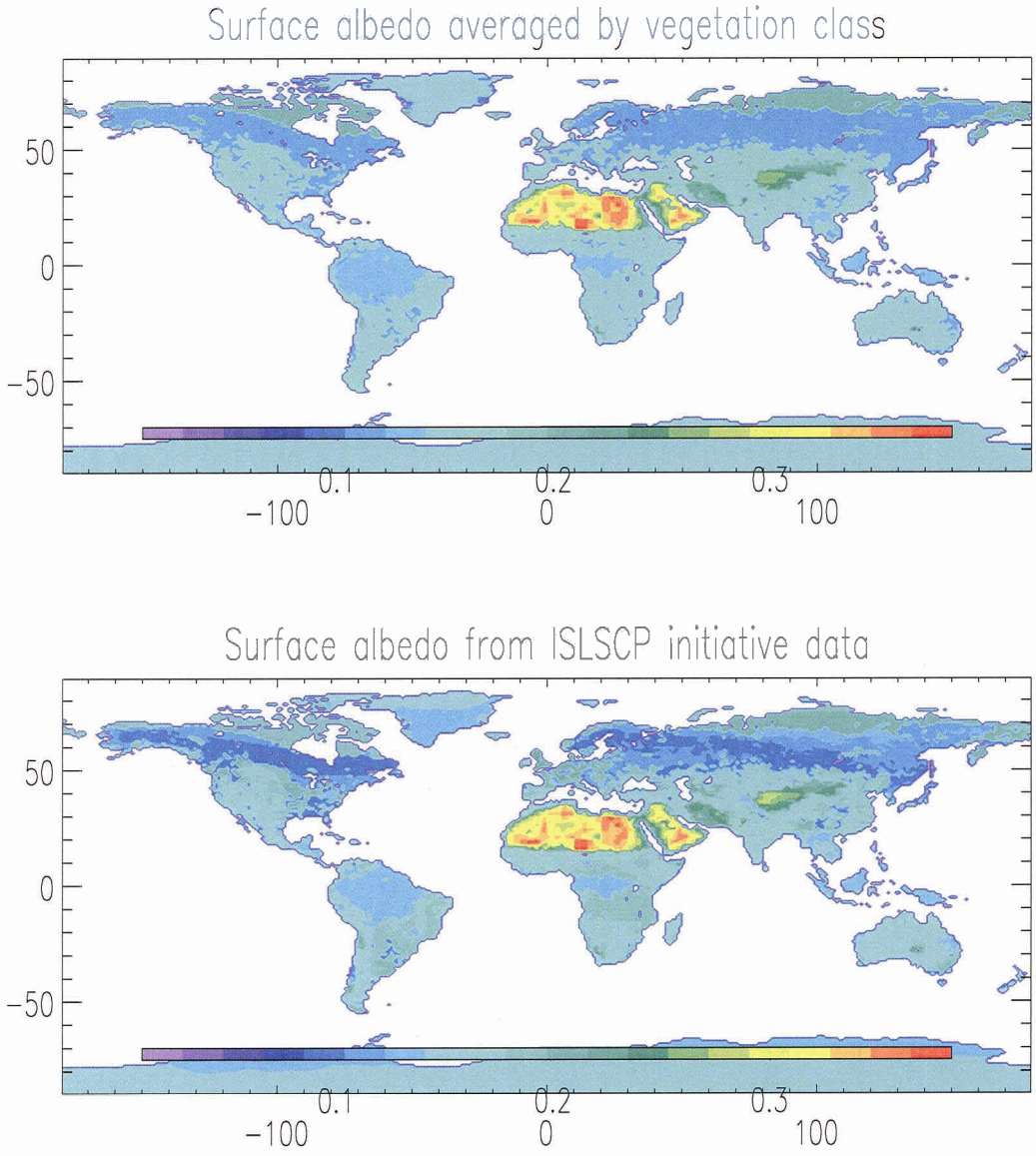

Figure 2.7: **Calculated surface albedo as a function of vegetation type, compared to ISLSCP satellite data (Sellers et al. 1996).**

Table 2.1: **Vegetation Types and specified Surface Albedo (α_s) and Roughness Length (z_0) values as derived from DeFries and Townsend (1994) and Sellers et al. (1996). Surface Resistances (r_s) and Snow-Masking Depths (S.M.D) are taken from Dickinson (2001) and Cox et al. (1999).**

Vegetation Type	α_s	z_0 **(m)**	r_s **(s/m)**	**S.M.D (m)**
Tropical Forest	0.13	2.86	75	10.0
Temperate/Boreal Forest	0.11	0.91	100	10.0
Grassland/Savanna	0.17	0.11	100	0.1
Cropland	0.17	0.11	60	0.1
Shrubland	0.17	0.05	100	1.0
Tundra	0.20	0.04	100	0.1
Desert	0.28*	0.04	100	0.01
Rock/Ice	0.14	0.02	100	0.01

* This is the average of the albedo values for all desert points. Actual values are spatially variable and range from 0.2 to 0.38.

of snow in a gridcell (A_{snow}, constrained between 0.0 and 1.0) is calculated as:

$$A_{snow} = max[H_{snow}, K\frac{T_{air} - T_{start}}{T_{end} - T_{start}}] \cdot \frac{1}{S.M.D} \tag{2.11}$$

where T_{start} and T_{end} are set to –5 °C and –10 °C respectively, T_{air} is the atmospheric temperature, H_{snow} is the snow height in meters (Weaver et al. 2001). K is a constant equal to 1 meter, which assigns units of meters to the expression $(T_{air} - T_{start})/(T_{end} - T_{start})$. The albedo for snow is then applied to this fractional area (A_{snow}), with the underlying snow-free albedo given to the remaining portion of the gridcell. This results in a linear transition from snow-free surface albedo to the albedo for snow or sea-ice that depends on snow depths, temperature and the vegetation snow masking depth. The result of this parameterization is that either snow height or temperature can be used to determine the fractional coverage of snow in a gridcell. This allows for a realistic simulation of snow area (and consequently surface albedo) in areas where the model's hydrological cycle does not simulate enough snowfall, as is common over continents in the Northern hemisphere. It is assumed here that if the air is cold

enough, the snow cover will be sufficient to warrant modifying surface parameters.

It should be noted that in the version of the model described in Weaver et al. (2001), the presence of snow at the surface increased the planetary albedo by a uniform amount of 0.18. In the initial stages of model development, this parameterization was adapted so that the local surface albedo (based on the vegetation type) was increased by 0.18 in the portion of the gridcell occupied by snow. As a result, in the early experiments performed using this model (those described in Section 3.2.1), the snow albedo was not constant, but rather reflected the underlying surface cover. This inconsistency was later corrected by fixing the snow albedo at 0.45 and applying this albedo to the fraction of the gridcell covered by snow. All subsequent experiments using this land surface model (beginning in Section 3.2.2) use this more consistent parametrization of snow albedo.

Surface temperature is calculated from the energy balance equation:

$$R_{NET} = LE + SH \tag{2.12}$$

R_{NET} is the net radiation at the surface (comprising absorbed shortwave and emitted longwave radiation), LE is the latent heat from evaporation and SH is the sensible heat exchange. Latent heat is calculated as $LE = \lambda \cdot E$ where λ is the latent heat of evaporation/sublimation and E is the evaporation as described above. Sensible heat is calculated from a bulk formula based on the temperature difference between the surface (T_s) and the atmosphere (T_a): $SH = \rho\ C_D\ U(T_s - T_a)$ where the Dalton number (C_D) is calculated as for evaporation, using the roughness length for heat (z_{0h}) rather than moisture. Surface temperature is calculated iteratively based on the joint dependence of emitted longwave radiation, latent heat and sensible heat fluxes. There is no heat storage in the land surface.

2.1.5 External Climate Forcings

Chapter 4 incorporates natural and anthropogenic climate forcings into the UVic ESCM. The natural forcings used are solar insolation and orbital variations and volcanic aerosols. Anthropogenic forcings include greenhouse gases and sulphate aerosols, as well as historical land cover change (explored in detail in Chapter 3). Data used to force the model are shown in Figure 2.8 and are discussed in the following sections.

2.1.5.1 Natural Forcings

Solar insolation is specified according to Lean et al. (1995) as a perturbation to the solar constant. Solar orbital variation is calculated using Berger's 1978 method, as described in Weaver et al. (2001). Volcanic aerosols are specified as a globally averaged optical depth from the data of Robock and Free (1995) prior to 1850, and the data of Sato et al. (1993) from 1850 to 1999. These optical depth data are converted to a radiative forcing by the method used in Crowley (2000):

$$F = -k \cdot \tau \tag{2.13}$$

where the volcanic forcing (F) is a function of k (set to –30 W/m^2 per unit optical depth) and optical depth (τ). This forcing is subtracted directly from the downward shortwave radiation incident at the top of the atmosphere.

2.1.5.2 Anthropogenic Forcings

Greenhouse gas forcing is specified using equation 2.1, with greenhouse gas data (both CO_2 and non-CO_2 greenhouse gases as a CO_2 equivalent) taken from Schlesinger and Malyshev (2001) and applied as a perturbation to outgoing longwave radiation. Anthropogenic sulphate aerosol optical depth data are taken from Tegen et al. (2000)

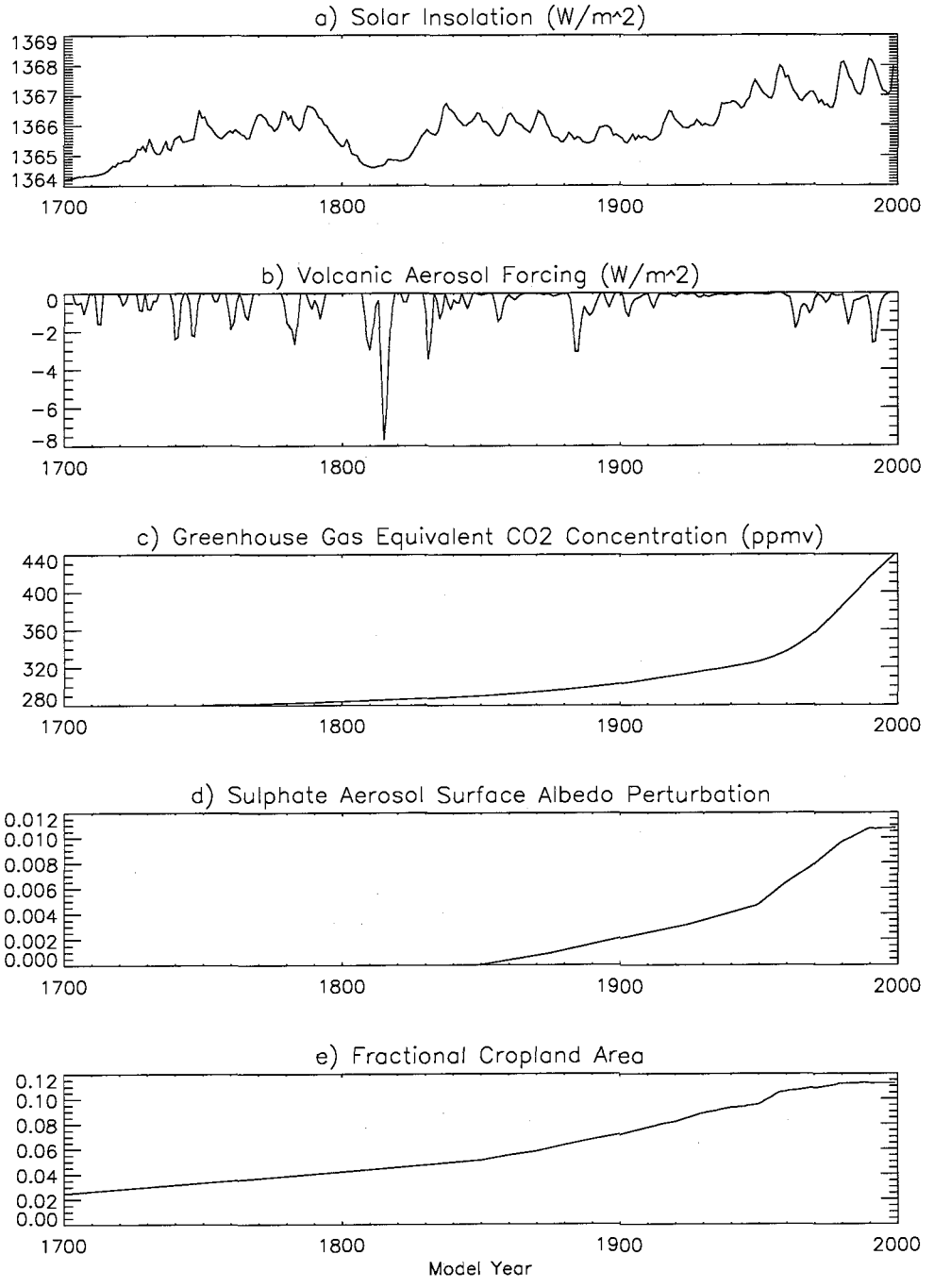

Figure 2.8: **Natural and anthropogenic forcing data: (a) Solar insolation from Lean et al. (1995); (b) Volcanic aerosol forcing from Robock and Free (1995) and Sato et al. (1993); (c) Greenhouse gas equivalent CO_2 concentration from Schlesinger and Malyshev (2001); (d) Sulphate aerosol surface albedo perturbation calculated from the data of Tegen et al. (2000) and Koch (2001); and (e) Global cropland fraction from Ramankutty and Foley (1999).**

and Koch (2001). These data are applied as perturbation to the local surface albedo as:

$$\triangle\alpha_s = \beta\tau(1-\alpha_s)^2 cos(Z_{eff}) \tag{2.14}$$

where β=0.29 is the upward scattering parameter, τ is the specified aerosol optical depth, α_s is the surface albedo and Z_{eff} is an effective solar zenith angle such that $cos(Z_{eff})$ is the diurnally averaged cosine of the zenith angle (Charlson et al. 1991).

Land cover change is represented by a modification of natural vegetation cover, replacing existing forest or grassland vegetation types with cropland or pasture. Two historical land cover datasets are used in Chapter 3. The first is that of Ramankutty and Foley (1999), which consists of fractional cropland areas on a 1° grid for every year from 1700 to 1992, determined based on available historical records and interpolated linearly for intervening years. Accompanying the yearly croplands dataset is a potential or "natural" vegetation field, that forms the backdrop onto which croplands are applied (Ramankutty and Foley 1999). The second dataset used is that of Klein Goldewijk (2001). This dataset includes both historical croplands on a 0.5° grid as well as land used as pasture, and so contains a more complete picture of historical land cover change. Furthermore, the placement of crop and pasture areas is determined from historical population densities, and so provides an independent corollary to Ramankutty and Foley (1999). Data are only provided, however, at 20 to 50 year intervals from 1700 to 1990, and consist of a single vegetation type at each gridcell. In all cases, areas occupied by cropland or pasture are assigned modified surface parameters according to the values given in Table 2.1.

2.2 Dynamic Vegetation Model

2.2.1 TRIFFID Dynamic Vegetation Model

The dynamic terrestrial vegetation model used in Chapters 4 and 5 is the Hadley Centre's TRIFFID (Top-down Representation of Interactive Foliage and Flora Including Dynamics) model (Cox 2001). TRIFFID has been coupled interactively with the UVic ESCM (as described in Meissner et al. (2003)) and explicitly models five plant functional types: broadleaf trees, needleleaf trees, C_3 grasses, C_4 grasses and shrubs. The five vegetation types are represented as a fractional coverage of each gridcell, and compete amongst each other for dominance as a function of the model simulated climate. Simulated vegetation distributions for the five vegetation types are shown in Figure 2.9 for a present-day equilibrium run that excluded croplands (Meissner et al. 2003).

Croplands in TRIFFID can be specified by allocating a portion of gridcells where only grass plant functional types are allowed to grow. This excludes tree plant functional types which would otherwise out-compete grasses given a favourable climate regime. The distribution of C3 and C4 grasses within specified cropland areas is simulated as a function of climatic conditions, as in areas where grasses would grow naturally.

2.2.2 MOSES Land Surface Model

The land surface model used to support the TRIFFID dynamic vegetation model is a single soil-layer version of MOSES (The Met Office Surface Exchange Scheme), based on that described in Cox et al. (1999). The version of MOSES used here calculates soil moisture, soil and surface temperatures and lying snow based on a single soil layer model of uniform 1 meter thickness. The five vegetation types simulated by

TRIFFID are recognized by this model, in addition to bare soil.

As in the simpler land surface model described above, soil moisture is calculated by a budget approach:

$$\frac{\delta W}{\delta t} = P_R + S_M - E - R \tag{2.15}$$

In this model, evapotranspiration (E) is made up of bare soil evaporation, and transpiration calculated for each plant functional type i:

$$E_i = \nu_i \frac{\rho_a}{r_a + r_{s,i}} [q_{sat}(T_{s,i}) - q_a] \tag{2.16}$$

where $r_{s,i}$ is now an interactively calculated canopy resistance term that depends on vegetation type, primary productivity and climatic conditions, or in the case of bare soil evaporation, a soil surface resistance term that depends on available soil moisture. In this formulation, ν_i represents the fractional area of each vegetation type, with total evapotranspiration calculated as: $E = \sum E_i$. Runoff is now based on the "leaky bucket" method of Clapp and Hornberger (1978), and is calculated as:

$$R = K_S \left(\frac{W}{W_{SAT}} \right)^{(2b+3)} \tag{2.17}$$

where K_s (saturated soil hydraulic conductivity), W_{SAT} (soil moisture saturation level) and b (Clapp/Hornberger parameter) are held constant. Simulated soil moisture for this model and for the modified bucket model described in Section 2.1 are shown in Figure 2.10.

Surface albedo is calculated interactively as a function of vegetation distributions, leaf area index, leaf phenology, snow cover and vegetation snow masking depths. The maximum albedo value for a snow-covered gridcell for this model is set to 0.6. The surface energy balance is also calculated for each vegetation type i, and is expanded

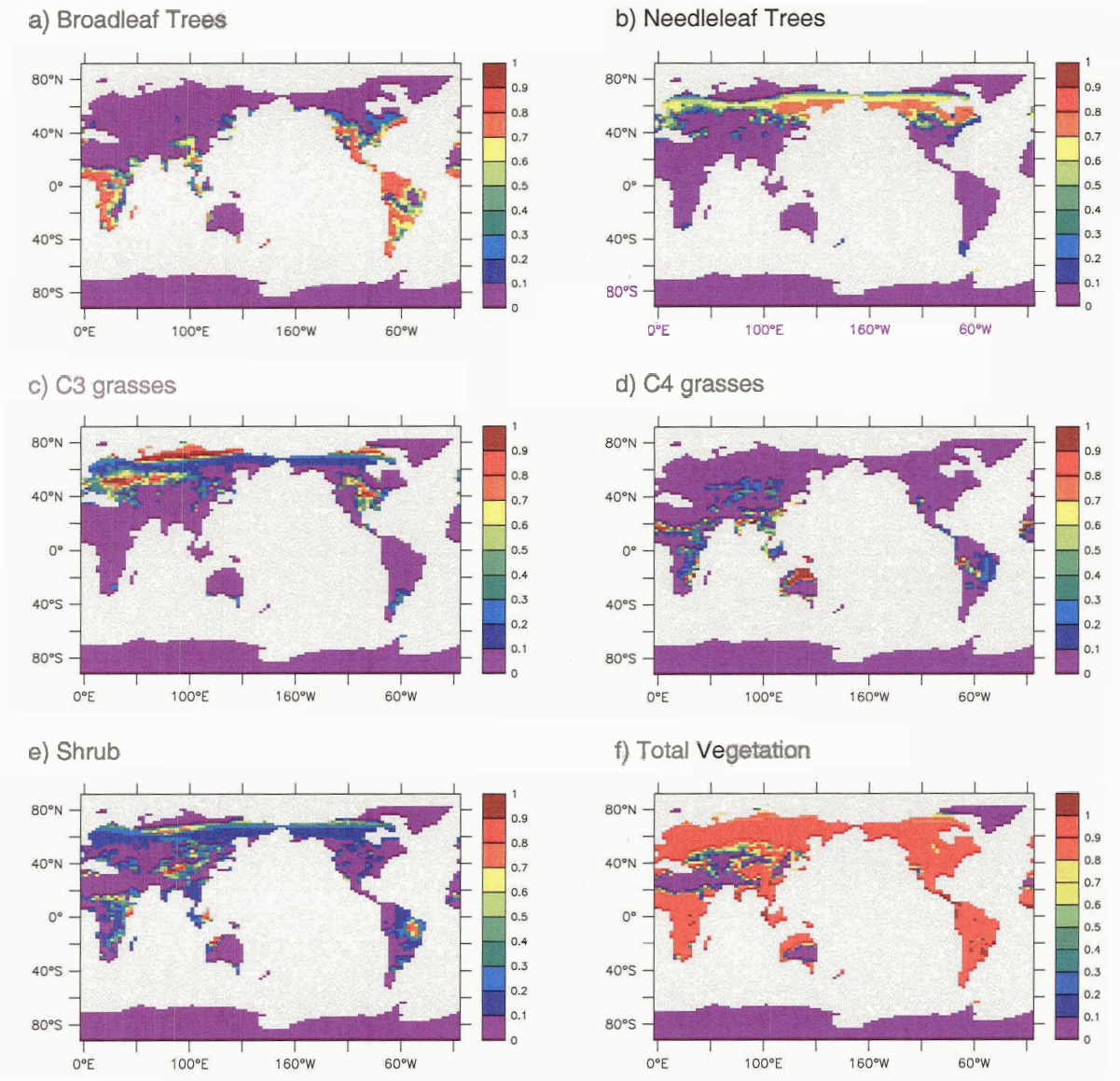

Figure 2.9: **Simulated fractional vegetation coverage for the five TRIFFID vegetation types and the total vegetation cover from a present-day equilibrium, excluding croplands. Reprinted with permission from Meissner et al. (2003).**

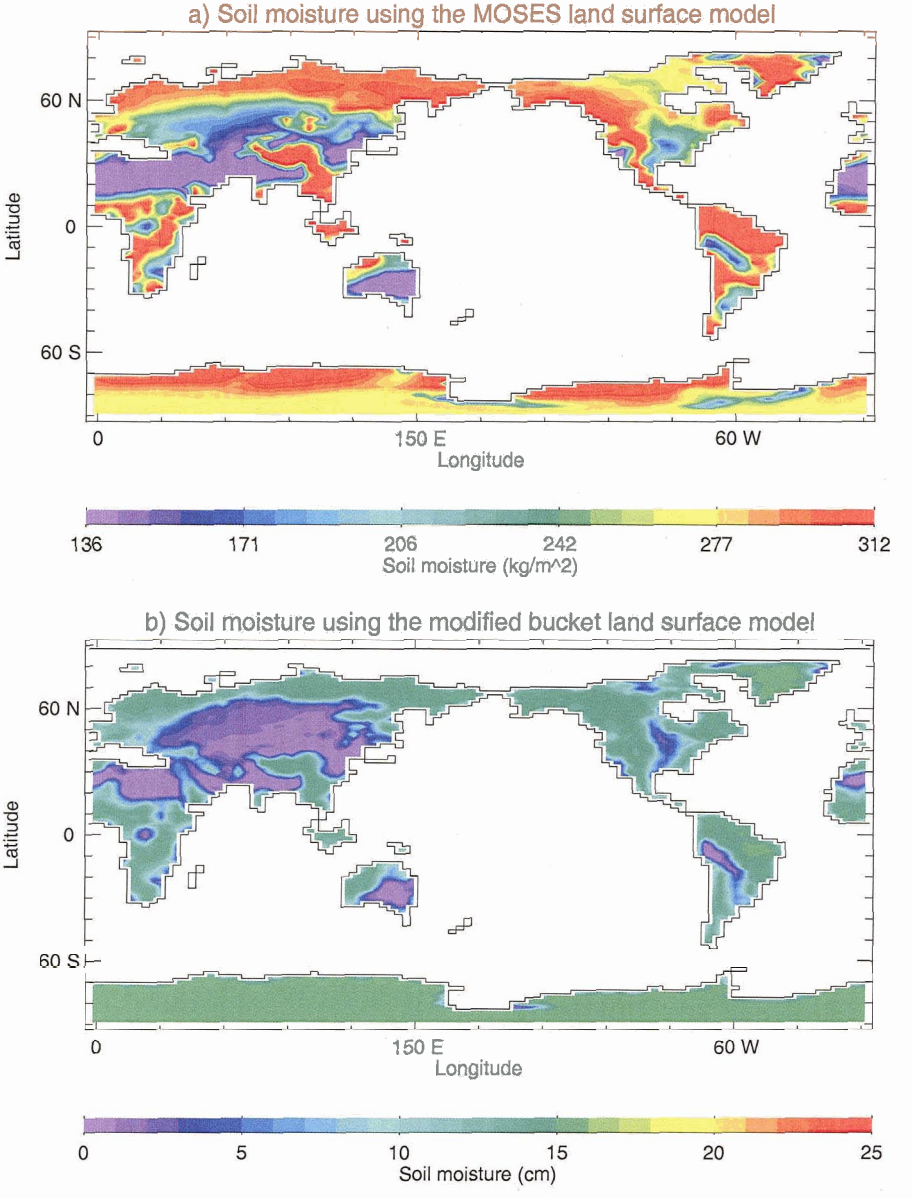

Figure 2.10: Simulated soil moisture for (a) the MOSES land surface model compared to (b) the modified bucket land surface model. Values in (a) are plotted beginning at 136 kg/m^2, which corresponds to the level below which soil moisture is unavailable to vegetation (equivalent to 0 cm in the bucket model). Values in (b) are plotted in cm, where 1 cm of soil moisture in the bucket corresponds to 10 kg/m^2 of soil moisture in a 1 meter thick soil layer. The colour bar in (b) is adjusted so that the maximum bucket depth (15 cm) corresponds with the critical soil moisture in MOSES above which plant stomata are not sensitive to soil moisture (242 kg/m^2).

from the previous land surface model to include a soil heat flux G_i:

$$R_{NET,i} = LE_i + SH_i + G_i \tag{2.18}$$

This ground heat flux (G_i) is calculated as a function of the temperature difference between the surface ($T_{s,i}$) and soil (T_{Soil}) temperatures:

$$G_i = 2\lambda \frac{(T_{s,i} - T_{Soil})}{\Delta z} \tag{2.19}$$

where λ is the soil conductivity, and Δz is the thickness of the soil layer (1 meter). This heat is stored in the soil layer, and the soil temperature (T_{Soil}) is calculated as a function of G and the energy required to melt snow. This version of MOSES, as well as its coupling to the UVic ESCM, is described more extensively in Meissner et al. (2003).

2.3 Carbon Cycle Model

In addition to simulating vegetation distributions, MOSES and TRIFFID calculate terrestrial carbon stores and fluxes. Carbon taken up by plant growth is defined as the gross primary productivity (GPP), and is calculated as a function of atmospheric carbon dioxide, solar radiation, soil moisture, temperature and nutrients. Nitrogen does impose a limit on photosynthesis, though the terrestrial nitrogen cycle is not currently included as a dynamic component of the model. Autotrophic plant respiration releases a portion of the carbon taken up by GPP back to the atmosphere, with the balance of carbon making up the vegetation net primary productivity (NPP). The photosynthesis model used here is based on the previously developed leaf-level photosynthesis models for C3 and C4 plants (Collatz et al. 1991, 1992); in this approach, photosynthesis calculations are coupled with the calculation of moisture fluxes

through plant stomata (as represented by the stomatal conductance or canopy resistance terms described in the previous section). The resulting carbon fluxes, calculated as a function of changing atmospheric carbon dioxide and climate conditions, determine the distribution of vegetation in the model and the response of vegetation to climate changes.

Carbon is transfered to the soil through litterfall and vegetation mortality, and its decay results in a return of accumulated carbon to the atmosphere. This soil or heterotrophic respiration (R_H) is calculated as a function of climatic conditions (temperature and soil moisture) and soil carbon stores (C_s):

$$R_H = R_H^* \cdot C_s \cdot F(T_s) \cdot F(\Phi) \tag{2.20}$$

In this formulation, R_H^* is the specific soil respiration rate (set to a constant value per unit soil carbon) at 25 °C and optimal soil moisture. $F(T_s)$ and $F(\Phi)$ are functions that modify the specific soil respiration rate based on soil temperature (T_s) and soil moisture (Φ). These functions are shown in Figure 2.11. The soil respiration rate increases exponentially as a function of soil temperature. This relationship is parameterized by means of a "Q_{10}" formulation:

$$F(T_s) = Q_{10}^{(0.1 \cdot (T_s - 25))} \tag{2.21}$$

In this formula, Q_{10} is set to a spatially and temporally constant value of 2.0, which results in a temperature factor that doubles the soil respiration rate with every 10 °C increase in soil temperature. This relationship has the potential to generate strong positive feedbacks to climate, as will be discussed further in Chapter 5. The effect of soil moisture on soil respiration is less dramatic – soil respiration decreases linearly in either direction from the optimal soil moisture value that occurs at 65% saturation. Below 30% saturation, soil respiration occurs at a constant rate equal to 20% of its

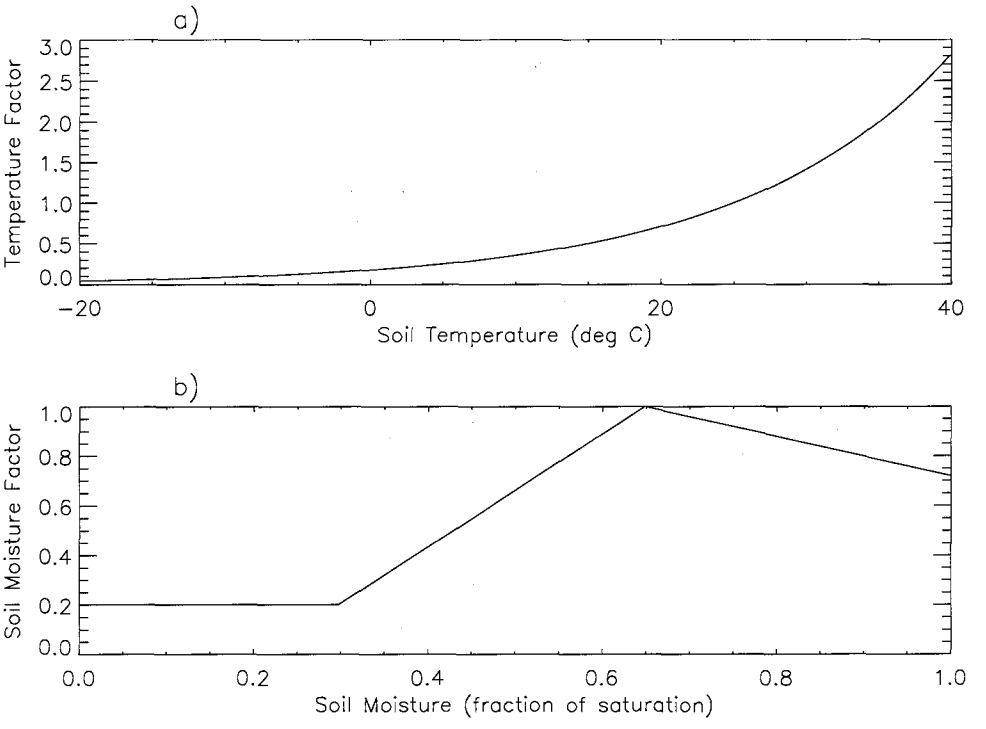

Figure 2.11: **Factors controlling the soil respiration rate as a function of (a) soil temperature and (b) and soil moisture.**

optimal rate.

Under equilibrium simulations, stable conditions arise when carbon taken up by NPP is equal to the carbon released by heterotrophic respiration in the soil. The difference between NPP and soil respiration is the net ecosystem productivity (NEP). In the absence of anthropogenic or natural disturbances, NEP represents the net flux of carbon from the atmosphere to the terrestrial biosphere. Anthropogenic disturbances, such as deforestation and agriculture, or natural disturbances, such as fire and insect outbreaks, generate additional releases of carbon to the atmosphere. When these are included, net uptake by the terrestrial biosphere is referred to as the net biome productivity (NBP). As TRIFFID does not model carbon fluxes from natural disturbances, the NBP in the UVic terrestrial carbon cycle model is simply the difference

between NEP and carbon emissions from anthropogenic land cover change ($E_{(lcc)}$):

$$F_{(land)} = NPP - R_H - E_{(lcc)} \tag{2.22}$$

At equilibrium, the net terrestrial carbon flux is equal to zero, with a small interannual variability on the order of 0.05 GtC/year. At present, TRIFFID does not include a parameterisation for the CO_2 emissions that result from imposed land cover change. As such, land cover change emissions of CO_2 are specified from estimates (Houghton 2003a), rather than being calculated directly as a function of the distribution of land cover changes in the model.

Under perpetual pre-industrial conditions (atmospheric CO_2 held fixed at 280 ppmv), the model simulates a globally averaged NPP and soil respiration of 63 GtC/year (where 1 GtC is equal to 10^{15} grams of carbon). The distribution of modelled NPP is shown in Figure 2.12. For comparison, a recent estimate of global NPP derived from satellite measurements of vegetation properties by the NASA Moderate Resolution Imaging Spectroradiometer (MODIS) is shown in the bottom panel of Figure 2.12. While the globally averaged NPP simulated by the model is quite close to observations (60 GtC/year: Prentice et al. 2001), the spatial distribution of NPP is more diffuse, with tropical NPP values in particular spread over a larger area than in the observed distribution. The simulated spatial distribution of NPP reflects the distribution of precipitation in the model, which is also more diffuse than is observed (see Figures 2.2 and 2.3). In addition, the modelled global NPP value of 63 GtC occurs under pre-industrial CO_2 conditions, whereas present-day observations of NPP correspond to present-day CO_2. While it is not clear to what extent historical increases in atmospheric CO_2 have increased NPP, it is possible that the model is overestimating pre-industrial vegetation productivity. Again, this can likely be linked to precipitation in the model, which is on the order of 20 percent too high on the

global average. Too much precipitation leads to wetter soil moisture conditions in the model, and significantly reduces the soil moisture constraint on photosynthesis.

Total simulated above-ground storage of carbon (vegetation biomass) is close to 800 GtC; storage of carbon in the soil totals 1050 GtC. The vegetation carbon store simulated by the model is about 25 percent higher than current estimates (650 GtC, Saugier et al. 2001), while simulated soil carbon is less than available estimates (1550 GtC, Prentice et al. 2001, Saugier et al. 2001). These discrepancies between simulated and observationally-based estimates of carbon stocks could be linked to a number of factors that are not adequately represented in the present simulations: (1) where anthropogenic land cover changes are specified, only croplands are accounted for, resulting in an under-representation of the actual extent of terrestrial vegetation modified by human activities; (2) the effects of natural disturbances (such as fires and insect outbreaks) on total vegetation carbon stores may not be sufficiently represented in the vegetation model; (3) too much vegetation carbon follows from an overestimate of NPP as discussed above; (4) river fluxes of carbon from terrestrial stores to the ocean are not included; (5) a single 1-meter soil layer would not be expected to capture the full extent of carbon in a realistic soil profile; and (6) peatlands, which represent a large portion of estimated global soil carbon stores, are not included in the soil carbon model. The equilibrium climatology of this model and comparison to observations is discussed in more detail in Meissner et al. (2003).

The terrestrial carbon cycle is combined in this model with an inorganic ocean carbon cycle, based on the Ocean Model Intercomparison Project (OCMIP) implementation (Orr et al. 1991). The model simulates dissolved inorganic carbon (DIC) as a passive tracer in the ocean, as well as carbon fluxes between the ocean and the atmosphere. The flux of CO_2 across the air-sea interface is calculated as a function

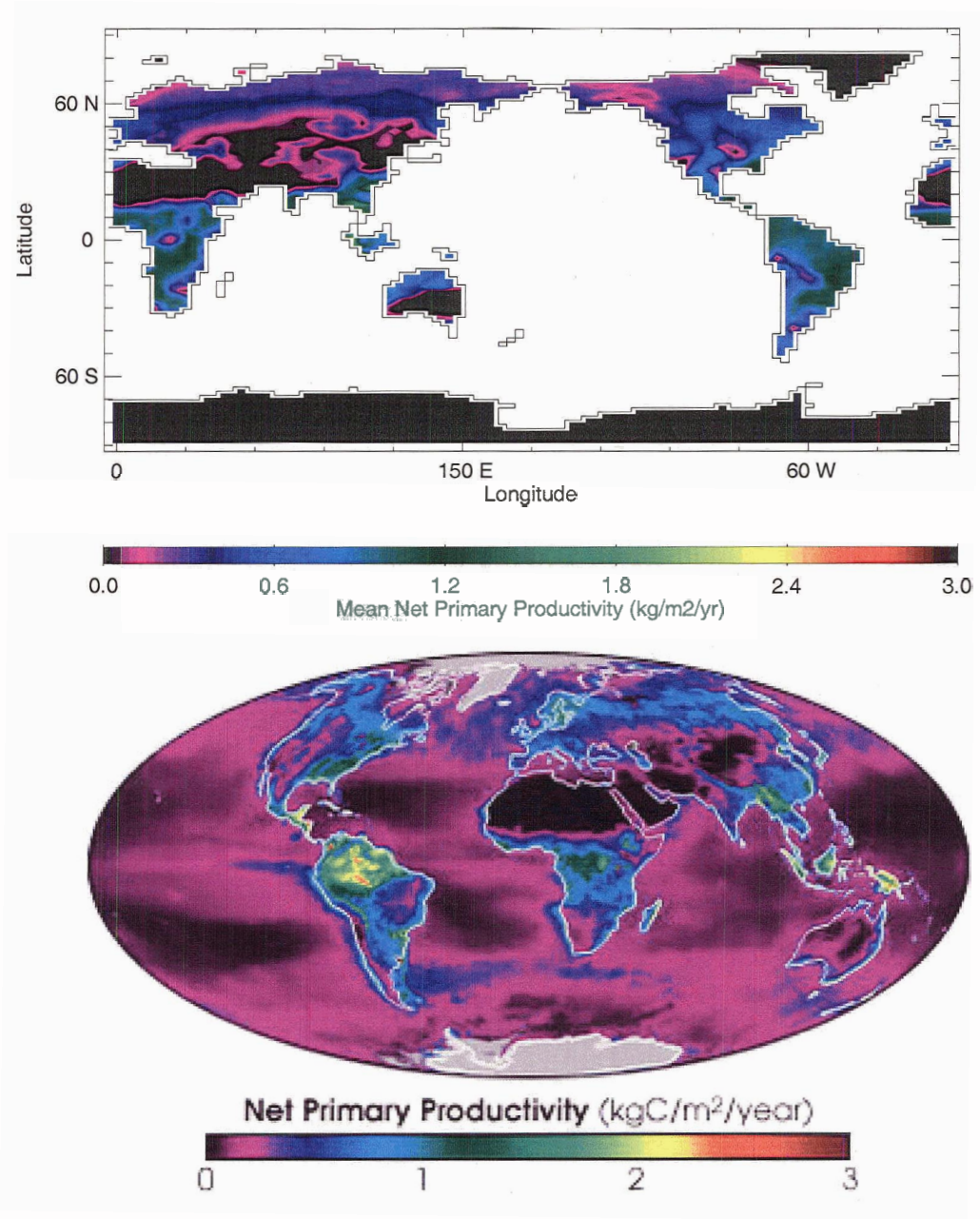

Figure 2.12: Modelled global net primary productivity for a pre-industrial equilibrium with CO_2 set to 280 ppmv (top) compared to an estimate of global net primary productivity from MODIS satellite measurements (bottom), (Courtesy of NASA Earth Observatory news archives: http://earthobservatory.nasa.gov/Newsroom/NasaNews/2003/2003042214379.html).

of the CO_2 gradient between the atmosphere and the surface layer of the ocean:

$$F_{(ocean)} = k_w(CO_{2(atm)} - CO_{2(ocean)}) \tag{2.23}$$

where k_w is the transfer velocity, calculated as a function of sea surface temperatures, wind speed and sea ice coverage (Weaver et al. 2001, Ewen et al. 2004). The equilibrium inorganic carbon storage in the ocean totals 31,000 GtC. As this total does not include dissolved organic carbon, or particulate organic/inorganic carbon, it would be expected that the model would fall short of the full 38,000 GtC estimate given in Prentice et al. (2001).

At present the global carbon cycle represented in the UVic ESCM does not include a biological ocean component. This is consistent with the assumption of a constant biological carbon cycle in the ocean that is not sensitive to anthropogenic emissions of atmospheric carbon dioxide. This view is supported by the following statement from Houghton et al. (2001):

> Despite the importance of biological processes for the ocean's natural carbon cycle, current thinking maintains that the oceanic uptake of anthropogenic CO_2 is primarily a physically and chemically controlled process superimposed on a biologically driven carbon cycle that is close to steady state. This differs from the situation on land... (p. 199)

In other words, it can be assumed that the biological ocean carbon cycle does not play a role in the uptake of anthropogenic carbon. As such, the transient response of the carbon cycle to anthropogenic perturbations can be investigated by focusing on inorganic carbon in the ocean and on the dynamics of the terrestrial biosphere.

In a transient simulation, this global carbon cycle model allows atmospheric CO_2 to be computed prognostically as a function of ocean-atmosphere and land-atmosphere carbon fluxes, as well as specified anthropogenic emissions. The net flux

of carbon to the atmosphere at each model timestep (in ppmv/s) is calculated as:

$$F_{(atm)} = (E_{(ff)} - F_{(ocean)} - F_{(land)})/2.1 \tag{2.24}$$

where $E_{(ff)}$ is the anthropogenic emission of carbon from fossil fuel combustion and $F_{(ocean)}$ and $F_{(land)}$ are the net uptakes by the ocean and land respectively (GtC/s). Emissions of carbon from land cover change, though specified as a model forcing in transient simulations, are included here as a component of $F_{(land)}$. The factor 2.1 represents the conversion from units of GtC/s to ppmv/s. This number is calculated based on the molecular volume of an ideal gas and an assumed 8.5 km atmospheric scale height, and is consistent with the conversion used by other models (see for example Berthelot et al. 2002).

In Chapters 3 (Section 3.3) and 5 the UVic ESCM global carbon cycle model is enabled. Transient climate simulations are carried out beginning from the pre-industrial equilibrium described above, and forced by anthropogenic carbon dioxide emissions from fossil fuel combustion and land cover change. Anthropogenic emissions of carbon dioxide from fossil-fuel combustion are specified from Marland et al. (2002); land-use emissions are specified from Houghton (2003a). These emissions (shown in Figure 2.13) impose a perturbation on the equilibrium spin-up state, and the land and ocean carbon stores and fluxes respond dynamically to the imposed increase in atmospheric carbon dioxide. The computed atmospheric carbon dioxide concentration is the resulting CO_2 in the atmosphere after global carbon sinks have responded to anthropogenic emissions.

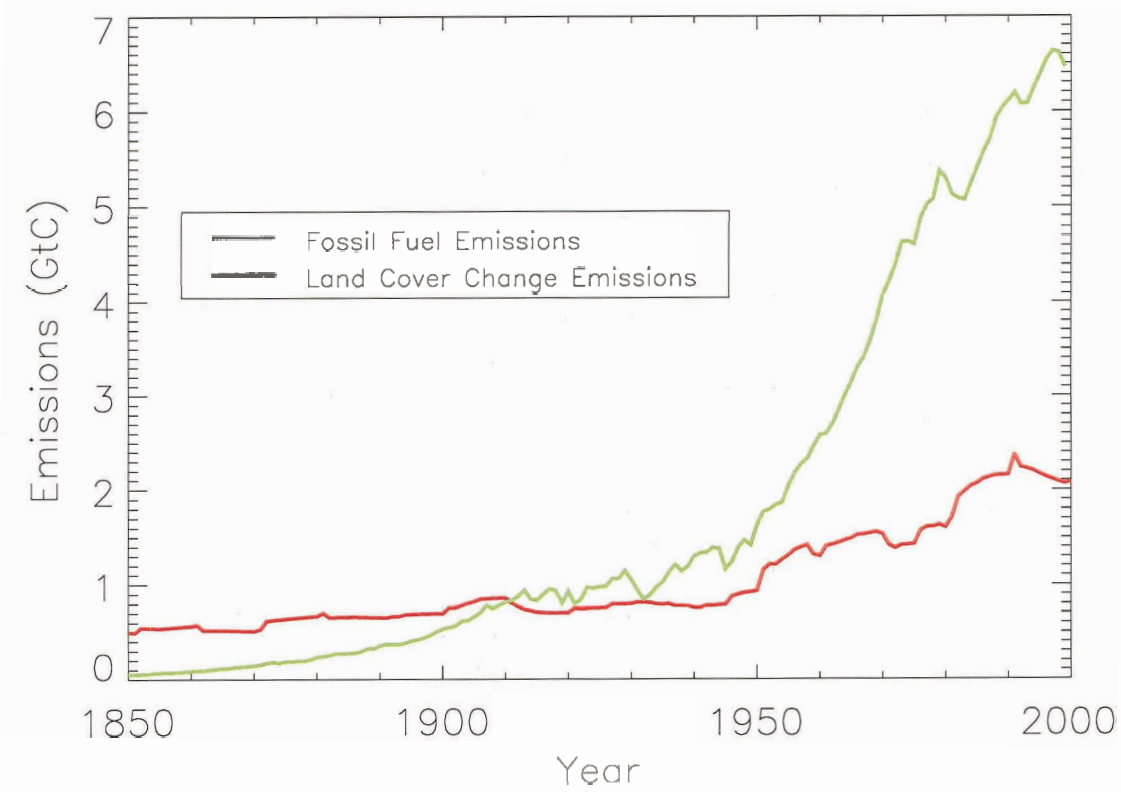

Figure 2.13: **Anthropogenic carbon dioxide emissions from land cover change (red line) and fossil fuels (green line).**

Chapter 3

Historical Land Cover Change

3.1 Introduction

In the study of anthropogenic climate change, there is a growing interest in the ways that human activities interact to affect the climate system. In particular, human land-use over the last several centuries, through large scale changes to the global vegetation cover, has had a potentially significant effect on global climate. These land cover changes have recently been quantified in global datasets that provide estimates of historical land cover change over the past three centuries (Ramankutty and Foley 1999, Klein Goldewijk 2001). These datasets now allow for an historically realistic analysis of land cover change using general circulation climate models.

Land cover change can influence global climate in a number of ways, by altering parameters such as leaf area index, root distribution, soil water holding capacity, surface resistance to evapotranspiration, surface albedo, snow-masking depths and fluxes and storage of carbon and other nutrients (see for example Betts 2001, Bolin et al. 2000). The effects of land cover change on climate can be separated into two broad categories: those that result from physical changes to the land surface and vegetation cover (biogeophysical effects), and those that result from altered fluxes of carbon dioxide (biogeochemical effects).

Biogeophysical effects of historical land cover change on climate were highlighted in a review of contemporary climate forcings by Hansen et al. (1998). Here, the authors concluded that the radiative forcing due to historical land cover change from

1850 to 1998 was -0.2 ± 0.2 W/m^2, resulting in a global cooling of -0.14 °C. The primary mechanism for this cooling is the increase in surface albedo that results when forest land cover types are replaced by cropland or pasture. This effect is particularly important in higher latitudes, where the snow-masking effect of vegetation is greatly reduced as a result of forest to cropland conversion (Hansen et al. 1998).

Several recent studies using reduced complexity climate models have also found a global cooling as a result these biogeophysical effects of historical land cover change. Brovkin et al. (1999) and Bauer et al. (2003) reported that historical deforestation over the last millennium induced a global cooling of -0.35 °C. Bertrand et al. (2002) reported a smaller effect: in their model, land cover change led to a cooling of -0.1 °C over the same time period. All of these studies prescribed transient scenarios of land cover change over the period of time studied.

A number of equilibrium studies using atmospheric general circulation models (AGCMs) have also noted both regional and global effects. Betts (2001) found that the global temperature was only -0.02 °C cooler in a comparison between present-day and pre-industrial vegetation equilibria, but noted stronger cooling (in the range of -1 to -2 °C) in the northern mid-latitudes in winter and spring. Bounoua et al. (2002) and Zhao et al. (2001) also determined globally-averaged changes to be small, but found significant regional and seasonal changes, both warming and cooling. Chase et al. (2000, 2001) found land cover change to have significant impacts on atmospheric circulation, particularly in the Northern hemisphere winter, and further argued that near-surface regional temperature anomalies due to land cover changes may be of similar magnitude to transient changes due to carbon dioxide and sulphate aerosol forcing. Govindasamy et al. (2001), in an AGCM/slab-ocean equilibrium comparison found a global cooling of -0.25 °C, and went so far as to suggest that reconstructed Northern hemisphere cooling trends over the past millennium could be largely the result of anthropogenic land cover change.

Compounding the issue of the climatic effect of land cover change is the contribution of land conversion to climate warming as a result of large emissions of carbon dioxide (Bolin et al. 2000). A number of studies have provided estimates of emissions associated with land cover change; most recently Houghton (2003a) estimated a total release of 156 GtC between 1850 and 2000. Only a couple of modelling studies have attempted to assess the net effect of land cover change on climate by including both the biogeophysical effects of changes to the land surface as well as the biogeochemical effects of carbon emissions (Betts 2000, Claussen et al. 2001). Betts (2000) compared the biogeochemical and biogeophysical effects of reforestation in northern mid-latitudes. It would be expected that in the case of reforestation, the biogeophysical effects might lead to a local warming, just as deforestation leads to a biogeophysical cooling. In this study, Betts found that in some cases, this biogeophysical warming actually exceeded the counteracting cooling effect of carbon uptake. Claussen et al. (2001) demonstrated that the net effect of land cover change, either in the case of deforestation or afforestation, is highly dependent on the latitude at which land cover change occurs: at high northern latitudes, there is a positive relationship between the extent of forest cover and temperature, whereas in the tropics and subtropics, the relationship is negative. These studies concluded that deforestation occurring at high latitudes would likely result in a net cooling, whereas in the tropics, a net warming is more likely.

In a recent sensitivity study, Myhre and Myhre (2003) suggested that model results on the effect of land cover change are highly sensitive to specified vegetation datasets and surface albedo values. Considering the range of vegetation albedo values and land cover change datasets available, they found a large range of radiative forcings: between -0.6 and $+0.5$ W/m^2, although they noted that positive radiative forcing results only occurred using extreme combinations of land cover change scenarios and surface albedo values, which are likely unrealistic. Nevertheless the large range of

land cover change radiative forcing presented in their study, as well as the range of radiative forcing and temperature results from previous studies of land cover change highlight the need for further study in this area.

In this chapter, I first describe a preliminary exploration of the radiative effect of land cover change using the earliest version of the UVic Earth System Climate Model (Section 3.2.1). This model includes the modified atmospheric moisture transport and radiative transfer schemes described in Sections 2.1.2 and 2.1.3. The land surface model is as described in Section 2.1.4 (the modified bucket land surface model), though in these preliminary experiments only surface albedo and roughness length are allowed to vary with vegetation type. Snow masking depth is held constant at 1 meter for all vegetation types, and surface resistance is not included in the parameterisation of evaporation. In addition, snow albedo is not specified as a fixed value, but rather as an increase of 0.18 applied to the local surface albedo.

These preliminary experiments are followed by a series of land cover change sensitivity experiments using varying datasets and model configurations (Section 3.2.2). The version of the model used in this series of experiments incorporates all of the modifications outlined in Sections 2.1.2 though 2.1.4. The land surface model used here is fundamentally the same as that used in Section 3.2.1, with the inclusion of vegetation snow masking depths and surface resistances as variable surface parameters. Additionally, in these experiments, the snow albedo is set to a fixed maximum value of 0.45. In Section 3.2.2, a series of land cover change equilibrium experiments are described and presented, highlighting the important processes and model sensitivities found in this study. These experiments produce a range of results that illustrate the biogeophysical effect of historical land cover change on climate.

I conclude this chapter with an analysis of the biogeochemical effect of land cover change that results from land-use emissions of greenhouse gases (Section 3.3). These experiments use the coupled terrestrial and inorganic ocean carbon cycle models de-

scribed in Section 2.3. The land surface model used in this section is the MOSES model, described in Section 2.2.2. This new land surface model is required for coupling with the dynamic vegetation model TRIFFID (Section 2.2.1), and the calculation of carbon fluxes that make up the terrestrial component of the global carbon cycle model. Results from this coupled climate carbon cycle model are used to estimate the biogeochemical effects of historical land cover change. This biogeochemical effect is compared to the biogeophysical effects presented in Sections 3.2.1 and 3.2.2 to generate an estimate of the net effect of historical land cover change on climate over the past 300 years.

3.2 Biogeophysical Effects of Historical Land Cover Change

3.2.1 Preliminary Experiments

3.2.1.1 Experimental Descriptions

The model results presented in this section are from three 2000 year equilibrium runs and four transient model runs covering the period from 1700 to 1992. The croplands dataset used is that of Ramankutty and Foley (1999), which provides a potential or natural vegetation field (representing vegetation distributions in the absence of human disturbance) and fractional cropland areas at each gridcell yearly from 1700 to 1992. As Ramankutty and Foley (1999) considered only historical changes in cropland area, and not other land cover changes such as pasture and extensively logged areas (see also Klein Goldewijk 2001), their dataset could be expected to generate a lower bound on the estimate of the radiative effect of land cover changes. The version of the UVic ESCM used here is as described in Section 2.1. However, of the vegetation-type dependent surface parameters given in table 2.1, only surface albedo and surface roughness length are altered by imposed land cover changes. In

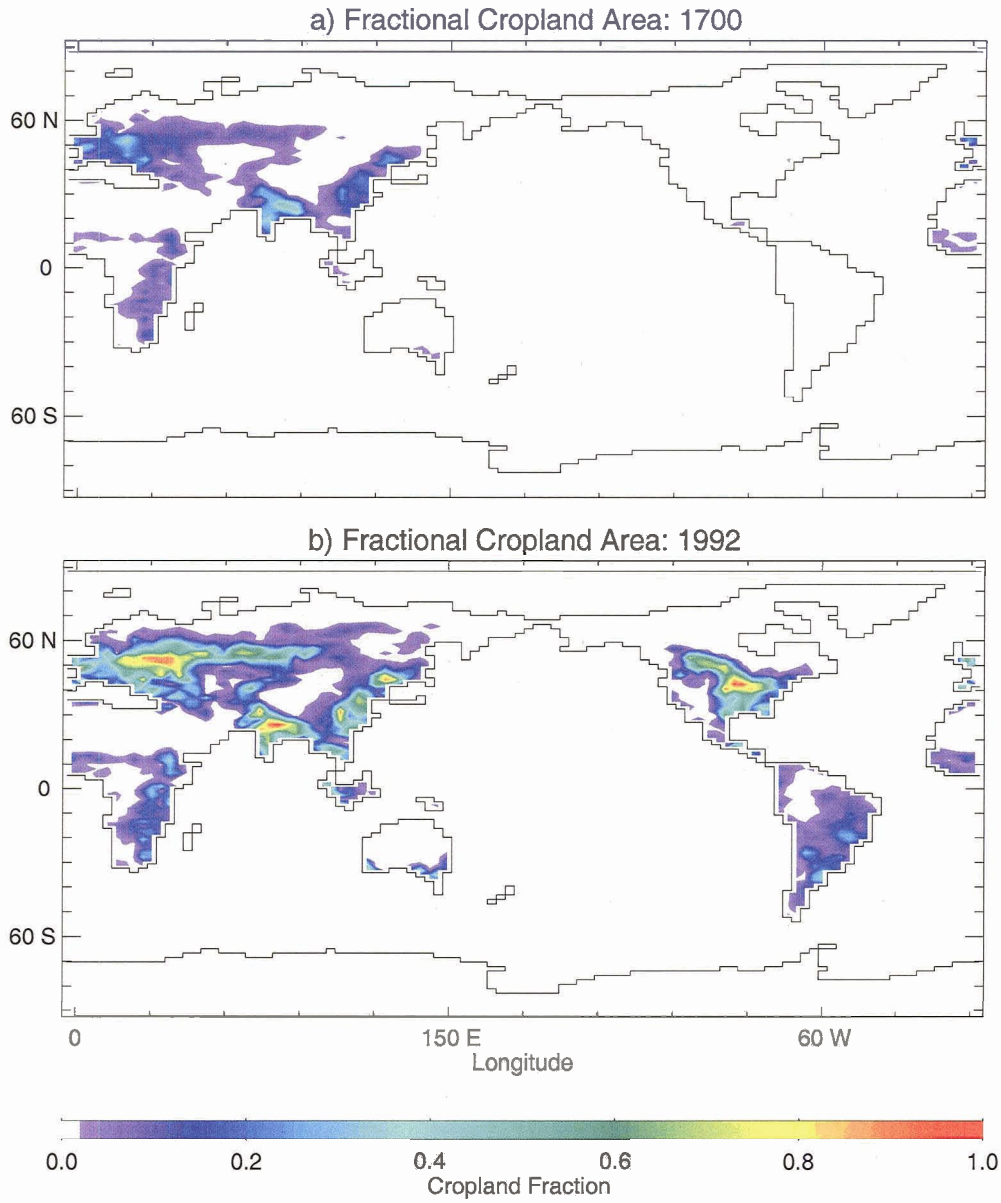

Figure 3.1: **Fractional cropland areas for year 1700 (top) and 1992 (bottom), from Ramankutty and Foley (1999).**

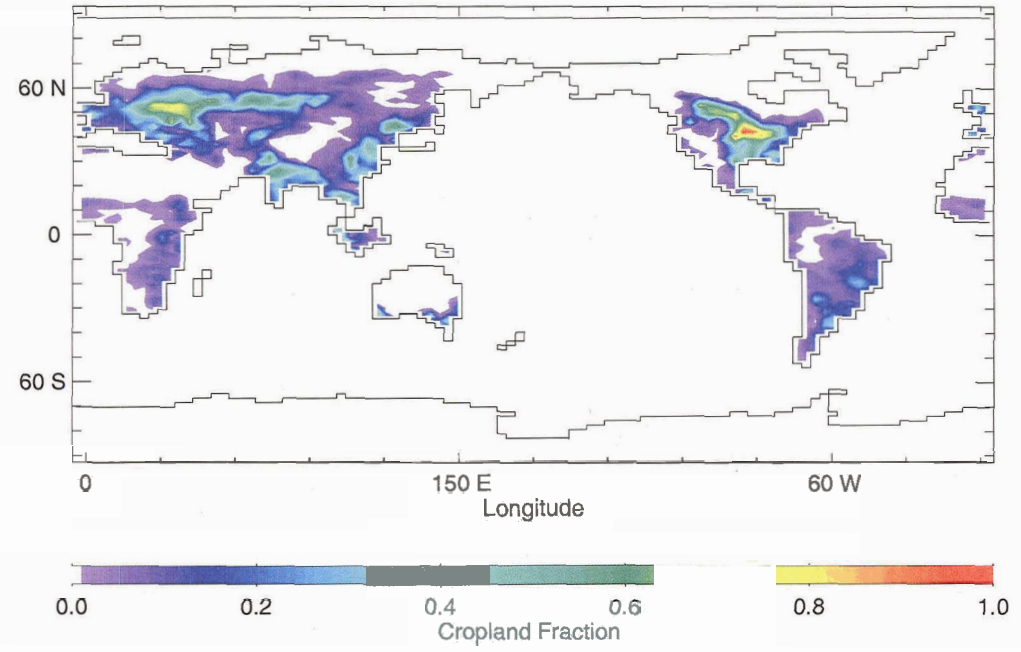

Figure 3.2: **Increase in fractional cropland area on the model grid from year 1700 to 1992 for the Ramankutty and Foley (1999) dataset.**

this initial exploration, surface resistance and vegetation snow masking depths were excluded as variable parameters.

The three equilibrium runs presented here are differentiated by the specified vegetation fields. Equilibrium (1) used present-day vegetation as determined from satellite data (DeFries and Townsend 1994). Equilibria (2) and (3) used the fractional cropland areas of Ramankutty and Foley (1999) corresponding to years 1700 and 1992, respectively (as shown in Figure 3.1), superimposed onto the potential vegetation field. Vegetation types for the satellite-derived and potential vegetation distributions are shown in Figure 3.3. All three equilibria use present-day CO_2 concentration (365 ppm) and orbital parameters. As the croplands dataset used here does not include all land cover changes that have occurred since 1700, it would be expected that equilibrium 1 (satellite-derived vegetation) will show a stronger land cover signal than equilibrium 2 (1992 croplands) when compared to equilibrium 3 (1700 croplands). Differences in the definition and placement of vegetation types between the two veg-

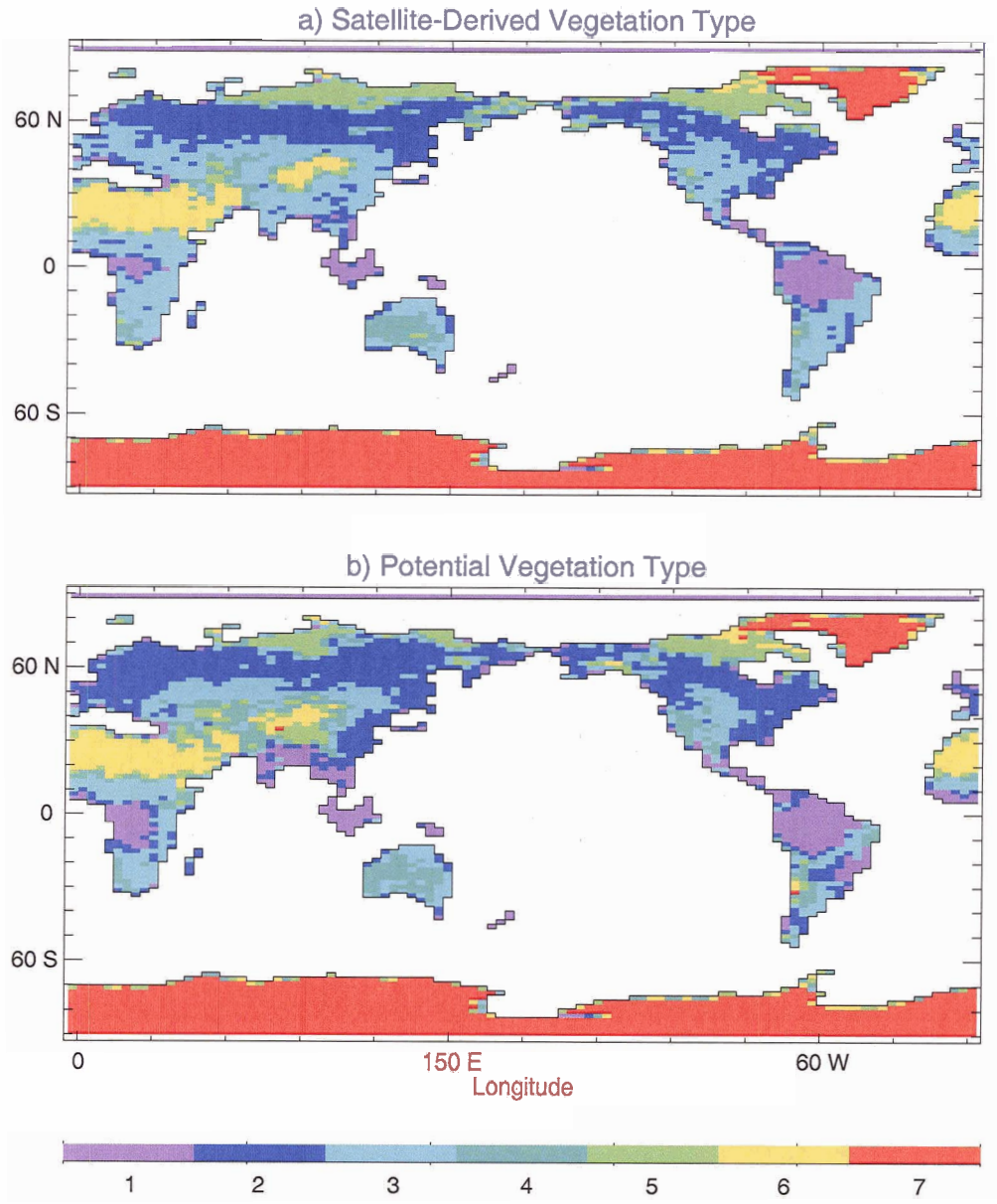

Figure 3.3: Satellite-derived present-day vegetation from DeFries and Townsend (1994) (top) and potential natural vegetation from Ramankutty and Foley (1999) (bottom). Numbered vegetation types correspond to: (1) Tropical Forest (mauve); (2) Temperate/Boreal Forest (blue); (3) Grassland/Savanna/Cropland (cyan); (4) Shrubland (turquoise); (5) Tundra (green); (6) Desert (tan); and (7) Rock/Ice (red).

etation datasets do have the potential to have a confounding influence on the land cover signal in equilibrium (1), but this was nevertheless a useful experiment to estimate the effect of land cover changes not captured in the Ramankutty and Foley (1999) dataset.

Transient climate simulations began from a control equilibrium climate defined by year 1700 land cover (as in equilibrium 3 above), pre-industrial CO_2 (280 ppm) and year 1700 orbital parameters. This control equilibrium was spun up for 1700 years, and transient simulations were run from year 1700 to present. The three transient runs were forced by: (1) changing croplands (land cover) only; (2) changing CO_2; and (3) changing land cover and atmospheric CO_2. A control experiment (4) was also conducted with changing orbital parameters, but not other radiative forcings. In runs 1 and 3, croplands were specified yearly from 1700 to 1992, and surface albedos and roughness lengths were changed according to the fractional cropland area in each gridcell. CO_2 increases in runs 2 and 3 were specified beginning in 1850 as an exponential increase to present-day values according to the formula:

$$[CO_2] = 280.0 \cdot exp(0.0018(year - 1850)) \tag{3.1}$$

As a result of the portion of the exponential curve that was applied to years from 1850 to 2000 by this formula, the actual increase in CO_2 was quite close to linear over this time period. Solar orbital forcing was also specified from 1700 to 2000, though this forcing would be expected to have a negligible effect on model results and hence provided a baseline against which the other runs can be compared (a "control" transient run).

3.2.1.2 Equilibrium Results

Results of the equilibrium model runs are presented as differences: (a) satellite-derived vegetation equilibrium minus year 1700 croplands equilibrium; and (b) year 1992 croplands equilibrium minus year 1700 croplands equilibrium. Negative differences thus represent a decrease resulting from changes in land cover between the year 1700 and the present day.

Figure 3.4 shows zonally averaged temperature, precipitation and evaporation differences for comparisons (a) and (b). Both comparisons show a cooling and a decrease in precipitation at all latitudes. Comparison (a) shows a globally averaged cooling of $-0.22°C$ and an average precipitation decrease of -14.2 mm/year. While the spatial pattern is similar, the magnitude of the change shown for comparison (b) is less: a cooling of $-0.10°C$ and precipitation decrease of -3.3 mm/year. As can be seen in the shape of the temperature plot, cooling is amplified in the Northern hemisphere, consistent with the location of the majority of the specified land cover changes (see Figure 3.2). There is also an amplification at around 70°S, resulting from local sea-ice albedo feedbacks.

Much of the decrease in precipitation can be attributed to atmospheric temperature change. However, the large decreases seen in the tropics and sub-tropics can be further explained by examining the roughness lengths listed in Table 2.1. According to the parameterisation of evaporation in the bucket model, a smaller roughness length results in a larger aerodynamic resistance to evaporation and hence a smaller Dalton number and (given equal moisture availability) less evaporation. By changing roughness length alone, a much larger decrease in evaporation would be expected as a result of a conversion from forest to grassland in the tropics (a decrease in roughness length from 2.86 m to 0.11 m) than by a similar change in the temperate/boreal regions (a decrease in roughness length from 0.91 m to 0.11 m) (see Table 2.1). As such, the greatest evaporation (and hence precipitation) differences are seen in the

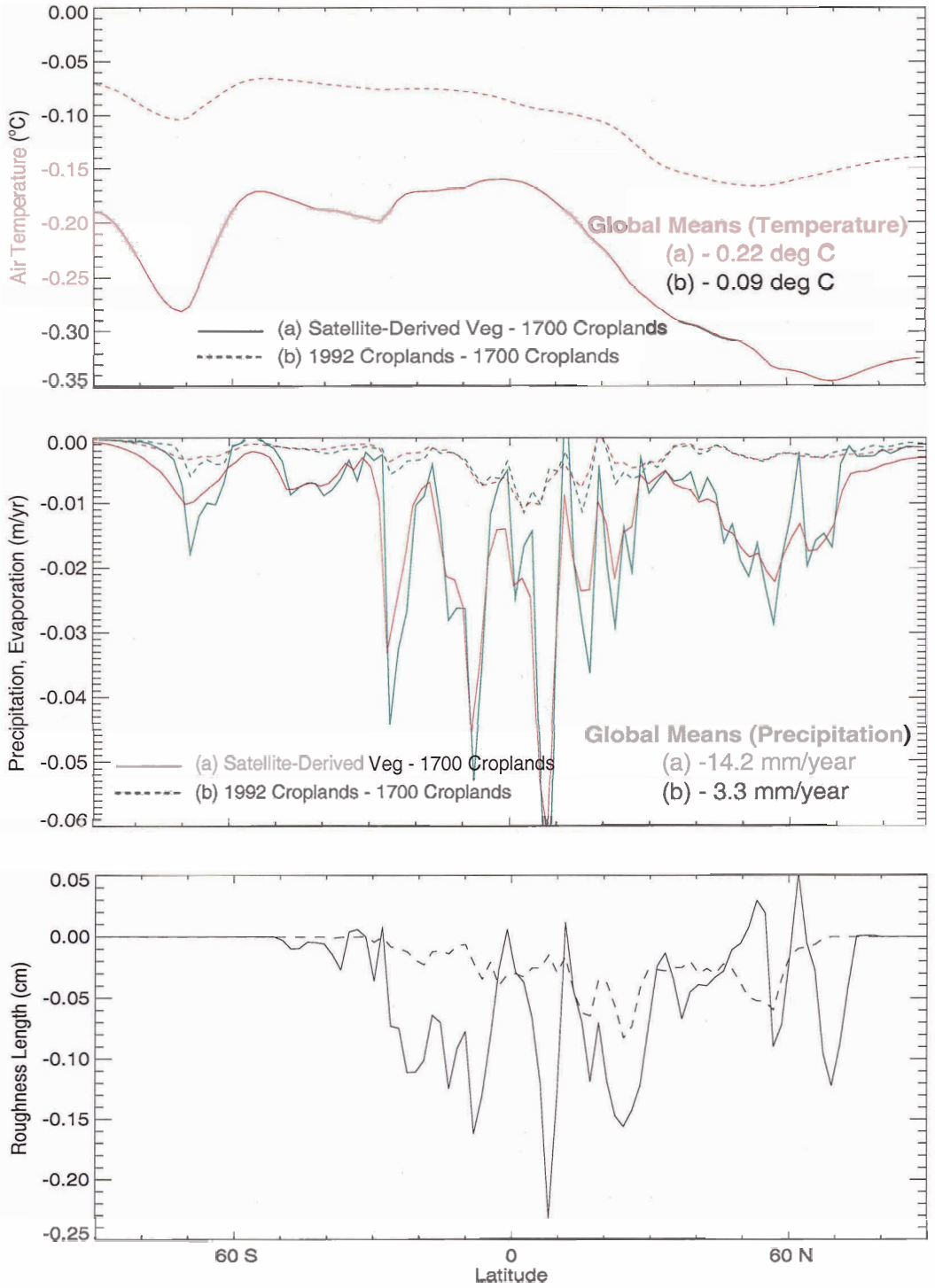

Figure 3.4: **Zonally averaged equilibrium temperature (top), precipitation (red lines, middle), evaporation (green lines, middle) and roughness length (bottom) differences for (a) satellite-derived vegetation – 1700 croplands (solid lines) and (b) 1992 croplands – 1700 croplands (dashed lines).**

tropics where roughness length changes are largest, with a less pronounced decrease seen in the northern mid-latitudes. This can be seen in Figure 3.4 by comparing the precipitation and evaporation changes (middle panel) with the changes in roughness length (bottom panel). Roughness length changes are largest in the tropics, and the zonal distribution of precipitation and evaporation changes follows closely the zonal pattern of roughness length changes that result from variability in the distribution of land cover changes at each latitude.

Spatially-varying temperature and precipitation differences are shown in Figures 3.5 and 3.6. While the majority of the temperature change can be seen in the Northern hemisphere, the largest local changes are the result of local snow and sea-ice albedo feedbacks. Particularly in the case of comparison (a), these positive feedbacks serve to amplify the cooling signal initiated by land cover change. Comparison (b) shows less cooling, but as in the case of the zonally averaged results, the spatial pattern of cooling is similar to (a). Precipitation changes for both comparisons are concentrated in the tropics (as in the case of the zonally averaged changes), and are largely localized in areas of large vegetation changes. Precipitation changes also reflect the local temperature changes seen in Figure 3.5. It is important to note here that as the model does not contain atmospheric variability (Weaver et al. 2001), the differences shown here represent significant changes in the climate mean state.

3.2.1.3 Transient Results

Transient runs were chosen to compare the relative importance of land cover and greenhouse gas forcing. The results of these runs are shown in Figure 3.7. The transient effect of land cover change is $-0.09°C$, quite close to that found in comparison (b) in the equilibrium results ($-0.10°C$). This indicates that there is little evidence of an oceanic cooling commitment associated with land cover change, as the majority of the temperature change seen in the equilibrium comparison is also seen in the

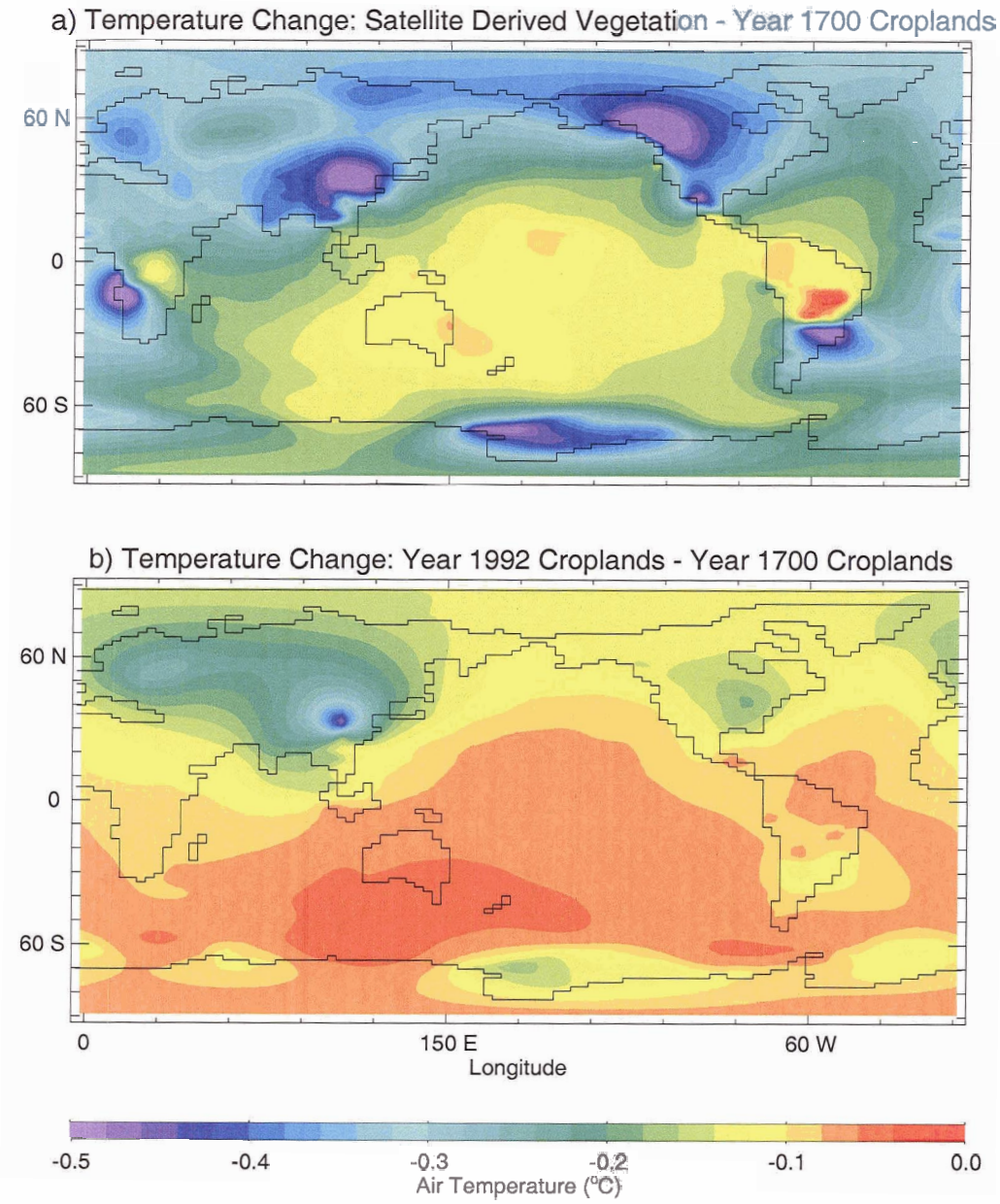

Figure 3.5: **Two dimensional temperature differences for equilibrium comparisons (a) satellite-derived vegetation – 1700 croplands (upper panel) and (b) 1992 croplands – 1700 croplands (lower panel).**

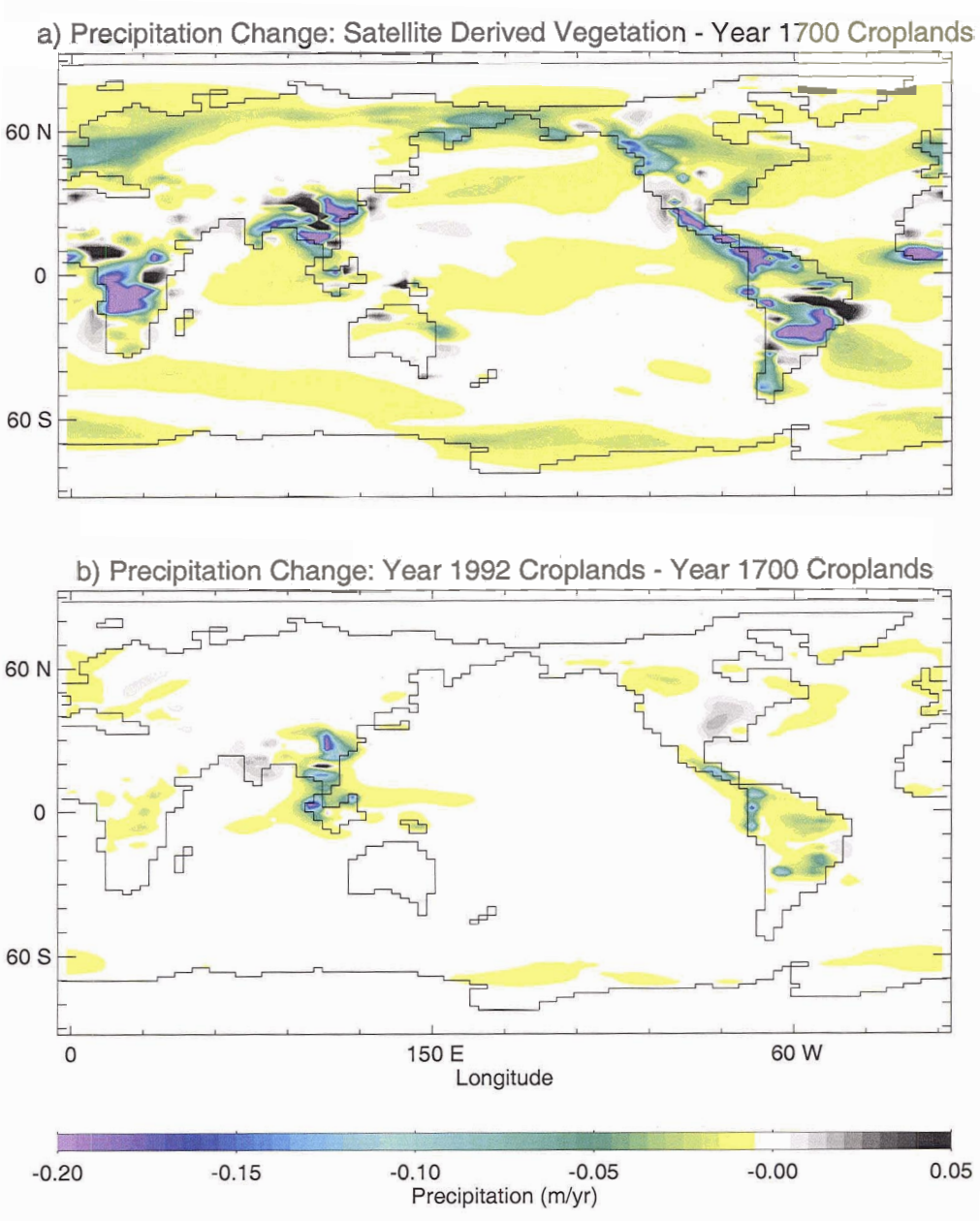

Figure 3.6: **Two dimensional precipitation differences for equilibrium comparisons (a) satellite-derived vegetation – 1700 croplands (upper panel) and (b) 1992 croplands – 1700 croplands (lower panel).**

transient run. While the land cover change effect on global temperature is smaller than that of CO_2 (+0.76°), it nevertheless has a noticeable dampening effect on the total warming when both forcings are combined (+0.68°C). It is also clear that land cover change is much larger than any model variability or orbitally induced response seen in the control run (+0.003°C).

To assess the magnitude of the radiative forcing associated with land cover change, Figure 3.8 shows the change in downward short-wave radiation absorbed at the surface for the land cover transient run. The change shown here results from a combination of land cover changes to surface albedo and snow/sea-ice albedo feedbacks. Comparison of Figure 3.8 with Figure 3.5b reveals a clear relationship between albedo-induced shortwave forcing at the surface and local temperature changes. The maximum local change in downward shortwave or -8.5 W/m^2 is located in Southeastern Asia, and corresponds to the maximum temperature change of -0.5 °C at this location. The globally averaged short-wave radiative forcing resulting from land cover change is -0.15 W/m^2, slightly less than, but within the error bounds of that found by Hansen et al. (1998). Transient changes in global temperature, evaporation, precipitation, and short-wave radiation for the four runs (as well as a fifth run described in the next section) are summarized in Table 3.1.

3.2.1.4 Surface Albedo Sensitivity

As shown in Table 2.1, the albedo value assigned to croplands in this model was 0.17. As a globally and temporally averaged albedo value for grassland, savanna and cropland vegetation types, this value reproduces well the satellite albedo data provided by Sellers et al. (1996). Previous studies of vegetation albedo, however, have provided widely varying cropland albedo values. Wilson and Henderson-Sellers (1985) gave albedo values for individual crop types that range from 0.12 to 0.25, with only rice having an albedo value of less than 0.17. Taken together, the above range corresponds to

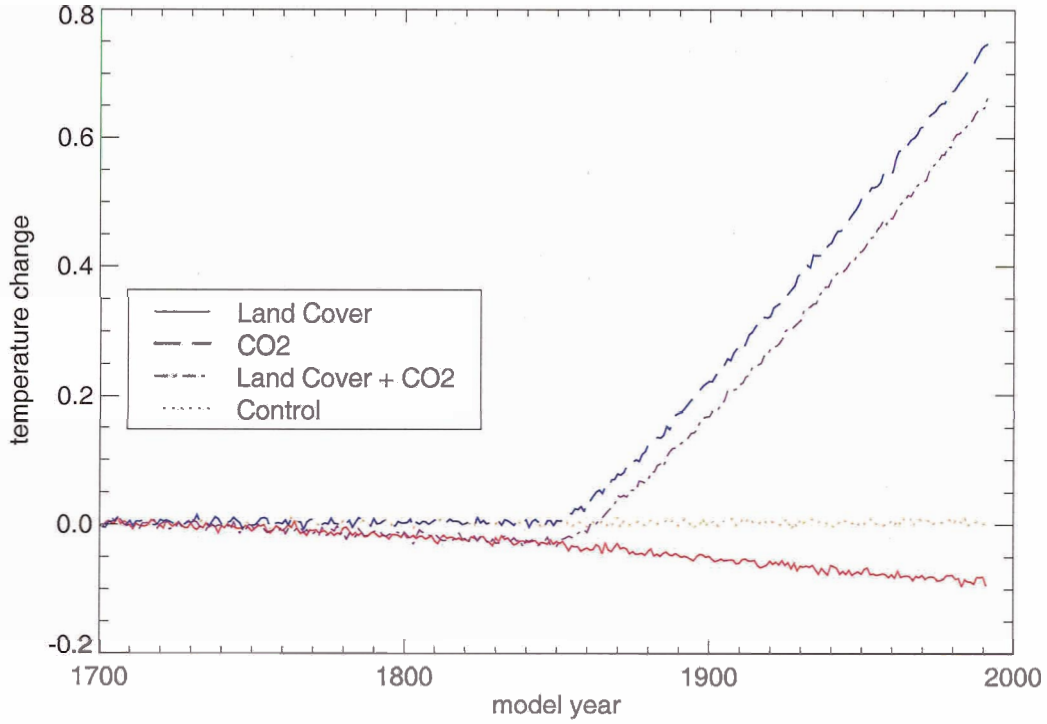

Figure 3.7: **Globally averaged temperature for four transient runs. Total temperature changes: (1) land cover only: $-0.09°$; (2) CO_2: $+0.76°$; (3) land cover + CO_2: $+0.68°$; and, (4) Control: $+0.003°$.**

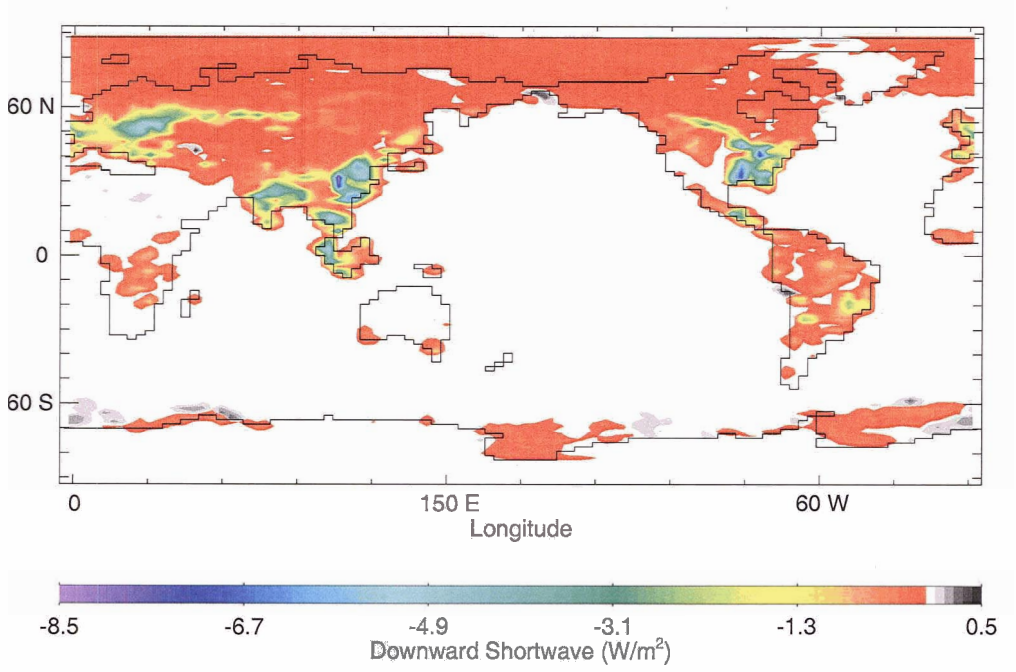

Figure 3.8: **Change in downward short-wave radiation absorbed at the surface for the land cover transient run.**

an average value of 0.2 (Myhre and Myhre 2003). The Surface and Atmospheric Radiation Budget (SARB) dataset (available online at http://snowdog.larc.nasa.gov/surf/index.html) assigned an albedo value of 0.15 to cropland and 0.16 to pasture, based on the work of Briegleb et al. (1986). Matthews (1983) gave a cropland albedo value of 0.18. While the chosen cropland albedo of 0.17 for the experiments described above falls in the middle of the range of values in the literature, in is not clear to what extent this choice affected the results discussed in this chapter.

In order to assess the model sensitivity to the specified cropland albedo, a second land cover transient run was performed using a cropland albedo value of 0.2 for all fractional cropland areas applied to the background vegetation field. This change almost doubled the albedo forcing associated with land cover change, as not only did forest gridcells show a 50 to 75% larger albedo increase as a result of conversion to cropland, but the albedo of grassland, savanna and shrubland gridcells was also increased from 0.17 to 0.2 in those areas where croplands were applied. In previous simulations, cropland albedo was equal to grassland, savanna and shrubland albedo values, and as a result, these gridcells did not see an albedo increase associated with cropland specification.

As can be seen in the last line of Table 3.1 and in Figure 3.9, a higher specified cropland albedo value has a large impact on the total temperature change for the transient run. Instead of a cooling of $-0.09°C$ as in the case of the original run, this second land cover transient run shows a much larger cooling of $-0.17°C$. Based on this result, it is clear that the surface albedo chosen for croplands can have a substantial impact on the magnitude of the global temperature change forced by land cover change.

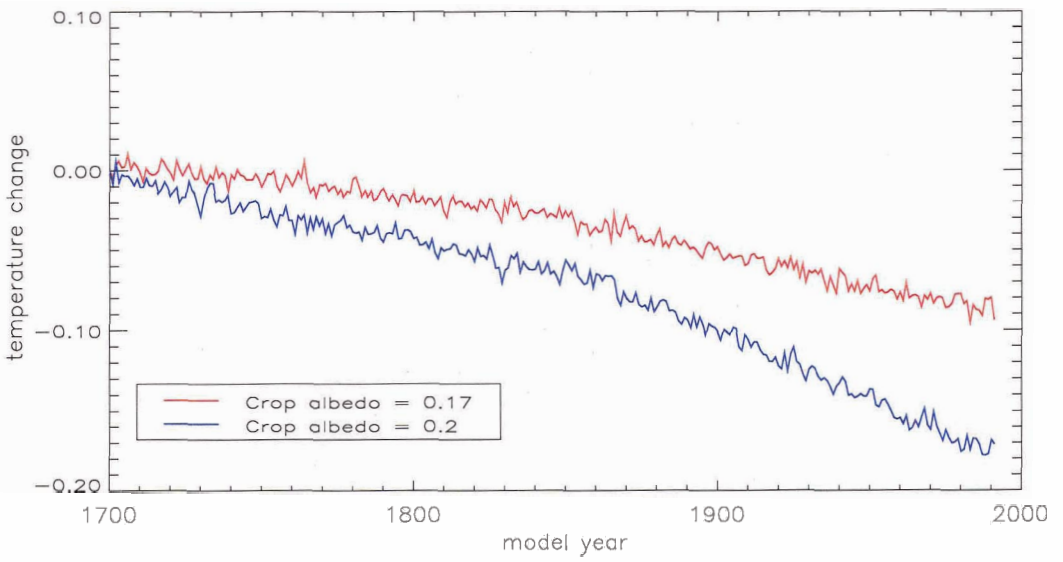

Figure 3.9: **Transient run showing the model's sensitivity to the specified cropland albedo. Shown in red is the initial transient run, with cropland albedo set to the default value of 0.17. For the transient run in blue, the cropland albedo was set to 0.2.**

Table 3.1: **Total changes in temperature, evaporation, precipitation and downward short-wave radiation absorbed at the surface for three preliminary transient model runs and a control run.**

Transient Model Run	T (°C)	E (mm/yr)	P (mm/yr)	↓SW (W/m^2)
1. Land Cover (LC) only	−0.09	−3.3	−3.3	−0.15
2. CO_2 only	+0.76	+12.1	+11.9	+0.06
3. LC + CO_2	+0.68	+9.1	+9.0	−0.09
4. Control	+0.003	∼0	∼0	+0.002
5. LC (crop albedo = 0.2)	−0.17	−4.9	−4.9	−0.28

3.2.2 Further Sensitivity Experiments

3.2.2.1 Dataset and Experiment Descriptions

Two historical land cover datasets are used in this section. The first is that of Ramankutty and Foley (1999, hereafter RF99), which was also used in the preliminary experiments described above. Implementation of this dataset into a global climate model is relatively straight forward, as surface parameters can be simply specified for the portion of each gridcell occupied by cropland. The second dataset used is that of Klein Goldewijk (2001, hereafter the HYDE dataset). This dataset includes both historical croplands and pasture on a 0.5° grid, with a single vegetation type given for each gridcell.

The experiments described in Section 3.2.1 provide a baseline to the experiments described here. In this section, I introduce two modifications to the land surface model. The first is a snow masking scheme that allows for the albedo of partially snow-covered land to vary according to the vegetation type. In the implementation of this scheme, the albedo value for snow was set to a fixed value of 0.45, and the surface albedo was allowed to scale linearly from its snow-free value to this constant upper limit for a completely snow-covered gridcell. The second is a parameterisation of surface resistance, which allowed for a more accurate representation of the evapotranspiration pathway and the effects on surface fluxes of moisture resulting from changing vegetation types. These modifications are described in Section 2.1.4.

Equilibrium runs are presented here using four different model/dataset configurations. First, the RF99 dataset was used, including the variable snow masking scheme, but omitting the use of surface resistance for all vegetation types (RF:SM). The second experiment used the same model configuration, but replaced the RF99 dataset with the HYDE dataset (HYDE:SM). Third, the RF99 dataset was used with both the snow masking scheme and the surface resistance parameterisation (RF:SM+SR).

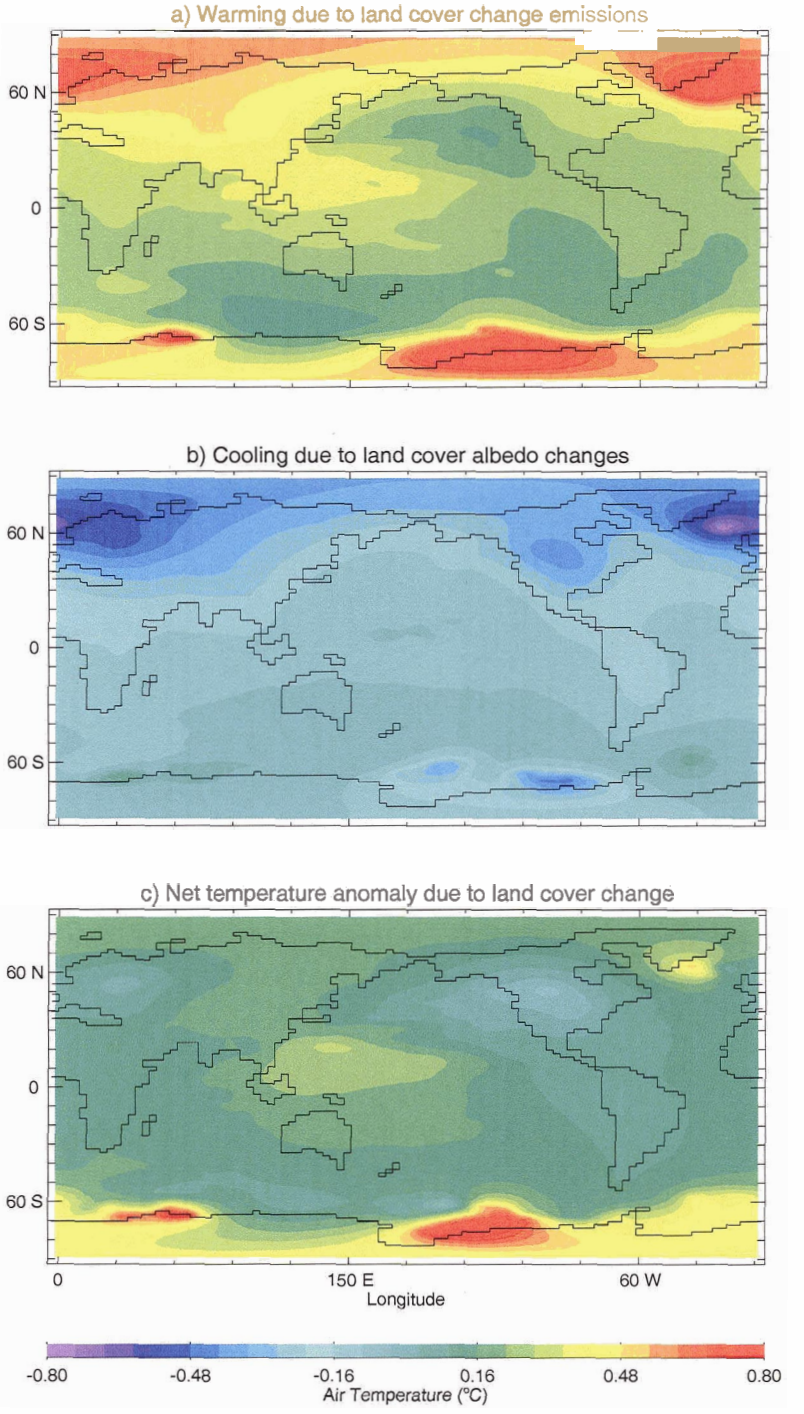

Figure 3.14: Regional temperature anomalies due to: a) land cover change emissions (biogeochemical effect), b) land cover changes to surface albedo (biogeophysical effect) and c) the net result of both the biogeochemical and biogeophysical effects of land cover change.

Table 3.3: **Equilibrium changes in globally averaged temperature, precipitation, surface albedo and downward shortwave radiation between the "present-day" and year 1700 equilibria.**

Experiment	**T**(°C)	**P**(mm/yr)	**Albedo**	**↓SW**(W/m^2)
RF:SM	−0.13	−3.1	+0.0016	−0.199
HYDE:SM	−0.19	−7.6	+0.0023	−0.275
RF:SM+SR	−0.14	−0.8	+0.0016	−0.198
RF:Alb	−0.13	−2.6	+0.0016	−0.198
RF:Alb-	−0.06	−1.8	+0.0008	−0.075
RF:Alb+	−0.22	−3.3	+0.0023	−0.325
RF:Prelim	−0.10	−3.3	+0.0010	−0.158

All experiment results show a global cooling and a decrease in precipitation. These changes are forced primarily by increases in surface albedo which result in a negative radiative forcing, as shown by decreases in net downward shortwave radiation at the surface. Globally averaged temperature changes range from −0.06 °C to −0.22 °C, depending on the model configurations and parameters used. Including pasture in addition to croplands increased global cooling by −0.06 °C (HYDE:SM) compared to croplands alone (RF:SM). Including a parameterisation of surface resistance (RF:SM+SR) has very little effect on global temperature, but precipitation changes are much smaller compared to when surface resistance changes are ignored (RF:SM). This can be explained by the assigned r_s value for croplands, which is smaller than all other r_s values. In this scenario, crops are assumed to transpire more than other vegetation types (due to the effects of irrigation), resulting in more precipitation over areas of land cover change that counteracts the reduced precipitation affected by global cooling and roughness length changes.

Temperature changes on the model grid are shown in Figure 3.10. Regional cooling resulting from land cover change ranges from 0 to −0.5 °C , reaching a maximum where large land cover changes (shown in Figure 3.2) overlap with areas of seasonal snow cover. This is most clearly seen in Northern Europe and Asia. Also evident

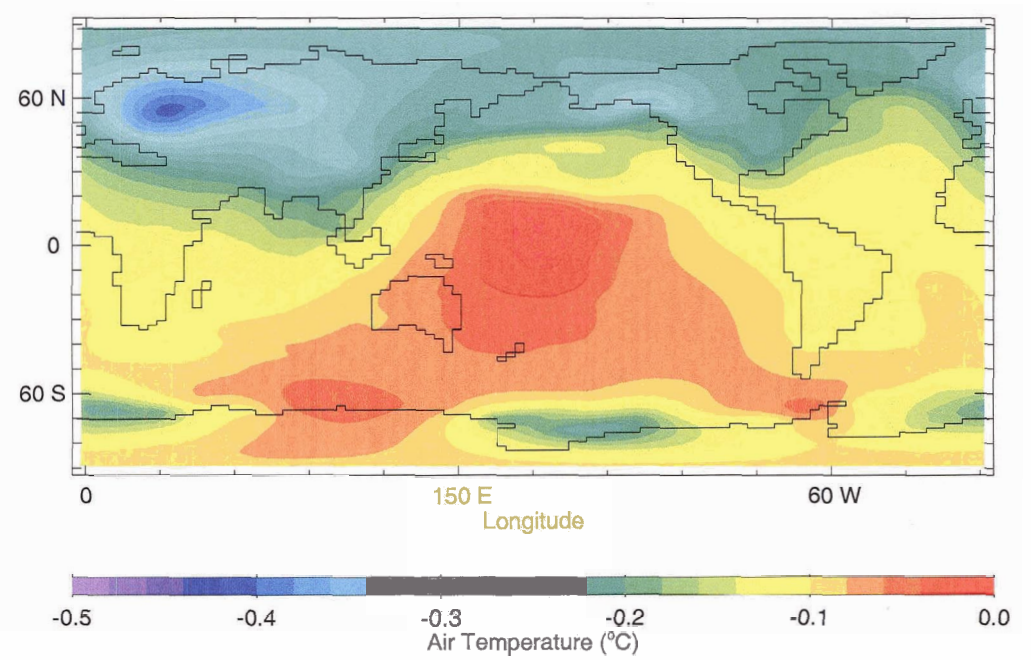

Figure 3.10: **Annual mean surface air temperature change on the model grid from year 1700 to 1992 for the equilibrium experiment RF:SM.**

in Figure 3.10 are regions where snow and sea-ice albedo feedbacks amplify local cooling, as seen off the coast of Antarctica and to some extent over Northwest North America and in the North Atlantic. Overall, the majority of the cooling occurs over continental regions in the Northern hemisphere. The shortwave radiative forcing that generates this spatial pattern of cooling can be seen in Figure 3.11. Whereas in the experiments described in Section 3.2.1, the change in downward shortwave radiation at the surface reached a maximum over Southeast Asia (see Figure 3.8), in Figure 3.11, the maximum shortwave forcing occurs in Eastern Europe. This different pattern of shortwave forcing results primarily from the inclusion of a variable snow-masking scheme which was excluded from the preliminary experiments. In addition, prescribing a fixed upper limit to the snow albedo results in a smoother surface albedo distribution for a snow-covered surface, as the maximum snow albedo value is now independent of the underlying surface vegetation type.

As in Section 3.2.1, the model is found to be very sensitive to specified surface

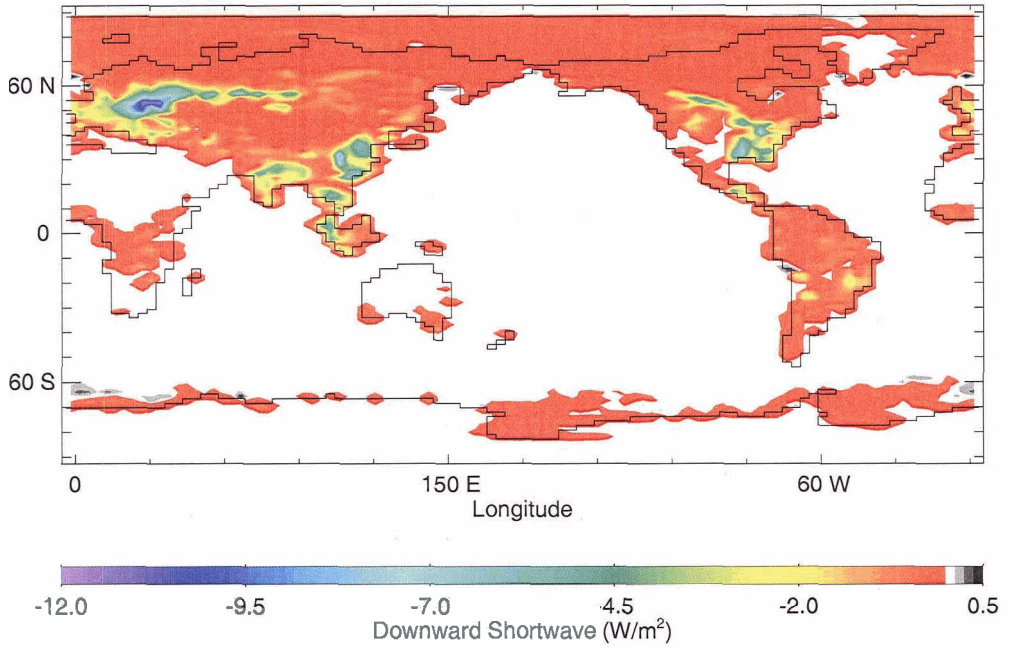

Figure 3.11: **Downward shortwave radiation change on the model grid from year 1700 to 1992 for the equilibrium experiment RF:SM.**

albedo values. If cropland albedos are increased to 0.20 from the default value of 0.17, the global cooling is increased from −0.13 °C (RF:ALB) to −0.22 °C (RF:ALB+). If cropland albedos are decreased to 0.15, the global cooling is decreased to −0.06 °C (RF:ALB-). It is likely that differences in how surface albedo is affected by land cover change in different models explains in large part the differences that are seen in model simulations of land cover change, a contention that is supported by the analysis of Myhre and Myhre (2003). There is also significant variability, however, in estimates of historical land cover change, and the interpretation of these data can account for discrepancy in model results. Bauer et al. (2003), for example, simulated a cooling over the past three centuries on the order of −0.3 °C, which is substantially higher than that found by our model, even accounting for reasonable surface albedo variation. Though Bauer et al. (2003) also used the RF99 dataset, they interpreted cropland areas as deforested areas. In the simulations presented here, there are fewer deforested areas than were used by Bauer et al. (2003); in many instances, cropland

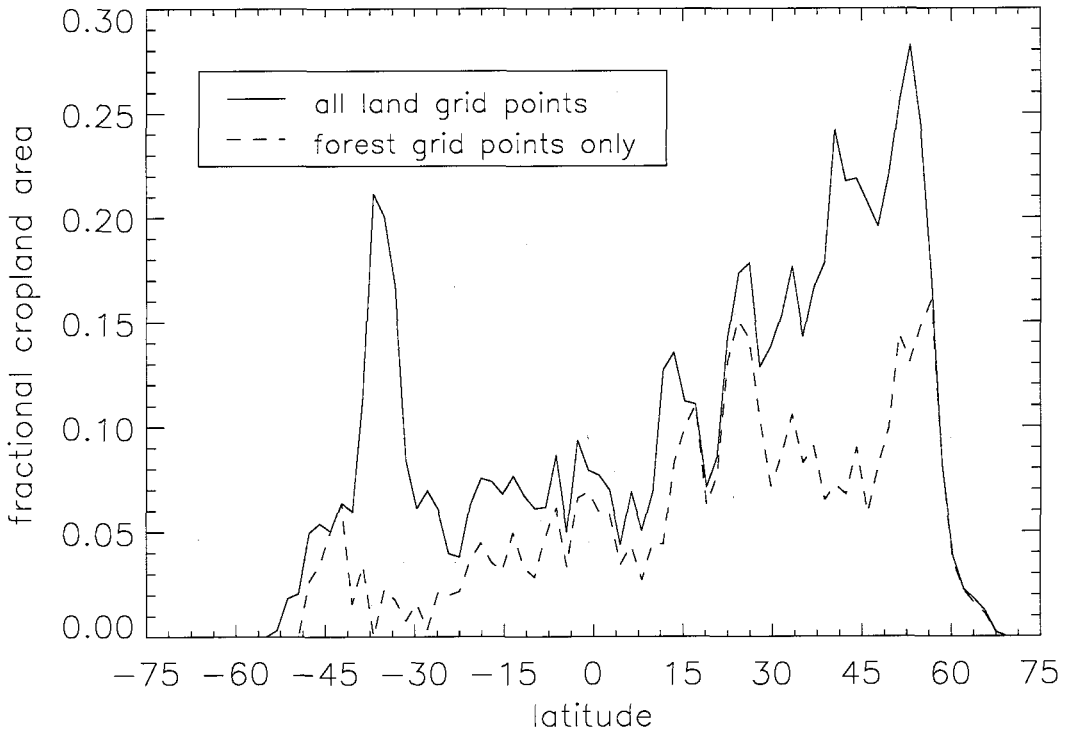

Figure 3.12: **Fractional cropland area by latitude, averaged over all land points (solid line) and over only those land points that are specified as forest vegetation types (dashed line). This comparison illustrates the difference between "deforested areas" and actual cropland area.**

was applied onto gridcells that in the "natural" vegetation fields were already designated as grassland or savanna, resulting in no change in local surface albedo. This can be seen in Figure 3.12; when averaged across forest-only gridcells in the UVic model, the fractional cropland area is substantially less than when averaged across all land points. It is likely this this difference in the model application of the RF99 croplands data explains the difference between the results reported here and those of Bauer et al. (2003).

It is worth noting that excluding roughness length as a variable model parameter has very little effect on global temperature, although there are small differences seen in global precipitation changes (RF:Alb compared to RF:SM). The radiative forc-

ing resulting from land cover change for all runs ranges from -0.075 (RF:Alb-) to -0.325 W/m^2 (RF:ALB+). This is well within the range of radiative forcing estimates provided in the literature (Hansen et al. 1998, Betts 2001, Myhre and Myhre 2003).

3.3 Biogeochemical and Net Effects of Historical Land Cover Change

In all cases presented thus far, the UVic ESCM has demonstrated a radiative cooling that results from surface albedo changes associated with historical land cover change. In this section I address the role that land cover changes have played in the global carbon cycle. Carbon emissions resulting from historical land cover change are well documented and are estimated to represent approximately a quarter of all anthropogenic carbon emissions for recent decades (Bolin et al. 2000, Houghton 2003a). This contribution to greenhouse gas forcing indicates that a significant portion of recent climate warming could be attributed to historical land cover change.

There have been some recent attempts to quantify the relative contribution of the biogeophysical effects (those associated with physical changes to the land surface) and biogeochemical effects (those resulting from emissions of greenhouse gases) of land cover change on global climate (Betts 2000, Claussen et al. 2001). These studies used hypothetical scenarios of reforestation (Betts 2000) or of deforestation and afforestation (Claussen et al. 2001), and found substantial regional variation in the magnitude and sign of the effect of land cover change on climate when both biogeophysical and biogeochemical processes are considered.

In this section, I assess the net effect of historical land cover change on global and regional climate by comparing the magnitude of the albedo-induced cooling reported in previous sections, with the contribution of land cover change emissions of carbon dioxide to 20^{th} century climate warming. The model experiments presented here

used the UVic ESCM dynamic vegetation and global carbon cycle model described in Sections 2.2 and 2.3. This version of the model computes atmospheric carbon dioxide prognostically as a function of anthropogenic emissions, as well as terrestrial and oceanic carbon fluxes and sinks. Results from this model are explored more extensively in Chapter 5.

3.3.1 Experimental Description

In this section, I present two transient climate simulations which were designed to identify the biogeochemical effect of historical land cover change. The first of these transient runs (FF Emissions) began from a control integration in which atmospheric carbon dioxide was fixed at 280 ppm and vegetation was allowed to equilibrate in the absence of land cover change. Fossil fuel emissions from Marland et al. (2002) were then specified from 1850 to present, and atmospheric CO_2 was allowed to respond freely to this forcing. The second transient run (FF+LCC Emissions) began from a control integration where atmospheric carbon dioxide was fixed at 280 ppm and vegetation was allowed to equilibrate under the constraint of imposed present-day cropland distributions. Emissions from both fossil fuels and land cover change (Houghton 2003a) were then specified from 1850 to present. For comparison, a third transient run is shown that was forced solely by the biogeophysical effects of land cover change. This specific run was generated using the same version of the UVic ESCM used in the "FF Emissions" and "FF+LCC Emissions" transient runs, though in this case, the carbon cycle component is not required, as atmospheric CO_2 is held fixed at pre-industrial levels. Transient land cover change runs are presented and discussed in more detail in Chapter 4.

3.3.2 Results and Discussion

Results from the above transient runs are shown in Figure 3.13. As can be seen in Figure 3.13a, specifying only fossil fuel emissions results in a substantial underestimation of present-day atmospheric carbon dioxide (327 ppm). Including land cover change emissions increases present-day atmospheric carbon dioxide to 353 ppm, a value that is much closer to the observed CO_2 concentration of 365 ppm. Historical land cover change emissions from 1850 to 2000 total 156 GtC, compared to 275 GtC from fossil fuels. Despite a slight underestimate of present-day CO_2 in the model, it is clear that land cover change emissions are necessary to accurately model historical atmospheric carbon dioxide concentrations.

What is also apparent from Figure 3.13b is that when land cover change emissions are included, the climate warming between 1850 and 2000 is increased by 0.3 °C compared to the case when only fossil fuel emissions are included. This global temperature change of 0.3 °C can be interpreted as the biogeochemical effect of historical land cover change, resulting from increased emissions of carbon dioxide. This 0.3 °C increase can be compared to the biogeophysical effect of historical land cover change, reported to range from −0.06 °C to −0.22 °C from the year 1700 to 2000 in Section 3.2.2.2, and shown as a transient run in Figure 3.13b from 1850 to 2000 (−0.16 °C cooling: see Chapter 4 for further discussion of the transient effect of land cover change). Considering the entire range of values found for the biogeophysical cooling, I conclude that the biogeochemical warming effect of historical land cover change emissions on globally averaged surface air temperature has exceeded the cooling effect of biogeophysical processes.

The climate response to these two competing effects of historical land cover change is also notable on a regional scale. In the carbon cycle model, carbon dioxide emissions are assumed to be instantaneously well mixed in the atmosphere, and as such,

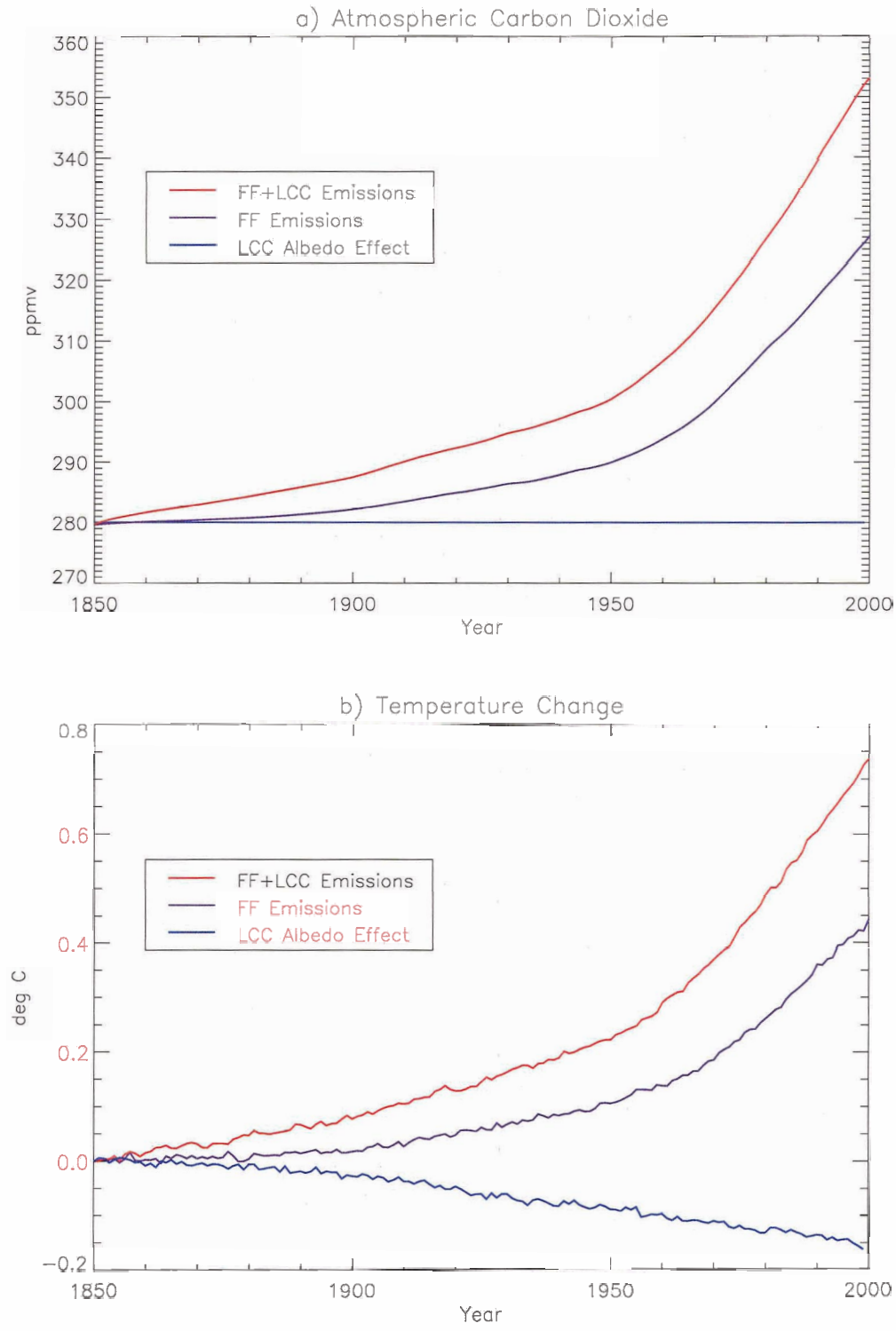

Figure 3.13: **Atmospheric carbon dioxide (a) and temperature change (b) from 1850 to 2000 resulting from transient runs forced by: fossil fuel emissions only (purple line) fossil fuel and land cover change emissions (red line) and land cover biogeophysical changes only (blue line).**

local warming does not represent local sources of carbon dioxide emissions. Nevertheless, there is a distinct regional pattern to both the warming associated with greenhouse gas emissions (Figure 3.14a) and the cooling generated by surface albedo changes (Figure 3.14b). The regional patterns of warming/cooling shown here can be attributed largely to amplification by local feedbacks, such as surface albedo changes that result from sea-ice dynamics in the North Atlantic and Southern oceans. In the case of Figure 3.14b, the cooling pattern does also reflect the spatial distribution of land cover changes.

Assuming a linear additivity of climate responses (I demonstrate that this is a reasonable assumption in Chapter 4), Figures 3.14a and 3.14b can be combined to determine the net effect of historical land cover change. Figure 3.14c thus represents the regional distribution of the net warming or cooling that results from both the biogeophysical and biogeochemical effects of historical land cover change. The net effect of land cover change reveals a distinct cooling over North America and very close to zero net change over Western Eurasia, with a warming over the Pacific Ocean, at high Northern latitudes and in the Southern hemisphere. The globally averaged net effect of land cover change under this comparison results in a warming of 0.15 °C.

3.4 Conclusions

The simulations presented in this chapter demonstrate that historical land cover change has had a non-negligible radiative effect on global climate over the past three centuries. All model runs in the preliminary experiments showed a cooling associated with land cover change, both in global averages, and as amplified locally by positive feedbacks. In the preliminary equilibrium runs, global cooling was in the range of -0.10°C to -0.22°C, depending on which vegetation dataset was used to represent present-day vegetation. In the transient case, the cooling was in the range of -0.09°C

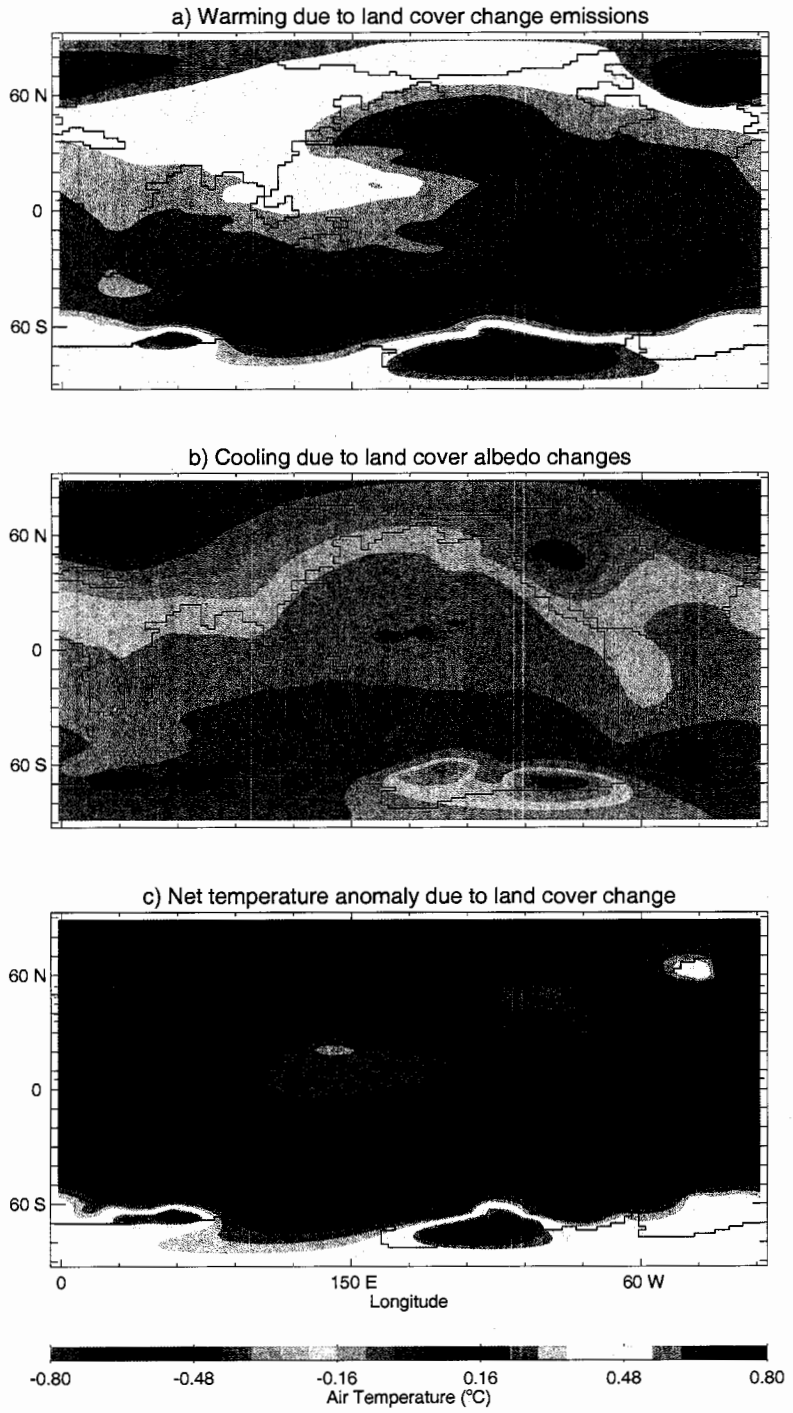

Figure 3.14: Regional temperature anomalies due to: a) land cover change emissions (biogeochemical effect), b) land cover changes to surface albedo (biogeophysical effect) and c) the net result of both the biogeochemical and biogeophysical effects of land cover change.

to −0.17°C, depending on the specified albedo value for cropland. From this analysis, it is clear that uncertainties in surface albedo values can have a large impact on the magnitude of the modelled land cover effect. It is also evident from comparing the land cover only transient run (−0.09°C cooling) with equilibrium runs (2) and (3) (−0.10°C cooling) that the effect of land cover change does not carry with it a large oceanic cooling commitment. This is in contrast to the effect of greenhouse gas forcing where the large thermal memory of the ocean has resulted in differences as large as 0.61°C in the UVic model between transient and equilibrium simulations of the present-day climate (Weaver et al. 2001).

In the follow-up sensitivity analysis using different land cover change datasets and varying model configurations and parameters, I found that the primary biogeophysical effect of historical land cover change has been to increase local surface albedo. While other parameters may be important to surface and regional processes, only albedo results in a global temperature effect. In these experiments, land cover change resulted in a global cooling of between −0.06 °C to −0.22 °C for the range of equilibrium comparisons performed here. I found that the cooling that results from land cover change is highly sensitive in our model (and I would expect this to hold for other models as well) to the specified surface albedo for croplands, or other human-modified land cover types. The entire range of results reported in this section can be reproduced simply by varying the specified cropland albedo value, with other model parameters proving to be of secondary importance. This last result helps to explain some of the variation seen in other simulations of the climatic effects historical land cover change (Bertrand et al. 2002, Bauer et al. 2003); remaining discrepancies between the results presented here and those of Bauer et al. (2003) are likely due to differences in the interpretation of the croplands dataset and resulting differences in the forcing applied to the climate model.

In the final section of this chapter, I addressed the question of the net effect

of historical land cover change, including both biogeochemical and biogeophysical processes. I found that including land cover change emissions in a transient climate simulation of the past 150 years amplifies greenhouse warming by 0.3 °C on the global average. This increase exceeds the biogeophysical cooling found over the same period (−0.16 °C). I therefore conclude that the net effect of land cover change has been to increase global temperatures over the last 150 years by an amount on the order of 0.15 °C. I further note that in some geographical regions, particularly over Northern hemisphere continents, the cooling influence of land cover change has dominated, while over most of the rest of the globe, the net effect has been warming. As this is the first time that the effect of observed historical land cover change has been studied using a global climate-carbon cycle model, these results shed new light on the competing effects of land cover change on the climate system.

These conclusions point to the important role that human land cover changes have played in observed climate change. It is clear that historical land cover change has had substantial and regionally varied effects on global temperatures, and that when included in transient simulations of recent climate change, land cover changes help to improve model simulations of the historical temperature record. Including the effect of land cover change emissions is of particular importance, as their contribution to recent climate warming has been notable. In future work, when considering the implications of carbon cycle feedbacks to climate, it will be critical to include the combined effects of land cover change on surface parameters, global carbon sinks and carbon dioxide emissions.

Chapter 4

Natural and Anthropogenic Climate Change

4.1 Introduction

Changes in global climate in the latter half of the 20^{th} century represent a distinct anomaly in the historical climate record. The global temperature increase of 0.6 $\pm$0.2 °C since 1900 has occurred at a rate unprecedented in the last 1000 years (Houghton et al. 2001). The current global temperature is unmatched in the Holocene (the last ten thousand years), and indeed has likely not occurred since the peak of the last interglacial, some 126,000 years ago (Petit et al. 1999).

In the last several decades, the field of climate science has been motivated largely by the challenge of understanding the changes that we are currently observing in the climate system. In the last decade, the global scientific community, as represented by the Intergovernmental Panel on Climate Change (IPCC), has sent a clear message that human activities are in large part responsible for the climate changes we are currently experiencing. Key among the identified causes of this global warming are elevated levels of greenhouse gases: levels that are unprecedented in the last 420,000 years (Houghton et al. 2001, Petit et al. 1999).

Numerous studies have identified processes that can act to force changes in global climate. Anthropogenic influences, of which greenhouse gases are known to be the most important, also include emissions of sulphate aerosols and human land cover change, as well as smaller forcings such as stratospheric ozone depletion, black and

organic carbon aerosols and jet contrails. Natural climate forcing processes include solar variability due to sunspot and other solar cycles, long-term changes in solar orbital parameters, and intermittent volcanic eruptions (Hansen et al. 1998, Houghton et al. 2001).

In this chapter, I present a suite of transient model simulations from 1700 to 2000 using the UVic ESCM forced by a series of natural and anthropogenic climate influences. These simulations place the biogeophysical effect of land cover change reported in Chapter 3, in the context of other climate changes that have been observed over the past 300 years. This is followed by a brief discussion of the extent to which the simulated results can be detected in observations of temperature change. In the final section of this chapter, I introduce simulations using the dynamic vegetation model described in section 2.2 coupled to the UVic ESCM. This model was run using the same set of natural and anthropogenic climate forcings, to explore the role of dynamic vegetation changes as a feedback and potential amplifier of externally forced climate change.

4.2 Natural and Anthropogenic Climate Change

In this section, the transient effect of land cover change is compared to other natural and anthropogenic forcings. As reported in Chapter 3, the transient effect of land cover change from 1700 to present is very similar to the equilibrium effect, a sign that there is very little oceanic cooling commitment associated with land cover change. For all transient runs reported in the following section, the model configuration used in experiment RF:SM+SR was chosen: the RF99 dataset was used (only croplands are accounted for) and all variable model parameter options were included.

The natural forcings considered are volcanic aerosols (VOLC), solar insolation variability (INS) and orbital changes (ORB). In addition to land cover change (LCC),

the anthropogenic forcings of greenhouse gases (CO_2 and other non-CO_2 greenhouse gases) (GG) and sulphate aerosols (SUL) were included. The datasets and methods used for each of these forcings are outlined in Section 2.1.5. The transient effect of each forcing is considered individually (GG, SUL, LCC, VOLC, INS, ORB), and then in combinations of anthropogenic forcings only (ANTH), natural forcings only (NAT) and all model forcings (ALL). A control equilibrium was spun up for 2000 years using year 1700 conditions (solar constant, orbital parameters, land cover), with greenhouse gases set to 280 ppmv and volcanic and sulphate aerosols set to zero. Transient scenarios for each individual forcing and combination were started from this control equilibrium and run from the year 1700 to the year 2000.

4.2.1 Transient Model Results

Figure 4.1 shows the results of transient runs driven by each individual model forcing. Greenhouse gas forcing results in a warming of 1.3 °C by the year 2000 compared to the control equilibrium. As described in Section 2.1.5, greenhouse gas increases for this run were prescribed from observed increases — this results in a much more realistic simulation of the temperature response to greenhouse gas forcing than that shown in Figure 3.7, where the historical CO_2 increase was approximated by an exponential function. Sulphate aerosols were assumed to be zero until 1850, after which they result in a cooling of −0.5 °C. Land cover change affects a cooling of −0.13 °C , very close to the equilibrium cooling of −0.14 °C found in the RF:SM+SR equilibrium experiment and consistent with the notion that there is very little oceanic cooling commitment associated with land cover change.

Natural forcings can also be seen to have significant effects. The effect of volcanic aerosols is notable but periodic, with large cooling episodes associated with major volcanic eruptions. Mt. Pinatubo (1992), El Chichon (1982), Agung (1963) and Krakatau (1883) can all be seen clearly. The largest volcanic cooling is associated

with Tambora (1815), said to have elicited the "year without a summer", and a global cooling in the range of 1 °C (Robock 1994, 2000). A slight long-term cooling trend can be seen in the VOLC model run, though it is possible that this is simply a result of starting from a model spin-up that does not include volcanic aerosols. Solar insolation changes result in a significant warming over the 300 year model run, partly due to the fact that the year 1700 chosen for the equilibrium spin-up corresponded to a local insolation minimum in the Lean et al. (1995) dataset. The warming in the early part of the model run is probably artificially amplified as a result of this, although there is still an additional warming in the range of 0.2 °C over the period from 1800 to 2000. Solar orbital changes have virtually no effect on globally averaged temperature, and thus demonstrate the low model variability and the model's stability when subjected to negligibly small external forcings.

It should also be noted that the linear sum of the individually forced climate responses (shown in Figure 4.1 as the thin grey line) is almost indistinguishable from the model response to all model forcings together (ALL, thick black line). This demonstrates the linear additivity of climate model responses to individual forcings in the context of our model, a conclusion that has also been drawn from other modelling studies (see for example Ramaswamy and Chen 1997).

Combinations of forcings (ALL, NAT and ANTH) are shown for the period from 1850 to 2000 in Figure 4.2 and compared to historical temperature data from Folland et al. (2001). As can be seen by comparing the all-forcings model run (purple line) with the temperature data (grey line), the UVic ESCM does an excellent job of reproducing the historical temperature trend in the absence of atmospheric variability. The 20^{th} Century saw a warming of 0.8 °C in the all-forcings model run, consistent with the 0.6 $\pm$0.2 °C warming cited by Houghton et al. (2001), and clearly in alignment with the temperature data shown in Figure 4.2. The model produces a cooling in the 1960's associated with the Agung volcanic eruption, a cooling that is also seen in the

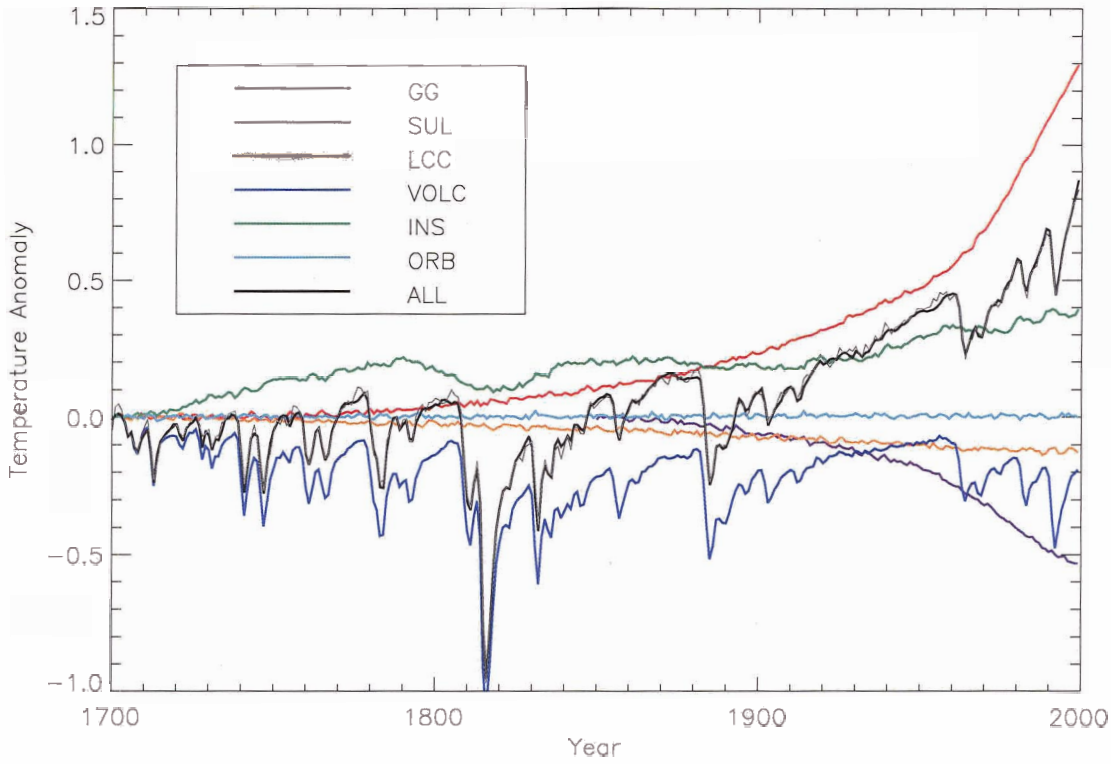

Figure 4.1: **Transient model runs from 1700 to 2000 under the six individual model forcings, and for all-forcings combined. Greenhouse gas (GG) forcing only is shown in red, sulphate aerosols (SUL) in purple, land cover change (LCC) in orange, volcanic aerosols (VOLC) in blue, solar insolation (INS) in green and solar orbital (ORB) in cyan. A transient run forced by all model forcings together (ALL) is shown by the thick black line. The thin grey line shows the linear sum of the six individual model forcings, for comparison with the all-forcings model run.**

historical temperature data. The warming in the early 1940's followed by a cooling trend in the latter portion of the decade and throughout the 1950's is not reproduced by the model, suggesting that this temperature variation is likely the result of internal climate variability (such as El Niño/La Niña) that is not captured in our model. The data also do not show the large volcanic cooling in the 1880's associated with the Krakatau eruption, but this model/data discrepancy is consistent with other model simulations of this period (see for example Stott et al. 2001). It is also possible that early temperature records do not capture the transient effects of volcanoes well, or that they may have been more heavily biased to Northern hemisphere temperatures, and thus not have accurately recorded the global effects of a large Southern hemisphere eruption. Alternately, it is possible that the optical depth changes inferred in the earlier portions of the volcanic records are not as good as more recent estimates.

Separation of model forcings into categories of natural forcings only (volcanic aerosols, solar insolation and orbital changes) and anthropogenic forcings only (greenhouse gases, sulphate aerosols and land cover change) reveal the source of temperature changes seen in the all-forcings model run. The natural forcings only run (blue line in Figure 4.2) shows a clear warming in the first half of the 20^{th} century as a result of a quiescence of volcanic activity and some increase in solar insolation. This is followed by a cooling trend in the latter half of the 20^{th} century, initiated and maintained by a series of large volcanic events. The anthropogenic forcings only run (red line in Figure 4.2) shows a gradual warming throughout the model run, but with a distinct acceleration of warming after 1960. These two model patterns combine in a linear fashion to generate the temperature trend seen in the all-forcings model run. Based on these results, I argue that the warming seen in the data in the early part of the century is a combination of greenhouse forcing and natural forcing, the cooling seen in the 1960's is a result of a resumption of volcanic activity, and the distinct warming in the latter half of the 20^{th} century can only be accounted for by greenhouse gas

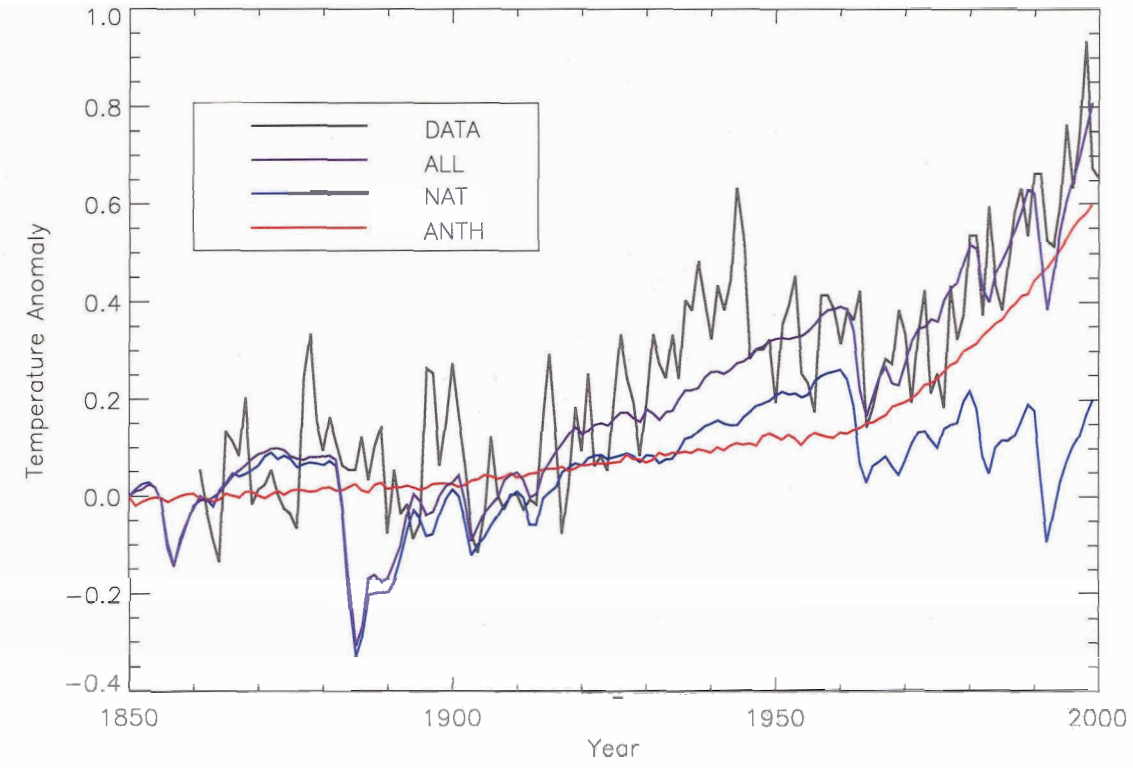

Figure 4.2: **All model forgings (ALL), natural (NAT) and anthropogenic (ANTH) combinations shown with global temperature data (DATA) for 1850 to 2000. DATA is shown in grey, ALL in purple, NAT in blue and ANTH in red. ALL and DATA are plotted such that their respective 1961 to 1990 averages are equal. NAT and ANTH are plotted so that they begin from the same point as ALL.**

forcing. These conclusions are consistent with those found by Stott et al. (2001).

Figure 4.3 shows Northern hemisphere mean temperatures from the all-forcings model run compared to the temperature reconstruction from Mann et al. (1999). While the strong volcanic signals seen in the model are not evident in the proxy data, the model results do fit within the error envelope of the proxy data prior to 1900, and track the Northern hemisphere temperature time series closely over the 20^{th} century.

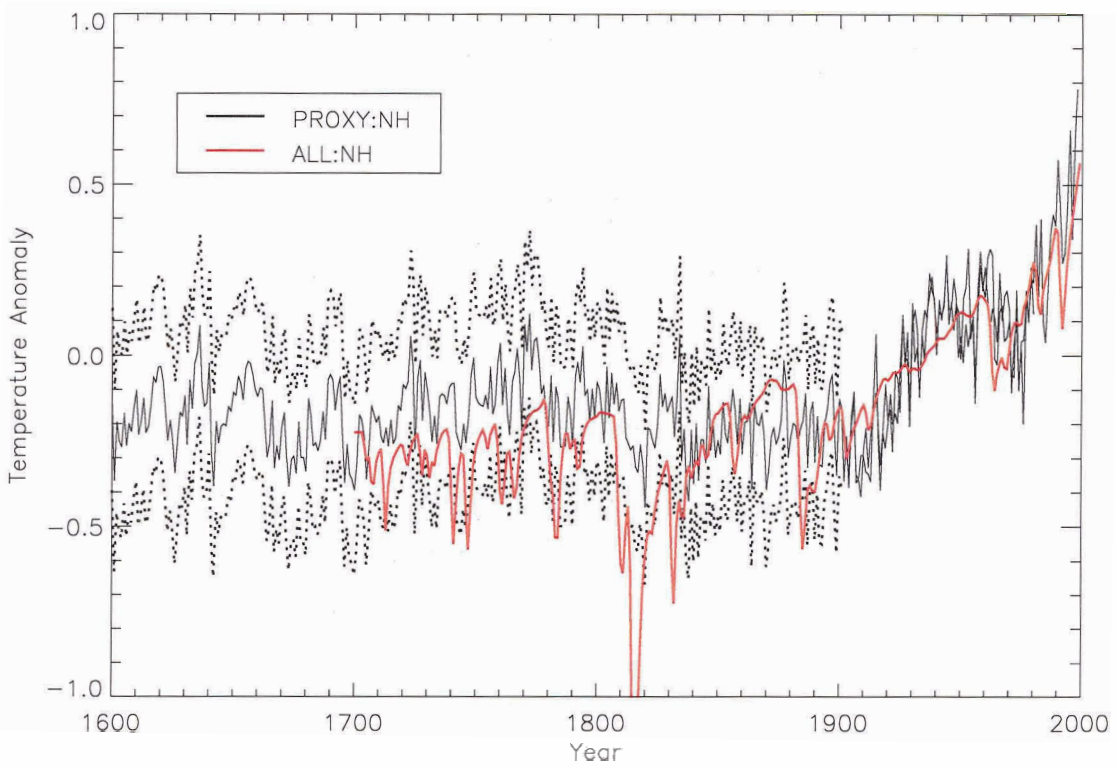

Figure 4.3: **All model forgings (ALL) compared to northern hemisphere temperature reconstruction (PROXY). Dotted lines indicate two standard deviations for the proxy data prior to 1900. Both proxy data and model results are plotted as anomalies against their respective 1902 to 1980 averages.**

4.2.2 Detection of Climate Change

Detection and attribution experiments represent an attempt to statistically detect trends seen in model output by comparing them to observations, and further to attribute the trends to external climate forcings. Recent detection and attribution studies have successfully attributed 20^{th} century temperature changes to greenhouse gas and sulphate aerosol forcing (Tett et al. 1999, Stott et al. 2001) as well as to changes in volcanic aerosols and solar irradiance (Jones et al. 2003). Hegerl et al. (2003) also applied detection and attribution methods to longer proxy records in an effort to detect volcanic, solar and greenhouse gas signals in hemispherically averaged temperature proxies. In this section we[1] apply the optimal fingerprint detection method (Tett et al. 1999) to UVic ESCM output of 20^{th} century temperature change to assess the detectability of biogeophysical changes forced by land cover change in comparison to all other model forcings.

Figure 4.4 shows the results of the detection and attribution experiment on model output from transient runs of land cover change and all other model forcings regressed against observations of the period from 1896 to 1996 (Jones 1993). Results are derived using an ordinary least squares regression of decadal mean T4 spherical harmonic temperatures (1896-1996) with a 10 EOF (empirical orthogonal function) truncation (Tett et al. 1999). Natural variability was estimated from the CGCM2 control simulation (Flato and Boer 2001). As can be seen on the horizontal axis of Figure 4.4, the combination of all model forcings is very well detected, with a regression coefficient very close to 1. The effect of land cover change carries a regression coefficient of about 0.6, consistent with the notion that the RF99 dataset does not capture all of the land cover changes that have occurred in the past century. However, the error bars are too large to make this forcing statistically detectable. We conclude that cooling due to land cover change in the 20^{th} century (about -0.05 °C) is too

[1]These results were produced and interpreted with the assistance of N. Gillett

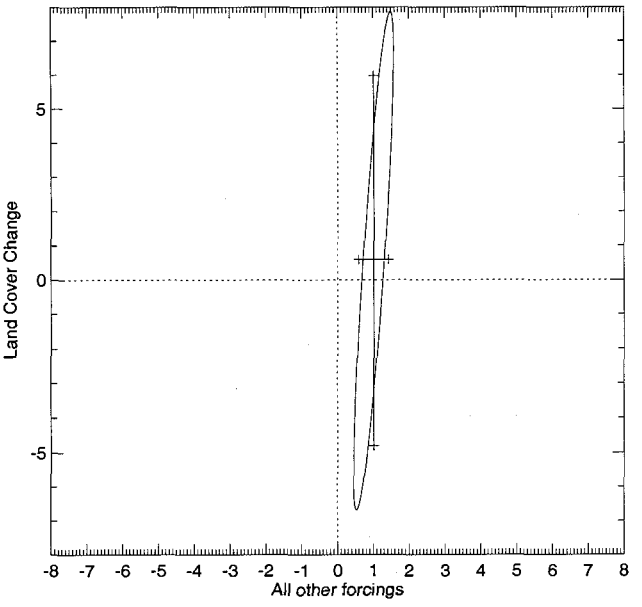

Figure 4.4: **Regression coefficients for land cover change and all other model forcings regressed against observations.**

small to be detected statistically in observed trends. This experiment was repeated using the Mann et al. (1999) Northern hemisphere temperature data for the period from 1700 to present. Although the error bars on the effect of land cover change were smaller, the signal was still not statistically detectable.

4.3 Dynamic Vegetation

In this section, I present transient runs from the UVic ESCM coupled to the modified MOSES land surface model and the dynamic terrestrial vegetation model TRIFFID (Section 2.2). Recent development of global dynamic vegetation models has allowed for the study of how changing vegetation distributions, as a function of climate, could feed back to climate change (Cramer et al. 2001). In this section, I explore the role of vegetation dynamics as a feedback within the climate system, in the context of anthropogenic climate change. As in the previous versions of the model, land cover change is prescribed from the RF99 dataset as a fractional area of cropland in each

gridcell. Now that vegetation is dynamic rather than prescribed, the prescribed land cover change allocates a portion of each gridcell where only grass plant functional types (C_3 or C_4 grasses) are allowed to grow. The remaining plant functional types (trees and shrubs) compete for space along with grass types in the unallocated portion of the gridcell.

Figure 4.5 shows the all-forcings model results for the 20^{th} century portion of the 300-year transient runs. Two new model runs are presented here: the first allows vegetation to respond dynamically to climate (ALL:DYN), and the second holds vegetation fixed at simulated pre-industrial distributions (ALL:CONST). These two runs are plotted in comparison with the previous all-forcings run (Section 4.2) without the dynamic vegetation model option (ALL), and the global temperature data (DATA). As can been seen by comparing ALL:CONST with ALL, when vegetation is held constant, this new model responds to the specified climate forcings in a similar fashion to the previous model version. When vegetation is allowed to change dynamically in response to climate changes however (ALL:DYN), there is a noticeable positive feedback to the climate system that results in an amplification of 20^{th} century climate warming by about 0.1 °C.

This same vegetation-climate feedback can be seen in the land cover change only transient runs shown in Figure 4.6. Including vegetation dynamics (LCC:DYN) increases the cooling signal from -0.14 °C (as in the case of the constant vegetation run: LCC:CONST) to -0.19 °C. The mechanism for this amplification can be seen in Figure 4.7, which shows the difference in simulated Northern hemisphere surface albedo between the LCC:DYN and LCC:CONST transient runs at the year 2000. Higher surface albedo values are seen in LCC:DYN throughout Northern Asia, and to a lesser extent in North America. This increase follows directly from changes in high-latitude vegetation cover, from forest vegetation types to grasses and shrubs, in response to climate cooling. The globally averaged surface albedo increase is $+0.0007$,

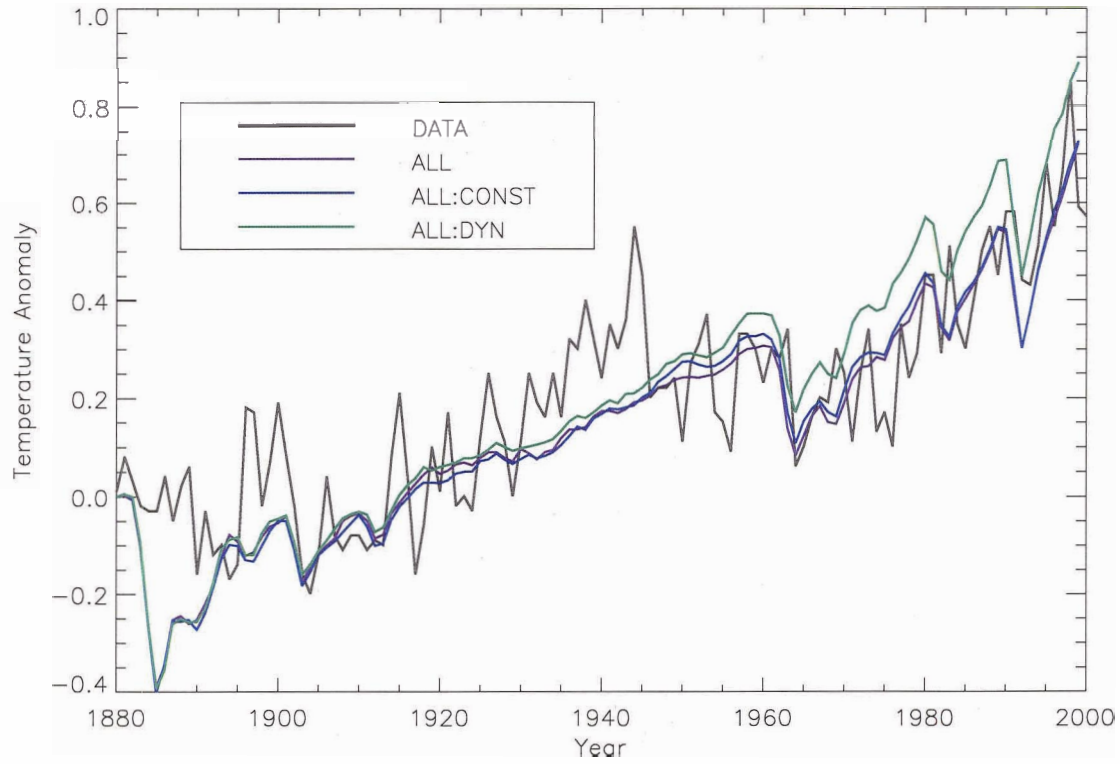

Figure 4.5: **All-forgings model transient run from 1880 to 2000 compared to data for: previous model version (ALL), model version including MOSES and TRIFFID but holding vegetation constant (ALL:CONST) and model including MOSES and TRIFFID and dynamic vegetation (ALL:DYN).**

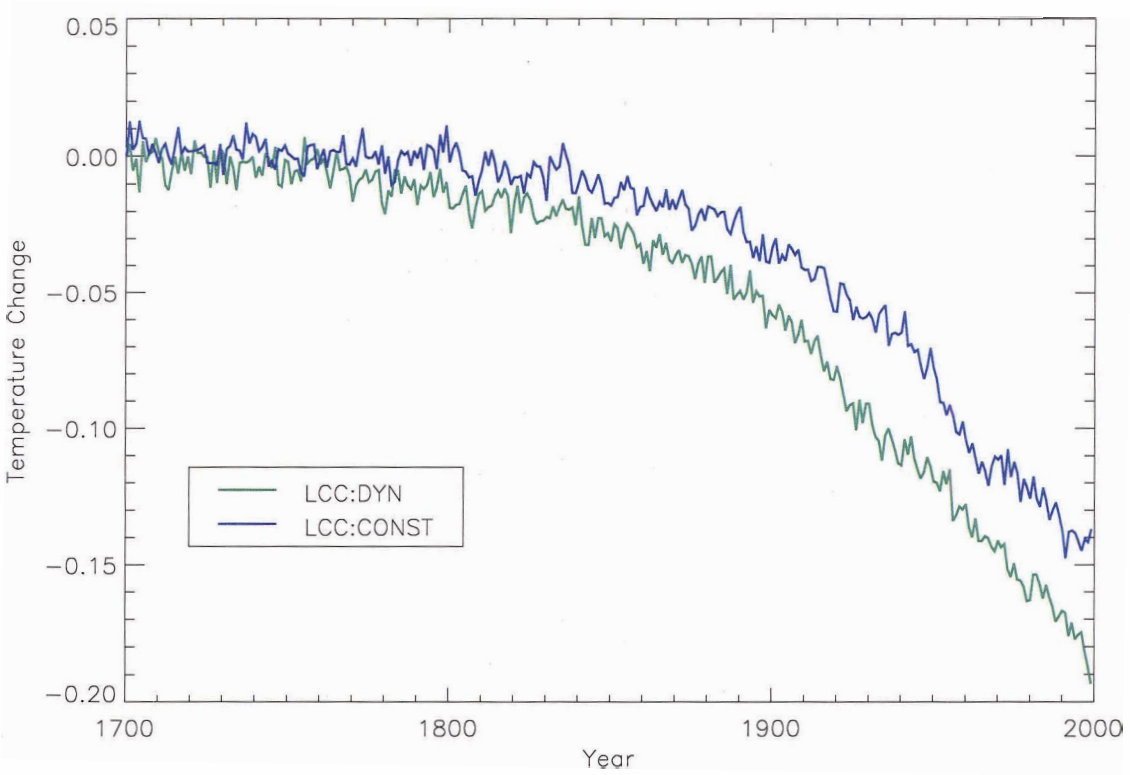

Figure 4.6: **Transient runs from 1700 to 2000 forced by land cover change alone for the model including MOSES and TRIFFID, with constant vegetation (LCC:CONST) compared to dynamic vegetation (LCC:DYN).**

which is sufficient to account for the amplification of cooling between the two runs (see Table 3.3 for comparison). In the case of climate warming (as in Figure 4.5) high latitude forests migrate northward, leading to a net decrease in surface albedo as forests replace grass and shrub plant types. This decreased surface albedo results in an enhanced climate warming. Thus in both the land cover change only and the all-forcings model runs, vegetation dynamics act as a positive feedback to the climate system, amplifying the effect of the specified forcing.

As stated in Section 4.2, in the case of prescribed vegetation, equilibrium and transient simulations of land cover change result in very similar global temperature changes, a sign that the oceanic cooling commitment associated with land cover change is negligible. This is not the case however when vegetation is allowed to

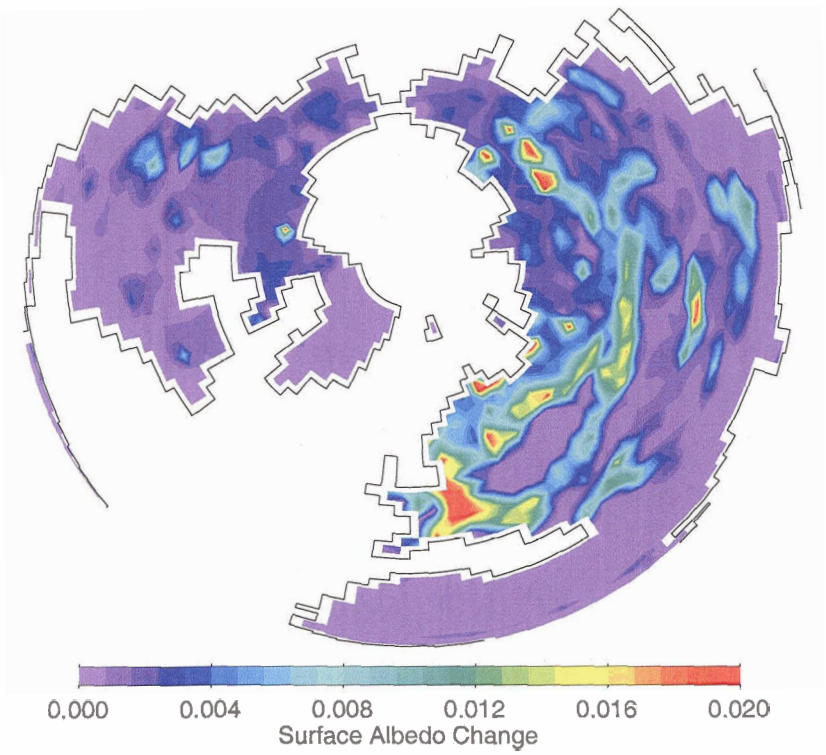

Figure 4.7: Northern hemisphere surface albedo change between LU:DYN and LU:CONST at present-day. Increases in surface albedo reflect changes in high-latitude vegetation cover from forest vegetation types to grasses and shrubs in response to climate cooling.

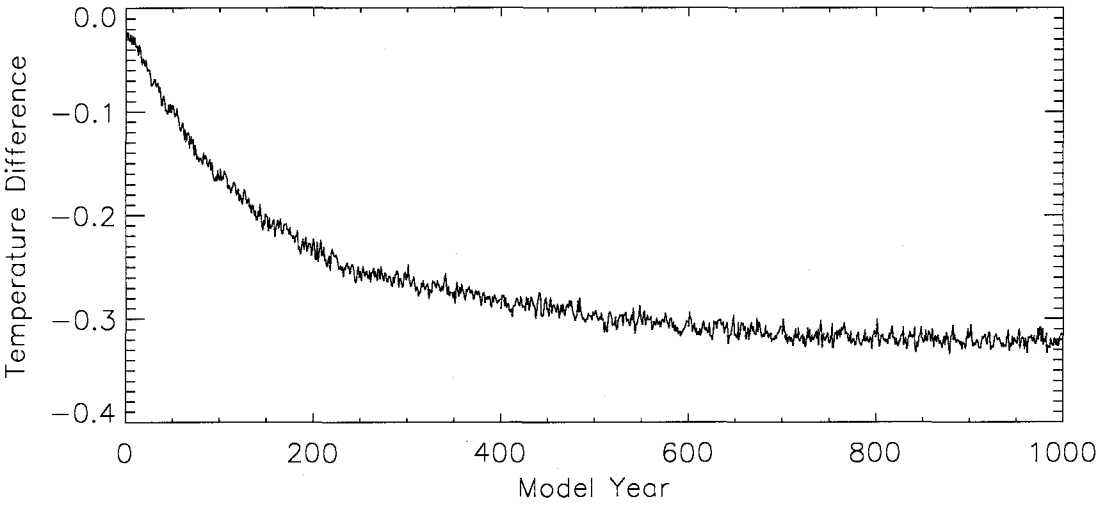

Figure 4.8: **Temperature difference between equilibrium simulations with present-day and year 1700 land cover over 1000 years of model integration.**

respond dynamically to changes in climate. Vegetation dynamics operate on decadal to centennial time scales, and as such introduce a new lag effect into the climate system that is not present when vegetation is prescribed or held constant.

Figure 4.8 shows the temperature difference over 1000 years of model integration between two equilibrium simulations of land cover change that include dynamic vegetation. The temperature difference between present-day and year 1700 simulations is seen to decrease rapidly, reaching -0.19 °C (the cooling reported for this model's transient simulation of land cover change) at around 150 years of model integration. This cooling continues however, as vegetation distributions adjust to the new climate regime, approaching the equilibrium difference of -0.32 °C only after several hundred years. From this comparison, it is clear that the positive feedback to climate from dynamic vegetation in this model is a slow process that requires at least 400 or 500 years to achieve its full effect.

4.4 Conclusions

In this chapter, I have presented results from transient climate simulations of the last 300 years. For the effect of land cover change, I chose an intermediate albedo value for croplands, resulting in a cooling of -0.13 °C from 1700 to present-day. When compared to other anthropogenic (greenhouse gases and sulphate aerosols) and natural (volcanic aerosols, solar insolation and orbital changes) climate influences, I found that the biogeophysical effect of land cover change is of secondary importance to other anthropogenic forcings, although it is of comparable magnitude to smaller forcings such as solar variability. On short timescales, volcanic forcing far exceeds that of land cover change, but both account for a similar amount of cooling over decadal to centennial length time scales. By comparing the effects of natural and anthropogenic climate influences, I found that the warming trend of the late 20^{th} century is well simulated by the combined effects of anthropogenic activities, whereas warming and cooling trends in the earlier portion of the temperature record are likely attributable to a combination of natural and anthropogenic climate change. I conclude from these transient runs that 20^{th} century climate change has been forced primarily by changes in greenhouse gases, but that other forcings and internal model feedbacks contribute to a realistic simulation of climate change over the past 300 years. These conclusions lend support to other published simulations of the effect of natural and anthropogenically forced climate changes (Crowley 2000, Stott et al. 2000, 2001, Bertrand et al. 2002, Bauer et al. 2003).

In Section 4.2.2, I found that the biogeophysical effect of land cover change is too small to be detectable in either 20^{th} century temperature data or hemispherically averaged proxy data. While including the biogeophysical effect of historical land cover change has the potential to improve simulations of recent climate change, the effect of this forcing is small compared to natural climate variability and other anthropogenic

climate changes. The issue of detection is complicated by the uncertainties associated with estimates of land cover change as well as its coupled biogeophysical and biogeochemical effects on climate. It is perhaps not surprising that the albedo-induced cooling effect alone is not readily detectable in 20^{th} century observations. As land cover changes have not previously been included in detection and attribution studies, this result suggests that it is unlikely that more complex models will be able to detect a significant effect.

When vegetation dynamics are included, as in Section 4.3, the results presented in previous sections are amplified by a positive feedback between vegetation dynamics and the climate system. When all model forcings are included, vegetation dynamics increase 20^{th} century warming by about 0.1 °C. In the case of simulations forced by land cover change only, vegetation dynamics increase the cooling signal from -0.14 °C to -0.19 °C between 1700 and present-day. In addition, the positive vegetation feedback introduces a significant lag effect into the climate model, resulting in a much larger equilibrium temperature difference (-0.32 °C) associated with land cover change than that found in the transient simulations (-0.19 °C).

Chapter 5

The Global Carbon Cycle

5.1 Introduction: Terrestrial Carbon Cycle Dynamics

The behaviour of the terrestrial carbon cycle under changing atmospheric carbon dioxide levels and climate remains a key area of uncertainty in our understanding of the global climate system. Atmospheric CO_2 has increased by about 90 ppmv in the last two centuries, but this increase represents less than half of the total anthropogenic release of carbon dioxide since the beginning of the industrial revolution, the remainder having been sequestered by the oceans and the land biosphere (Prentice et al. 2001). In order to understand this pattern of atmospheric accumulation, we must understand how terrestrial and oceanic carbon sinks absorb anthropogenic carbon, and the extent to which carbon sinks will persist under continued emissions of greenhouse gases.

Despite this imperative, estimates of terrestrial CO_2 uptake for the last several decades are very poorly constrained. Bolin et al. (2000), in the IPCC Special Report on Land Use, Land-Use Change and Forestry, indicated that terrestrial carbon uptake was in the range of 0.6 to 3.2 GtC/year for the 1980s, and 1.0 to 3.6 GtC/year for the 1990s. These numbers have recently been updated by House et al. (2003), who reported that terrestrial carbon uptake was in the range of 0.3 to 4.0 GtC/year and 1.6 to 4.8 GtC/year for the 1980s and 1990s respectively. The modifications reported in House et al. (2003) were based on improved estimates of ocean carbon

uptake from measured oxygen fluxes (Bopp et al. 2002, Plattner et al. 2002), as well as updated estimates of the net emissions of carbon from anthropogenic land-use change (Houghton 2003a). It is notable that despite extensive research over the past several years, the uncertainty range on estimates of terrestrial carbon uptake has not narrowed.

One of the primary challenges in the investigation of the terrestrial carbon cycle is the difficulty obtaining direct observational estimates of terrestrial carbon uptake. Forest inventory studies and measurements of carbon fluxes using the eddy-covariance method are useful for estimating changes in terrestrial carbon stores for individual forest plots, but there are considerable challenges both in the accuracy of these methods and in their ability to be extrapolated to continental or global scales (Adams and Piovesan 2002, Houghton 2003b). Analysis of atmospheric O_2 trends (Bopp et al. 2002, Plattner et al. 2002), inverse modelling of atmospheric carbon fluxes using atmospheric transport models (Bousquet et al. 2000, Gurney et al. 2002), and analysis of ice-core CO_2 records (Joos et al. 1999, Trudinger et al. 2002) are useful in partitioning anthropogenic carbon uptake between oceanic and terrestrial sinks. However, these methods can only shed light on the net terrestrial flux — emissions of carbon from land-use change must still be accounted for to obtain an estimate of the actual terrestrial carbon uptake. The values for terrestrial uptake reported by both Bolin et al. (2000) and House et al. (2003), while generally consistent with observational results, were nevertheless obtained by calculating a residual terrestrial sink based on the difference between estimates of anthropogenic carbon emissions from fossil fuels and land-use change, measured increases in atmospheric carbon dioxide, and model and observationally-based estimates of ocean uptake. As all of these components of the global carbon balance have considerable uncertainty associated with them, it is not surprising that the uncertainty on estimates of the residual terrestrial carbon sink is also large.

Another area of uncertainty is the mechanism behind the observed terrestrial carbon sink. It is thought that terrestrial carbon uptake is due to some combination of several processes: fertilization of plant growth by increased atmospheric CO_2 and by deposition of anthropogenic nitrogen; changes in climatic constraints on vegetation growth; and regrowth of forests in previously harvested areas (Schimel et al. 2001, Malhi et al. 2002, Adams and Piovesan 2002, Houghton 2003b, Nemani et al. 2003). There is considerable debate about the relative magnitude of these effects, and and it is not clear to what extent the mechanisms behind the terrestrial carbon sink will persist into the future. Comparisons of process-based terrestrial ecosystem models have generally found the terrestrial carbon sink to be consistent with the effect of CO_2 fertilization on plant growth (Cramer et al. 2001, McGuire et al. 2001), though there is conflicting experimental evidence to suggest that increases in plant photosynthesis may be limited by nutrient availability (Oren et al. 2001) or by other constraints on plant growth (see reviews by Adams and Piovesan 2002, Malhi et al. 2002, Karnosky 2003). However, these conclusions are based on short term exposure of plants to fixed elevated CO_2 in a controlled experimental setup. The response of diverse terrestrial ecosystems to continually increasing atmospheric CO_2 levels over decades to centuries is very difficult to assess experimentally, and remains an open question.

There is even less information available on the potential for feedbacks between climate and the carbon cycle. It is quite possible that changes in temperature and precipitation could affect the ability of the terrestrial biosphere to take up anthropogenic carbon over the coming century. As climatically-induced changes in terrestrial carbon fluxes would have a direct effect on atmospheric accumulation of carbon dioxide, this would constitute an important and as yet poorly quantified climate feedback. In particular, there is evidence that increased soil temperatures may increase carbon decomposition in the soil through increased heterotrophic respiration by soil microbes. Increased heterotrophic respiration would create a positive feedback to

climate, resulting from an increased flux of carbon from the soil to the atmosphere and a correspondingly reduced terrestrial carbon sink (Cox et al. 2000, Cramer et al. 2001, Friedlingstein et al. 2001, Dufresne et al. 2002, Melillo et al. 2002).

Global climate models have only recently incorporated the functionality necessary to study the carbon cycle response to climate change through the inclusion of interactive carbon cycle models. This has allowed for a fully coupled investigation of the sustainability of terrestrial carbon uptake over the coming century, as well as the nature of possible feedbacks between climate and the carbon cycle. To date, two general circulation climate models have been used to simulate the future behaviour of the carbon cycle, and the results thus far have yielded dramatically different projections of the future of the terrestrial carbon sink. Cox et al. (2000) were the first to publish results from a general circulation climate model coupled to a carbon cycle model (HadCM3C). In their study, the Hadley Centre model was forced from 1850 to present by observed emissions of CO_2 and non-CO_2 greenhouse gas increases, and then by the IS92a emissions scenario through the 21^{st} century. This simulation revealed a dramatic positive feedback to climate resulting from large releases of soil carbon under climate warming, as well as a significant die-back of South American tropical forests and consequent flux of carbon to the atmosphere. Terrestrial carbon uptake decreased throughout the simulation, and the land biosphere became a carbon source around the year 2050.

A similar study was carried out by Friedlingstein et al. (2001) and Dufresne et al. (2002) using the IPSL-CM2 model forced by CO_2 emissions from 1850 to 2100. This study supported the notion of a positive feedback to climate from the carbon cycle, but found the magnitude of the feedback to be less than a third of that seen in Cox et al. (2000). While terrestrial uptake in the 21^{st} century was reduced in this simulation, the IPSL model did not reproduce the terrestrial carbon sink-to-source transition seen in Cox et al. (2000). Dufresne et al. (2002) did not include dynamic

vegetation in their study, and so could not be expected to reproduce the dramatic changes in vegetation cover seen by Cox et al. (2000). They contend, however, that the main difference between the two studies lies in the response of the soil carbon pool to climate change.

The differences between these two model runs were the focus of a subsequent paper by Friedlingstein et al. (2003). The authors identified three key factors that could influence the magnitude of climate-carbon cycle feedbacks. The first was the model's climate sensitivity: a higher climate sensitivity implies more simulated warming for a given increase in atmospheric CO_2, which would lead to a stronger climatic impact on the carbon cycle. Secondly, the response of ocean circulation to climate change, and hence the geochemical uptake of anthropogenic carbon differed considerably between models. Third, the response of soil and vegetation carbon uptake to climate change was highly model dependent. Friedlingstein et al. (2003) analysed these processes and determined that the differences in model climate sensitivities, ocean circulation responses and terrestrial vegetation dynamics were of secondary importance to the extent to which soil carbon pools in the two models were affected by climate warming.

In this chapter, I present evidence that suggests instead that the magnitude and character of model-simulated climate change over the 21^{st} century may have a dominant impact on the resultant feedbacks between the terrestrial carbon cycle and climate. I use a new version of the UVic Earth System Climate Model (ESCM) (Weaver et al. 2001), now coupled to a dynamic terrestrial vegetation and carbon cycle model, as well as an inorganic ocean carbon cycle component, as described in Sections 2.2 and 2.3. The UVic model is a global climate model of intermediate complexity, and as such allows for multiple transient model runs under a range of climate scenarios. Repeated simulations can also be carried out to assess the sensitivity of climate feedbacks to key processes and parameters in the model. In addition, the terrestrial component of this model is taken from that used in HadCM3C — this

allows for an assessment of the extent to which the large positive feedbacks seen in Cox et al. (2000) can be reproduced using a different climate model.

With this new tool, I investigate the role of the terrestrial biosphere in moderating and responding to recent and future scenarios of climate change. The UVic ESCM and carbon cycle components are described in Chapter 2; the following sections describe the experimental setup and results of the model simulations. Section 5.3.1 presents the results of model runs of the 20^{th} century, validating them against available observations. Section 5.3.2 focuses on the 21^{st} century, demonstrating the model response to six CO_2 emissions scenarios. I discuss simulated atmospheric CO_2 and temperature trends, as well as changes in terrestrial and ocean carbon sinks. I then focus on the magnitude of terrestrial carbon cycle feedbacks to climate and present the results of a sensitivity study to assess the importance of key model processes in determining the strength of the feedback.

5.2 Experimental Descriptions

In this chapter, transient runs were performed from 1750 to 2100, forced by observed and projected anthropogenic carbon dioxide emissions. For the historical period (1750 to 2000), CO_2 emissions from combustion of fossil fuels were taken from Marland et al. (2002); land-use emissions were specified for the period from 1850 to 2000 from Houghton (2003a). From 1750 to 1850, emissions from land cover change were linearly interpolated from zero at 1750 to the 1850 value corresponding to the first year in the Houghton (2003a) dataset.

Historical methane emissions were prescribed (Stern and Kaufmann 1998) and allowed to decay to carbon dioxide with an atmospheric lifetime of 8.4 years, providing a small additional source of carbon dioxide from anthropogenic activities. There was no direct radiative forcing applied from methane on the climate system, other than

that which results from the formation of CO_2. Consumption of methane in the soil and methane loss to the stratosphere was omitted, although these have been estimated to constitute only about 10% of the total sink for anthropogenic methane (Prather et al. 2001). This is a highly simplified parameterisation of the fate of methane in the atmosphere, but does provide a first-order approximation of the contribution of anthropogenic methane to the atmospheric carbon budget.

From 2000 to 2100, fossil fuel and land cover change emissions are specified from scenarios A1B, A1T, A1F1, A2, B1 and B2 of the IPCC Special Report on Emissions Scenarios (SRES) (Nakićenović et al. 2000). Emissions from the six scenarios, as well as for the historical period, are shown in Figure 5.1. Due to a discrepancy between land-use emissions given in the SRES scenarios at the year 2000, and year 2000 emissions estimated by Houghton (2003a), the land-use emissions from each of the SRES scenarios were scaled up so as to be consistent with the Houghton (2003a) dataset. In doing this, the SRES land-use emissions were increased slightly, but the emission trends throughout the 21^{st} century were preserved. All transient model runs presented here began from an equilibrium simulation with atmospheric CO_2 set to 280 ppmv. Present-day croplands from Ramankutty and Foley (1999) were prescribed onto this equilibrium climate so that historical land-use CO_2 emissions did not duplicate carbon already stored in the terrestrial biosphere. For these simulations, natural climate forcings and anthropogenic forcings other than CO_2 (including the transient biogeophysical effect of land cover change) were ignored.

5.3 Results and Discussion

5.3.1 20^{th} Century

Figure 5.2 shows modelled atmospheric carbon dioxide and temperature compared to data from Etheridge et al. (1998) and Keeling et al. (2003a,b) for CO_2, and Fol-

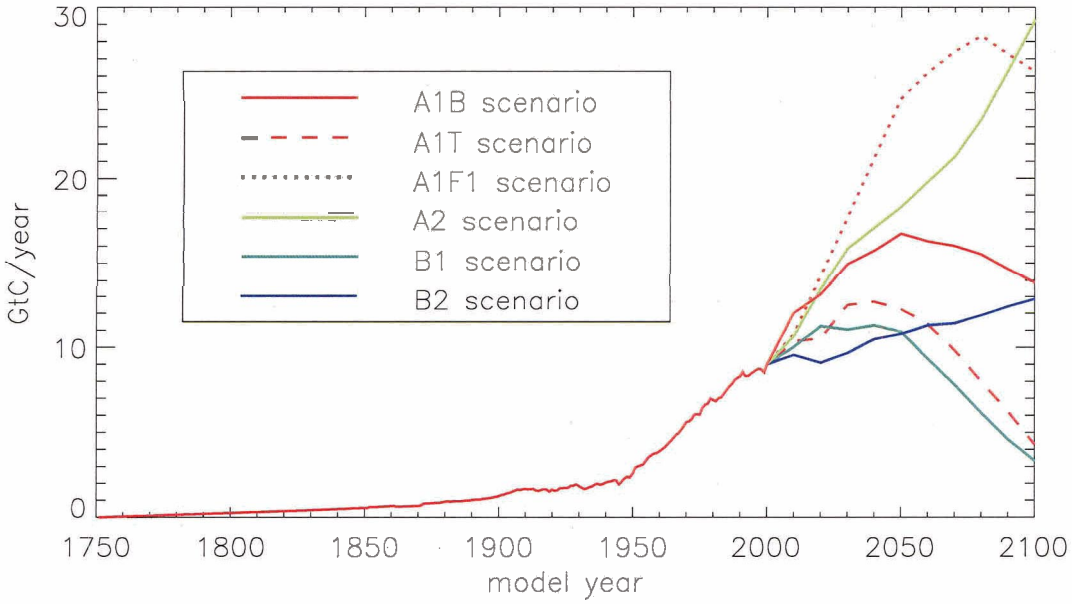

Figure 5.1: **Anthropogenic carbon dioxide emissions from observations for 1750 to 2000 and from six marker SRES scenarios from 2000 to 2100.**

land et al. (2001) for temperature. The model does a very good job of reproducing historical CO_2 concentrations, reaching 366 ppmv at the year 2000 (compared to the observed 368 ppmv). Particularly in the latter portion of the 20^{th} century, the observed CO_2 increase is well reproduced, with most of the model-data discrepancy occurring prior to 1950. Of the simulated 86 ppmv CO_2 increase from pre-industrial conditions to present-day, about 30 ppmv can be attributed to emissions from historical land-use change. Decay of anthropogenic methane accounts for a small additional source of CO_2, contributing 3 to 4 ppmv of atmospheric CO_2 increase.

Simulated temperature in Figure 5.2 shows a good agreement with data, although the interannual variability is not captured on account of the reduced complexity of the atmosphere component of the model. Decadal-scale variability, such as the warming in the early part of the 20^{th} century followed by slight cooling, is also not seen in this simulation. This lower frequency variability is thought to be largely the result of natural climate forcings such as solar insolation changes and volcanic activity (Stott

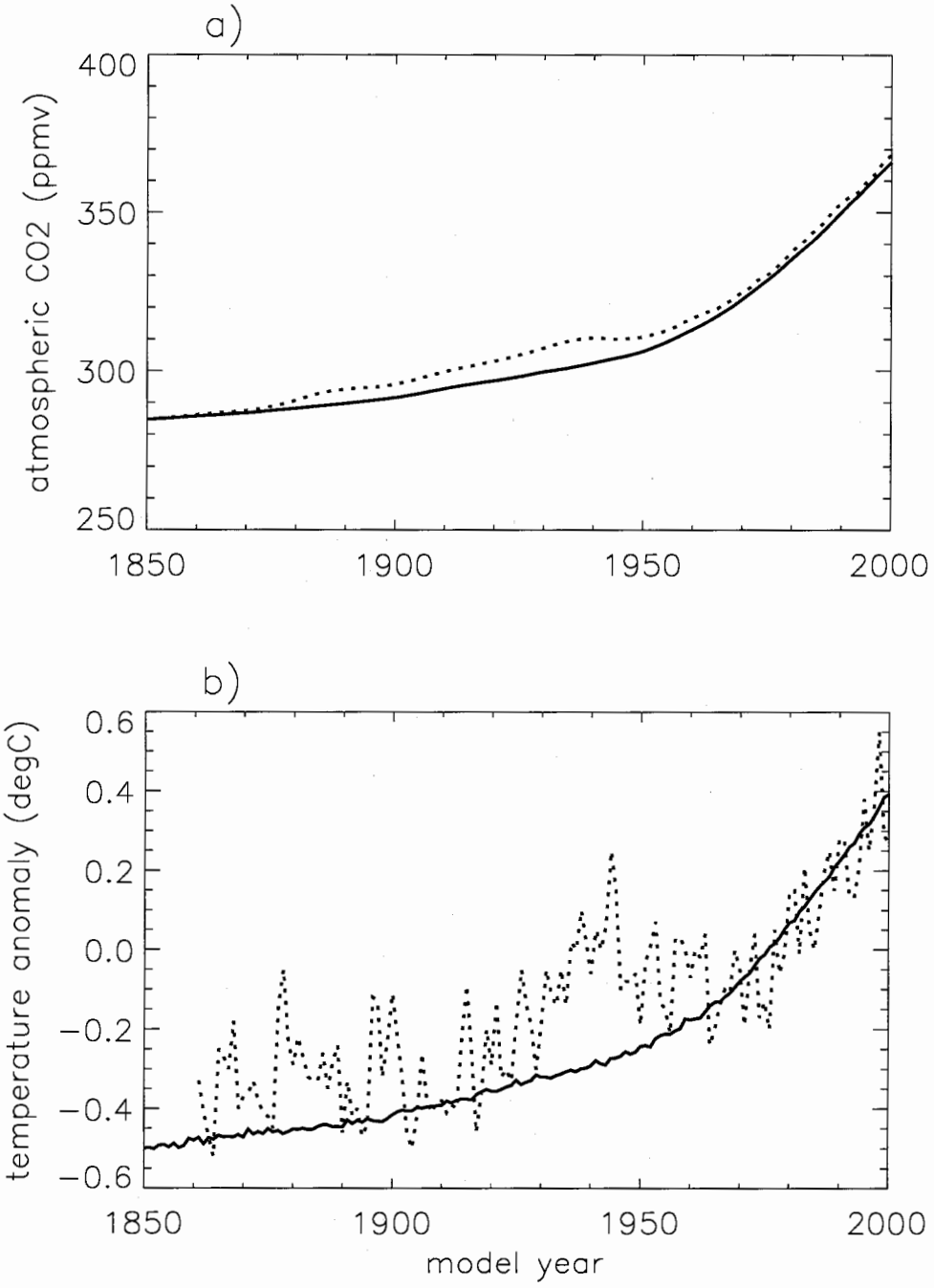

Figure 5.2: **Modelled (a) atmospheric carbon dioxide and (b) temperature anomaly with respect to the 1961-1990 average (solid lines), compared to observations (dotted lines).**

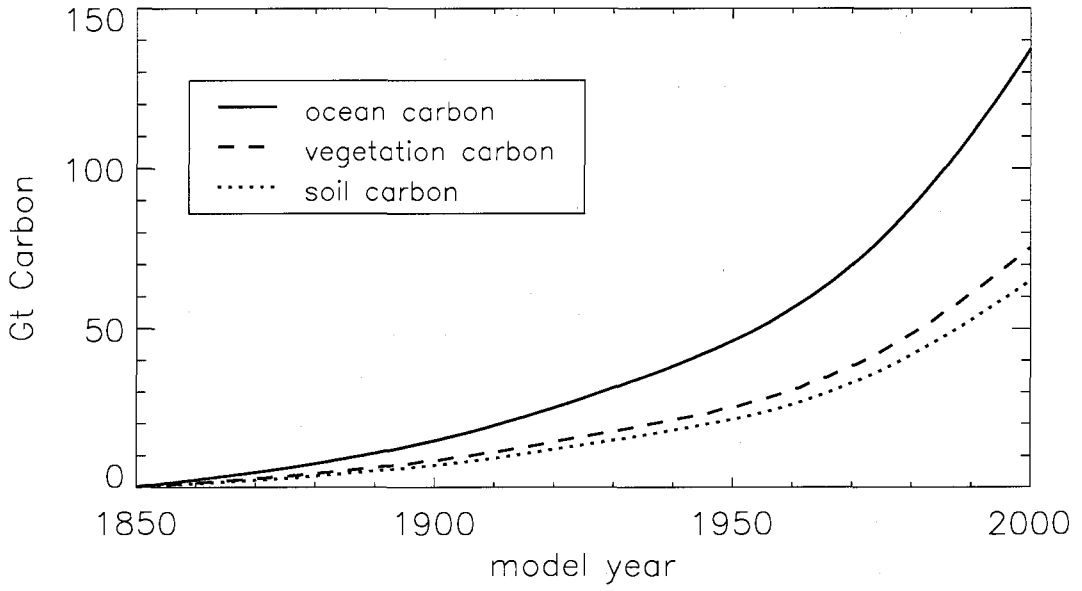

Figure 5.3: **Increases in ocean (solid line), vegetation (dashed line) and soil (dotted line) carbon sinks from 1850 to 2000.**

et al. 2000, 2001, see also Chapter 4) which are not included in the current simulations (see Chapter 4 for a detailed analysis of the UVic ESCM's response to contemporary climate forcings). It is possible that inclusion of these climate forcings would also improve the simulation of atmospheric CO_2 in the early part of the century, as this would allow for a more accurate response of CO_2 to changes in climate via climate-carbon cycle feedbacks (discussed further in Section 5.3.2).

Figure 5.3 shows the accumulation of carbon in ocean and terrestrial sinks from 1850 to 2000. From 1850 to 1998, vegetation carbon increased by 72 GtC and soil carbon by 63 GtC, giving a total land carbon increase of 135 GtC. Specified emissions from land-use change (Houghton 2003a) totalled 152 GtC, yielding a net carbon source of 17 GtC over this time period. This is quite consistent with the estimate of a 26±60 GtC source given in Bolin et al. (2000). Ocean carbon from 1850 to 1998 increased by 132 GtC; this leaves an accumulation of 170 GtC in the atmosphere, slightly less than, but within the error bounds of the Bolin et al. (2000) figure of 176±10 GtC.

In Figure 5.4, I show the globally averaged annual terrestrial carbon flux (net ecosystem productivity, in GtC/year) as a function of time from 1850 to 2000 (dashed line). This plot shows that the terrestrial carbon cycle does take up carbon throughout the model simulation, although the strength of the sink increases notably after 1950, reaching 2.7 GtC/year by the year 2000. Also shown on this plot are the specified land-use emissions (dotted line) and the sum of emissions and uptake (solid line). This latter line represents the net terrestrial carbon flux, or the net biome productivity. For most of the simulation, when land-use emissions are included, the terrestrial biosphere acts as a net source of carbon (as noted above for the 1850-1998 total). Around 1970, however, terrestrial uptake exceeds emissions from land-use change, and the terrestrial biosphere becomes a net carbon sink. This pattern is consistent with that seen in simulations using terrestrial ecosystem models forced offline by observed CO_2, land-use and climate changes (McGuire et al. 2001, Levy et al. 2004). Deconvolution analyses of ice-core CO_2 records also reveal similar magnitudes and temporal progression of net terrestrial carbon fluxes, though the transition from a net land source to a net land sink occurs slightly earlier at around 1950 (Joos et al. 1999, Trudinger et al. 2002).

It is important to note that the mechanism of terrestrial carbon uptake in the UVic model (as well as in most other terrestrial ecosystem models) is enhanced gross primary production resulting from increased atmospheric CO_2 (i.e., CO_2 fertilization). While there is considerable uncertainty as to the long term effect of elevated CO_2 on plant growth and terrestrial carbon sequestration, and as such it is difficult to validate this result against observations, there is new evidence to suggest that changes in other climate variables may also be contributing to increased net primary production. Nemani et al. (2003), in a recent analysis of satellite records of vegetation characteristics over the period from 1982 to 1999, estimated that global annual NPP has increased by 3.42 GtC over the 18 year period studied, and argued that

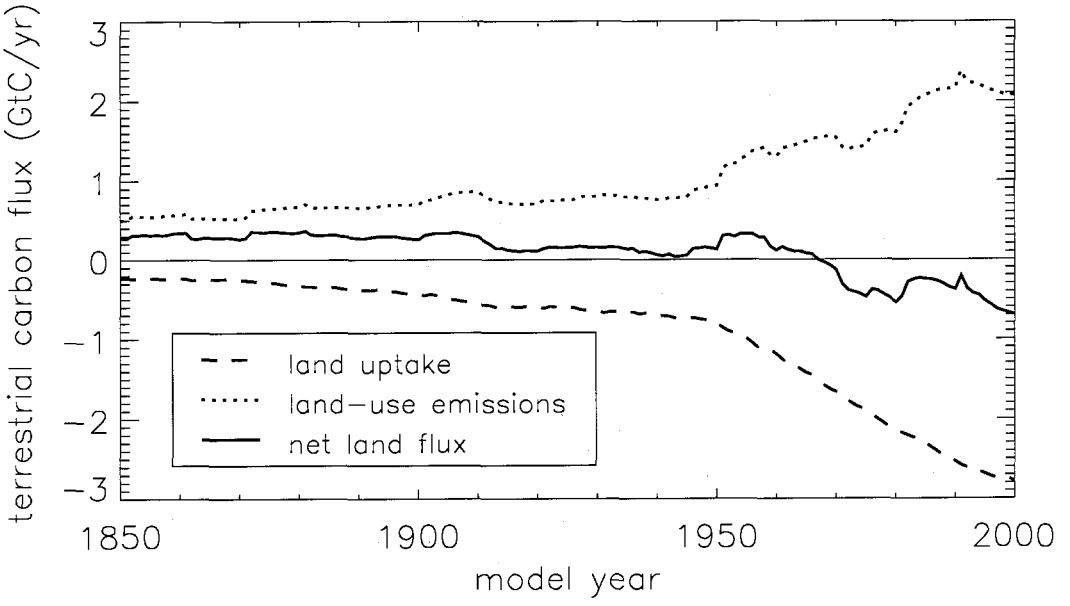

Figure 5.4: **Terrestrial carbon uptake (dashed line), emissions from land cover change (dotted line, Houghton 2003a) and the net terrestrial carbon flux (solid line). Negative values indicate a withdrawal of carbon from the atmosphere.**

almost 40% of the estimated NPP increase could be attributed to the direct effects of climate changes (such as changes in temperature, soil moisture and cloud cover), with the remainder likely resulting from changes in land-use, vegetation distributions and growth fertilization. While the UVic model simulates a similar global annual NPP increase over this period (3.68 GtC/year), the effect of CO_2 fertilization is by far the dominant effect. When modelled CO_2 increases were prevented from affecting vegetation growth in the model (this scenario is discussed further in the following section) climatic changes alone lead to an increase in NPP in extratropical forests and a decrease in NPP in the tropics, with very little change in the global average.

Uptake by the ocean and terrestrial biosphere for the 1980s and 1990s, as well as from 1850 to 1998, is summarized in Table 5.1 and compared to the values given in Bolin et al. (2000), Plattner et al. (2002) and Houghton (2003a). The values simulated by the model for atmospheric carbon increase, ocean uptake, terrestrial uptake and

Table 5.1: **Modelled annual average CO_2 budget for the 1980s, 1990s (in GtC/year)[1] modelled totals for 1850 to 1998 (in GtC)[1] compared to estimates given in the IPCC special report on *Land Use, Land-Use Change and Forestry* (Bolin et al. 2000), updated where available for the 1980s and 1990s by Plattner et al. (2002) and Houghton (2003a).**

		1980s	1990s	1850 to 1998[2]
Atmospheric Increase:	Model	3.1	3.4	170
	Estimate[2]	3.3 ± 0.2	3.3 ± 0.2	176 ± 10
Ocean Uptake:	Model	-2.2	-2.6	-132
	Estimate[3]	-1.7 ± 0.6	-2.4 ± 0.7	-120 ± 50
Terrestrial Uptake:	Model	-2.3	-2.7	-135
	Estimate[4]	-2.4 ± 1.1	-2.9 ± 1.1	-126 ± 80
Land-use Emissions:	Model[5]	2.0	2.2	152
	Estimate[4]	2.0 ± 0.8	2.2 ± 0.8	
Net Terrestrial Flux:	Model	-0.3	-0.5	17
	Estimate[3]	-0.4 ± 0.7	-0.7 ± 0.8	26 ± 60

[1] Negative values indicate a withdrawal of CO_2 from the atmosphere.
[2] From Bolin et al. (2000).
[3] From Plattner et al. (2002).
[4] From Houghton (2003a).
[5] Specified in the model from Houghton (2003a).

the net terrestrial flux (calculated as the sum of simulated uptake and specified land-use emissions) are all very close to the estimates for the 1980s and 1990s, as well as for the period from 1850 to 1998 as discussed above. This does suggest that despite substantial uncertainties in the mechanisms of terrestrial carbon sequestration, the UVic model does a good job of reproducing the observed behaviour of global carbon sinks.

5.3.2 21st Century

5.3.2.1 SRES Scenario Results

Six SRES emissions scenarios (A1B, A1T, A1F1, A2, B1 and B2) were used to force the model from the year 2000 to 2100, generating a range of model responses to future climate change scenarios. Simulated atmospheric CO_2 and temperature changes from

these six runs are shown in Figure 5.5. Simulated atmospheric CO_2 at the year 2100 ranged from 500 ppmv (B1 scenario) to 885 ppmv (A1F1 scenario). Temperature increases over the 21^{st} century ranged from 1.4 to 3.0 °C. These numbers are in general agreement with those presented in Houghton et al. (2001), which were based on simulations using simplified models of climate and the carbon cycle. The CO_2 increases simulated by the UVic model are on the lower end of the range of results obtained from this same set of emission scenarios (500 to 1250 ppmv at the year 2100: Prentice et al. 2001). The simulated warming over the 21^{st} century is also at the low end of the range reported in Houghton et al. (2001) (1.4 to 5.8 °C); this is a direct consequence of simulated CO_2 levels, given that the UVic model's climate sensitivity is close to the average of the range of climate models discussed in Houghton et al. (2001).

Vegetation and soil carbon increases for the same series of model runs are shown in Figure 5.6. All model scenarios show a smooth increase in vegetation and soil carbon, with vegetation carbon increasing by 135 to 230 GtC and soil carbon by 110 to 200 GtC over the 21^{st} century. Total land and ocean carbon uptake (shown in Figure 5.7) ranges from 245 to 430 GtC and from 370 to 650 GtC respectively. It is interesting to note that for the early part of the 21^{st} century, land and ocean carbon sinks increase at a very similar rate, and contribute approximately equally to the total sequestration of anthropogenic carbon. After 2050, however, the behaviour of the land and ocean carbon sinks begin to diverge: both continue to take up carbon in response to anthropogenic emissions, but the land biosphere shows signs of saturation, and the resulting cumulative uptake amounts at the year 2100 are notably lower than those for the ocean. This saturation is a sign of the diminishing effectiveness of CO_2 fertilization at high CO_2 values in the model, as well as temperature driven increases in soil and plant respiration.

The distribution of terrestrial carbon increases on the model grid and by latitude, are shown in Figure 5.8 for the A2 scenario run. From both of these plots it is apparent

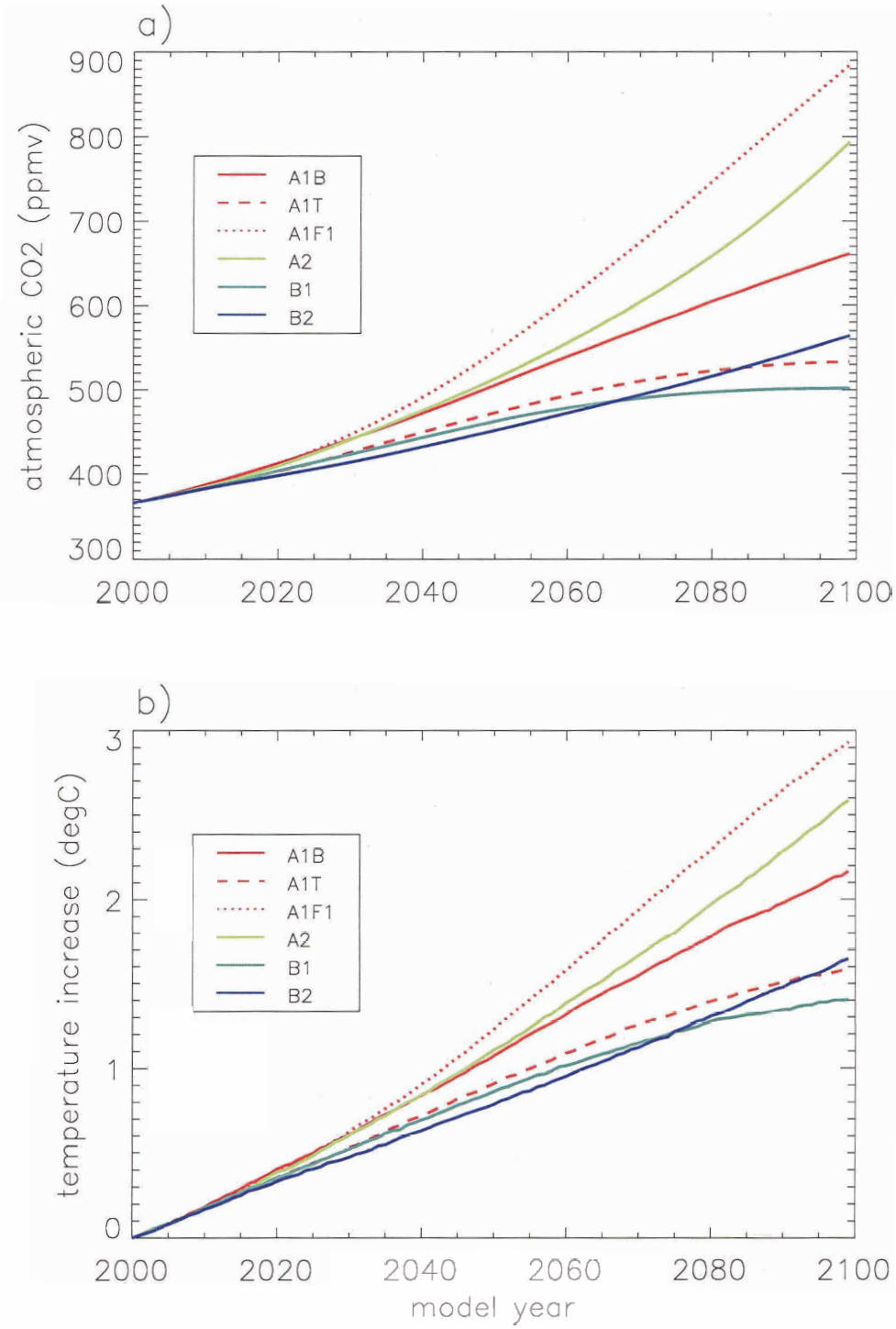

Figure 5.5: **Modelled (a) atmospheric CO_2 and (b) temperature increase for model runs from 2000 to 2100 under six SRES marker scenarios of greenhouse gas emissions.**

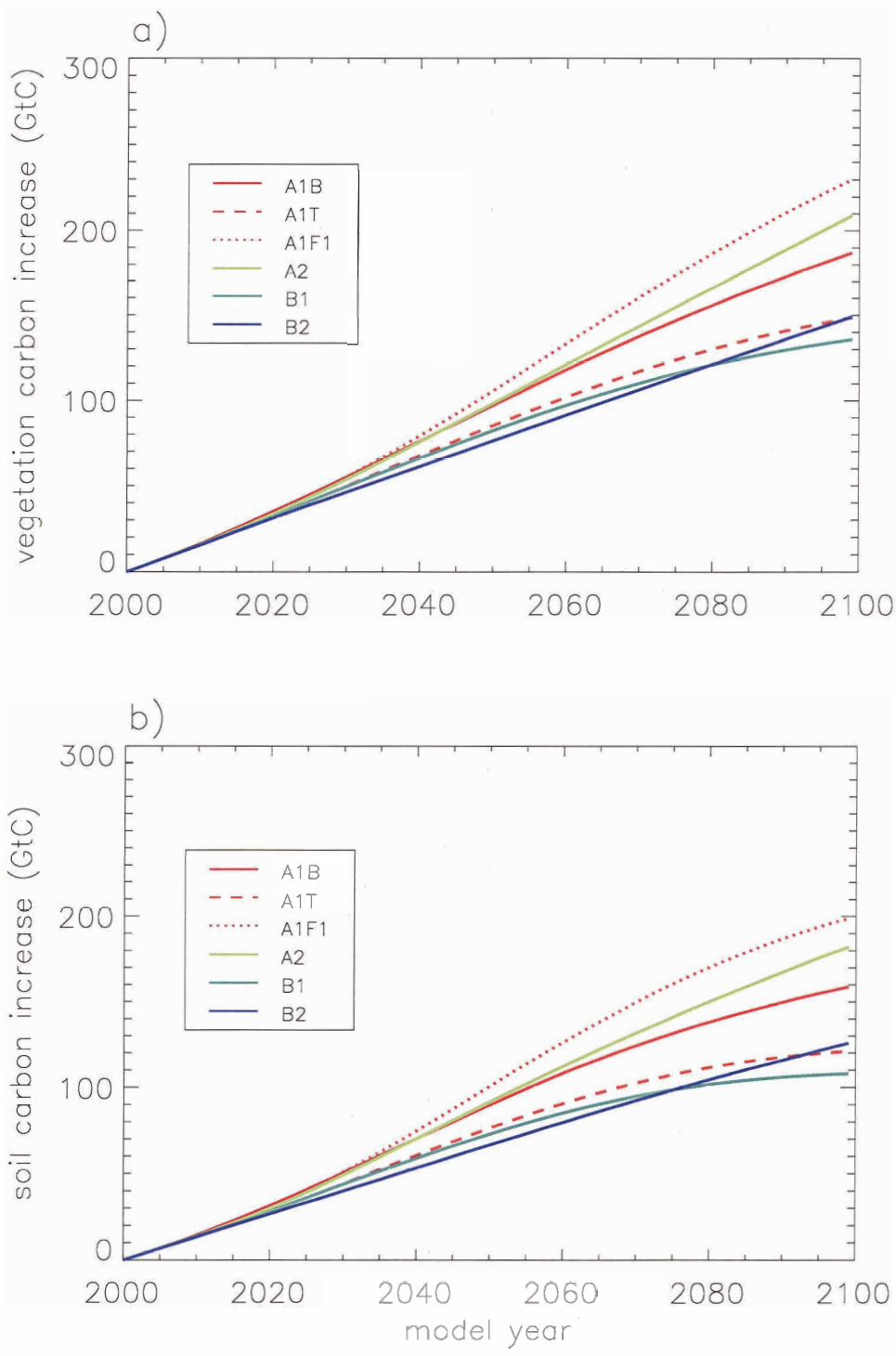

Figure 5.6: **Modelled (a) vegetation and (b) soil carbon increase for model runs from 2000 to 2100 under six SRES marker scenarios of greenhouse gas emissions.**

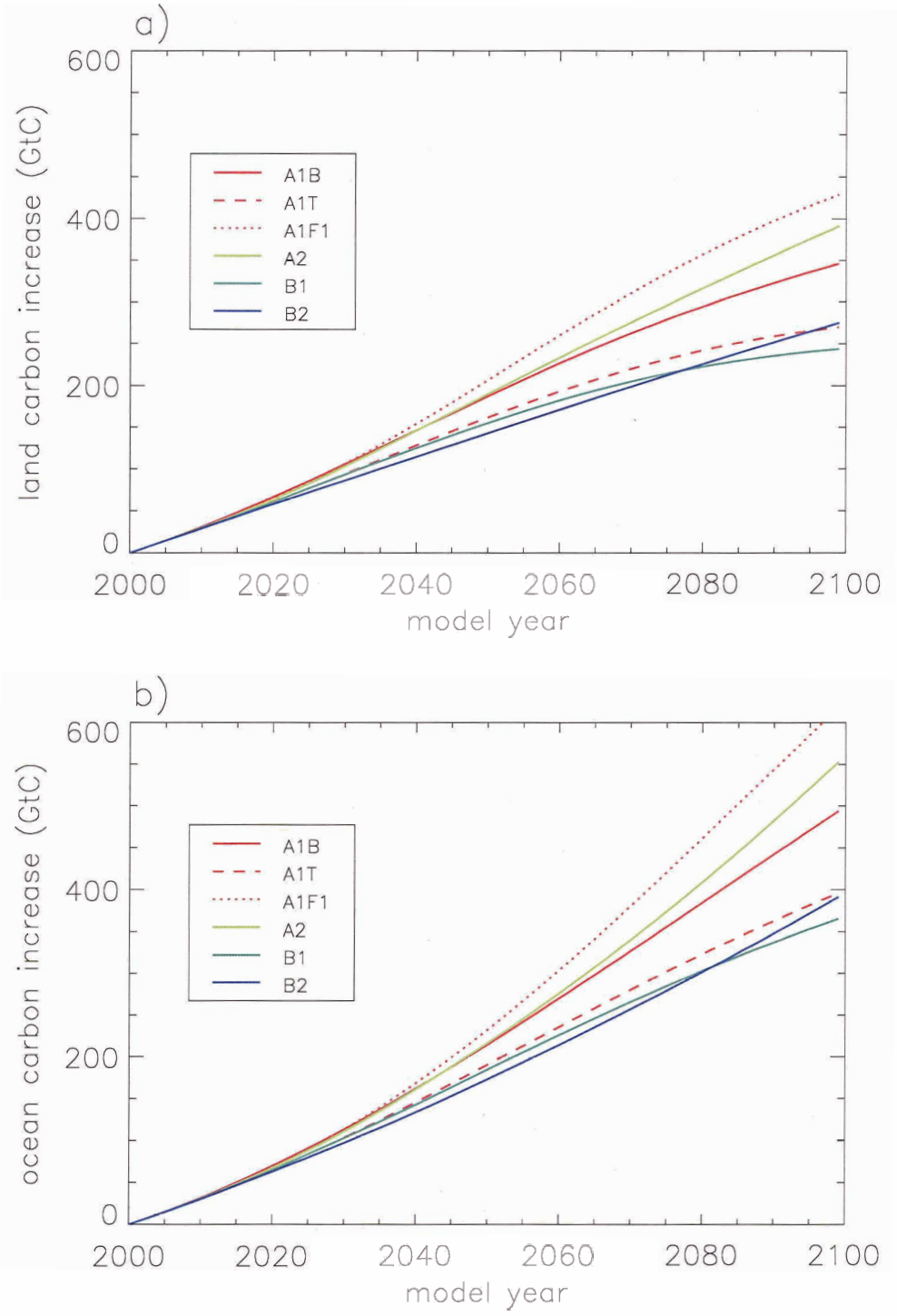

Figure 5.7: **Modelled (a) total land and (b) ocean carbon increase for model runs from 2000 to 2100 under six SRES marker scenarios of greenhouse gas emissions.**

that the majority of simulated terrestrial uptake occurs in the tropics, although mid- to high latitude boreal forests also contribute. It is notable that terrestrial carbon storage does not decrease at any location or latitude band in the model during the 21^{st} century.

It is important to note that the land carbon increases shown here do not include any removal (or addition) of carbon due to changing patterns of human land-use change. For all simulations, cropland distributions in the vegetation model were held fixed at present-day values (corresponding to those provided in the last year of the Ramankutty and Foley (1999) dataset). Land-use CO_2 emissions were included in the specified SRES emission scenarios, and in some cases this may have led to a duplication of carbon in the model. This duplication is small however, as in all scenarios, land-use change is projected to decline over the next century, and cumulative land-use change emissions are less than 10% of those from fossil fuel combustion (Nakićenović et al. 2000). Nevertheless, as in the discussion of Figure 5.4, the net change in terrestrial carbon can be calculated as the sum of simulated terrestrial uptake and specified land-use emissions. This results in a reduced range of terrestrial carbon increases of between 235 and 335 GtC from the year 2000 to 2100.

The temporal evolution of the terrestrial carbon flux (heterotrophic soil respiration minus NPP) for the six SRES scenario runs is shown in Figure 5.9. This plot represents the annually averaged terrestrial carbon flux in response to changing climate and CO_2 (neglecting annual land-use change emissions), where negative values again correspond to a flux of carbon out of the atmosphere. In all six cases, the terrestrial biosphere remains a sink for carbon throughout the model run, although the transient behaviour of this sink is dependent on the specific scenario that is employed. In cases where CO_2 emissions increase throughout the model run (scenarios A2 and B2: see Figure 5.1) the terrestrial carbon sink remains much stronger than in cases where CO_2 emissions decline in the second half of the century (scenarios A1B, A1T,

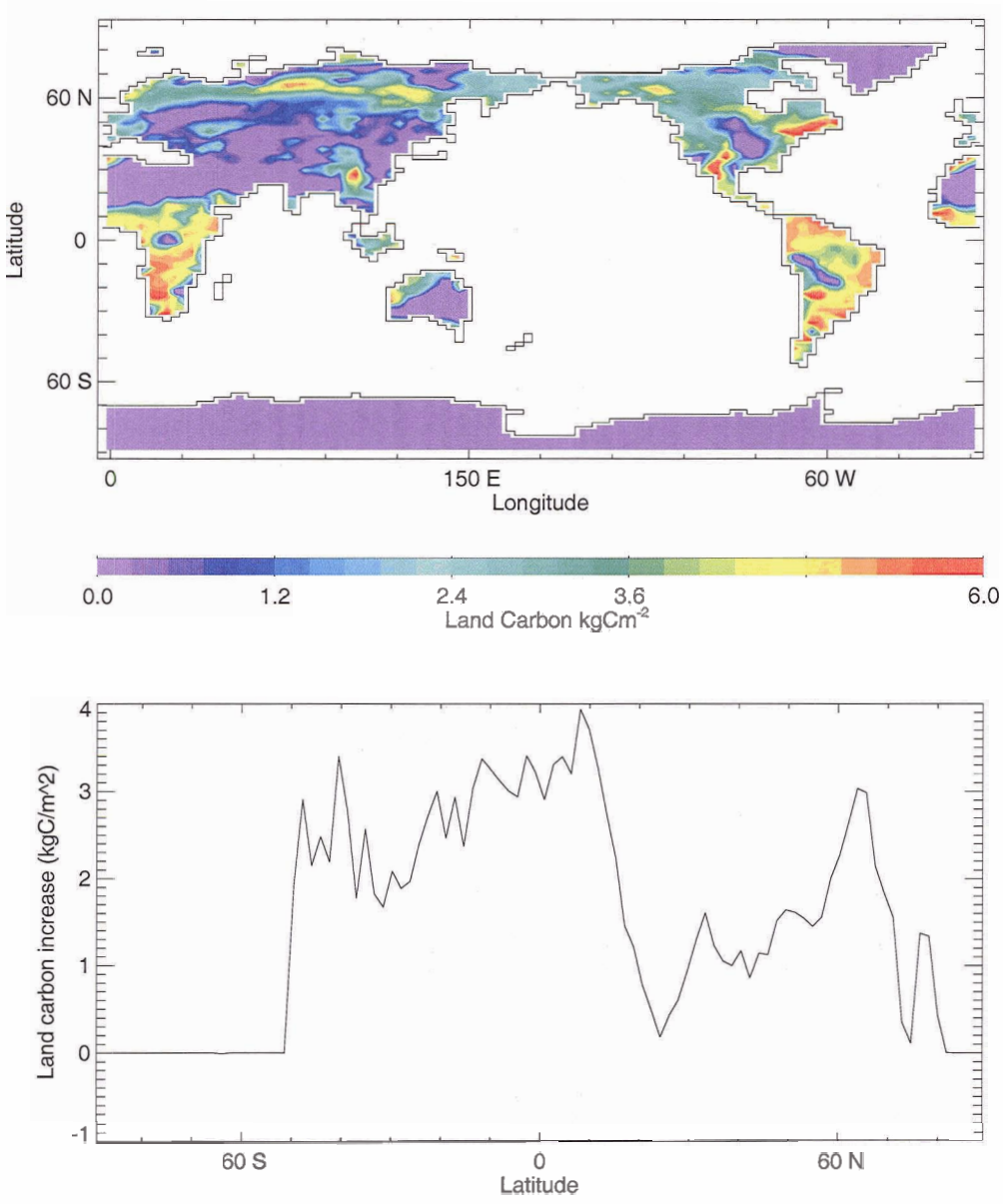

Figure 5.8: **Modelled increase in terrestrial carbon storage from 2000 to 2100 on the model grid (top) and by latitude (bottom) for the A2 scenario run.**

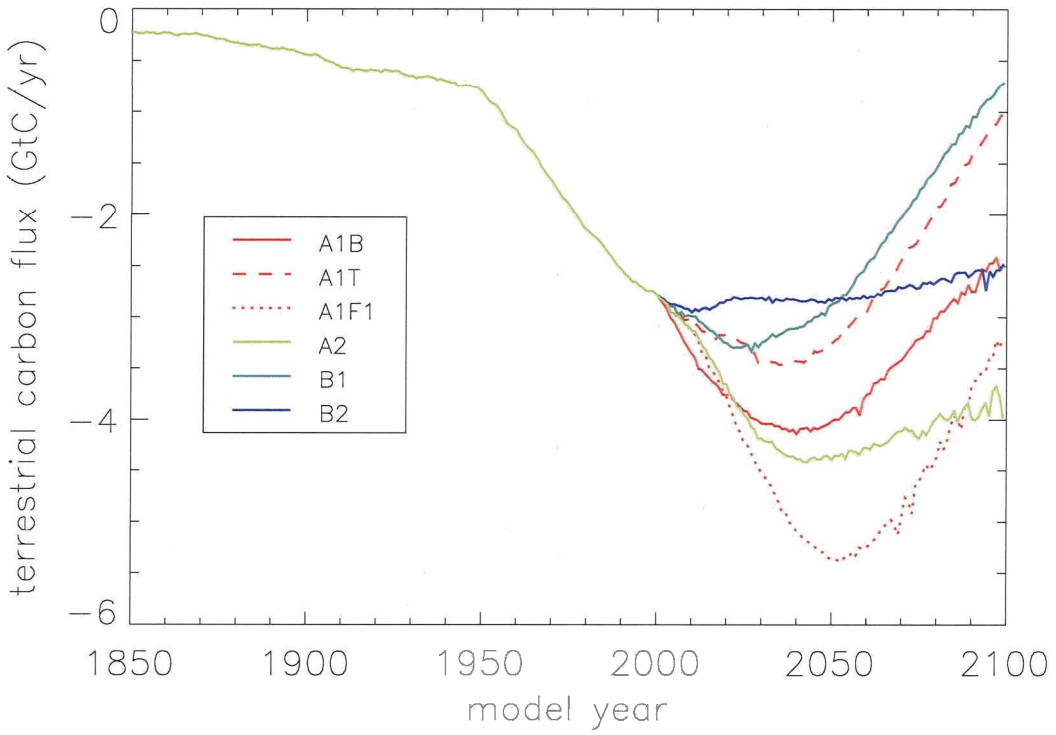

Figure 5.9: **Annually averaged global terrestrial carbon flux from 1850 to 2000 and from 2000 to 2100 for the six SRES scenario runs. Negative values indicate a net flux of carbon from the atmosphere into the terrestrial biosphere.**

A1F1 and B1). In these latter cases, the flux of carbon into the terrestrial biosphere decreases substantially toward the end of the simulation, and it is evident that this flux would reach zero (the transition point from a terrestrial carbon source to a sink) within another several decades of model simulation. In no case, however, does the terrestrial carbon cycle model simulate a transition from a sink to a source within the 21^{st} century.

Annual 21^{st} century land and ocean carbon fluxes can also be plotted as a fraction of yearly anthropogenic carbon emissions. Figure 5.10 shows fractional carbon uptake for the land and ocean, as well as the fraction of emissions that remain in the atmosphere from the A2 scenario simulation (A2 emissions are shown in Figure 5.1).

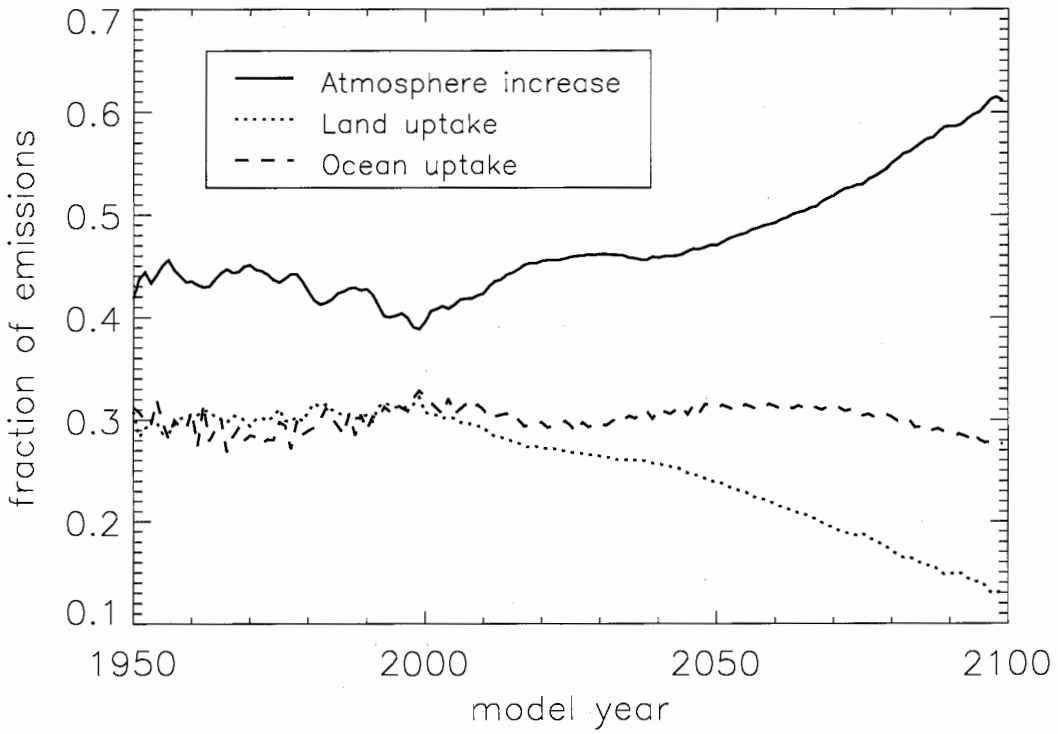

Figure 5.10: **Modelled atmospheric storage (solid line), land uptake (dotted line) and ocean uptake (dashed line) as a fraction of emissions for the A2 scenario, plotted from 1950 to 2100.**

Prior to about 2010, land and ocean sinks each take up close to 30% of CO_2 emissions, with 40 to 45% of emissions accumulating in the atmosphere. As emissions increase throughout the 21^{st} century, the ocean continues to take up a fairly constant fraction of emitted anthropogenic carbon. The fraction of emissions taken up by the land, however, begins to decline, reaching only 13% of emissions by the year 2100. This results in a steady increase in the fraction of emissions remaining in the atmosphere, and points again to a weakening of the terrestrial carbon sink relative to the ocean towards the end of this century.

The results presented in this section are generally consistent with previous coupled climate-carbon cycle simulations of the 21^{st} century (Cox et al. 2000, Dufresne et al. 2002). It is surprising, however, that my results are different from those of

Cox et al. (2000) in several important ways, given that the UVic and Hadley Centre models share common dynamic vegetation and terrestrial carbon cycle components. The striking result of Cox et al. (2000) was that under increasing 21^{st} century temperatures, terrestrial carbon uptake slowed dramatically, and the terrestrial biosphere became a carbon source around the middle of the century. In addition, Cox et al. (2000) simulated a dramatic die-back of South American forests as a result of hydrological feedbacks between vegetation distributions and climatic conditions in the Amazon basin. The UVic model does simulate a slowing of terrestrial uptake as a result of climate changes, but to a much lesser extent than HadCM3C. None of the model scenarios presented here show a sink-to-source transition in the 21^{st} century, as seen in Cox et al. (2000). I also do not see a decrease in Amazonian forests, but rather an increase in carbon sequestration throughout South America. Despite the commonalities between the UVic model and the model used by Cox et al. (2000), my simulations more closely resemble those of Dufresne et al. (2002).

In the next section, I address the question of why the UVic model results diverge from those of Cox et al. (2000). I focus on the magnitude of the carbon cycle feedback to climate seen in these simulations, and compare my results to those of Cox et al. (2000) and Dufresne et al. (2002). I then analyze the UVic results following the method of Friedlingstein et al. (2003), showing the sensitivity of carbon uptake in the UVic model to changes in atmospheric CO_2 and temperature. As one potentially important difference between the UVic model and HadCM3C is our respective climate sensitivities, I present an analysis of the effect of increased warming in the UVic model on the magnitude of the carbon cycle feedback to climate. Finally, I propose a mechanism that could explain the differences between my results and those of Cox et al. (2000) based on regional differences in simulated temperature and precipitation changes over the 21^{st} century.

5.3.2.2 Carbon Cycle-Climate Feedbacks

Climate changes likely have several important effects on terrestrial carbon uptake. On the one hand, increased temperatures could lead to a longer growing season, which would create a negative feedback on atmospheric CO_2 as a result of increased vegetation growth. Conversely, higher temperatures increase plant and soil respiration, leading to a decreased total terrestrial carbon uptake and a net positive feedback to climate. Changes in precipitation and soil moisture would also have an effect both on vegetation growth and on the rate of soil carbon decomposition. Previous studies have focused on the effect of soil temperature on heterotrophic soil respiration as the dominant contributor to a net positive feedback between the terrestrial carbon cycle and climate (Cox et al. 2000, Friedlingstein et al. 2001, Dufresne et al. 2002, Berthelot et al. 2002, Friedlingstein et al. 2003).

In this section, I introduce several new model runs to assess the magnitude of carbon cycle-climate feedbacks in the UVic model. The first is a simulation where modelled increases in atmospheric CO_2 did not apply any change in radiative forcing to the climate system. This means that the carbon cycle components of the climate model did not see any CO_2-induced changes in climate throughout the model run, and respond instead under constant pre-industrial climate conditions. The results of this simulation reflect a scenario in which there are no feedbacks between the carbon cycle and climate, and can be compared directly to similar runs carried out by Cox et al. (2000) and Dufresne et al. (2002). Second, modelled increases in carbon dioxide were masked from the terrestrial carbon cycle component of the model, which was instead forced by constant pre-industrial CO_2. This simulation resulted in a modelled CO_2 increase in the absence of the beneficial effects of CO_2 fertilization on terrestrial carbon uptake.

Figure 5.11 shows the simulated atmospheric CO_2 from these two model runs (dashed and dotted red lines) compared to the standard A2 model run, as presented

in the previous section (solid red line). The difference between the "no carbon cycle-climate feedback" model run and the standard A2 model run indicates the magnitude of the positive feedback between the carbon cycle and climate in the UVic model. As can be seen in this figure, the difference in simulated atmospheric CO_2 at the year 2100 is only about 60 ppmv, indicating a fairly weak positive feedback in our model. The difference between the "no CO_2 fertilization of vegetation" model run and the standard A2 run is notably larger: around 250 ppmv difference in CO_2 at the year 2100. Given the present uncertainty regarding the long-term effects of elevated CO_2 on plant growth and consequent terrestrial carbon sequestration, this simulation can be viewed as an upper bound for the evolution of 21^{st} century atmospheric CO_2 in the absence of CO_2-induced drawdown by terrestrial ecosystems. Also shown in this figure are the cumulative carbon emissions from the A2 scenario (solid black line): this represents the atmospheric CO_2 concentration that would result in the absence of uptake by both land and ocean carbon sinks.

Again, the differences between the results seen in the UVic model and those reported in Cox et al. (2000) are striking. In their coupled climate-carbon cycle experiment, atmospheric CO_2 at the year 2100 was 250 ppmv higher than in their "offline" simulations, in which the carbon cycle was forced by pre-industrial climate conditions. For the same set of model scenarios, the UVic model simulates a 60 ppmv CO_2 difference, which is more consistent with the 75 ppmv CO_2 difference simulated by the IPSL model (Dufresne et al. 2002). This is surprising given the commonalities between the UVic carbon cycle model and the HadCM3C model used by Cox et al. (2000).

Friedlingstein et al. (2003) attempt to explain the differences between the Hadley and IPSL simulations by comparing the sensitivities of land and ocean carbon uptake in the two models to changes in atmospheric CO_2 and temperature. In Figure 5.12, I show these sensitivities for the UVic model. Panels (a) and (b) show the simulated

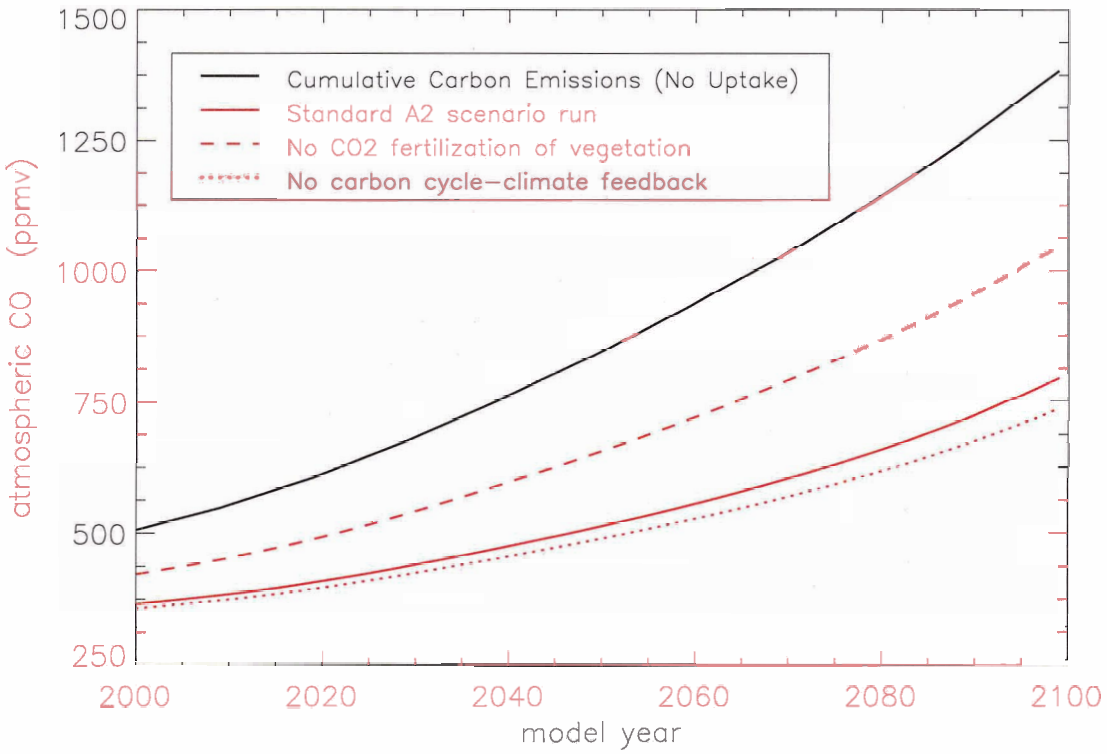

Figure 5.11: **Simulated atmospheric CO_2 from 2000 to 2100, forced by the SRES A2 scenario emissions. The standard A2 scenario run (solid red line) is compared to a run with constant climate (dotted red line) and constant atmospheric CO_2 (dashed red line). The solid black line is where there is no uptake by either land or ocean carbon sinks.**

ocean and land uptake as a function of atmospheric CO_2 for the "no carbon cycle-climate feedbacks" model run. This is the sensitivity of carbon uptake to CO_2 in the absence of climate change. Comparing these plots to Figure 3 in Friedlingstein et al. (2003), it is apparent that the effect of CO_2 increases on land uptake in the UVic model is virtually identical to that of the Hadley model, as would be expected given that we use the same terrestrial vegetation models. The sensitivity of ocean uptake to CO_2, however, is much more consistent with the IPSL model; both the UVic and IPSL models simulate a cumulative ocean uptake of around 650 GtC at 700 ppmv CO_2, compared to only about 400 GtC in HadCM3C.

This last result explains why the UVic "no carbon cycle-climate feedbacks" model run is very similar to Cox et al. (2000)'s "offline" run, despite the fact that I use the A2 emissions scenario which specifies higher CO_2 emissions throughout the 21^{st} century than the IS92a scenario used by Cox et al. (2000) (also noted as a difference between the IPSL and HadCM3C results in Friedlingstein et al. (2003)). Differences in ocean uptake in the absence of climate change do not explain, however, the differences in the simulated magnitudes of the carbon cycle-climate feedback. To assess the effect of temperature increases on land and ocean carbon uptake, Friedlingstein et al. (2003) plotted the changes in carbon uptake between the offline and fully coupled model runs as a function of modelled global temperature. As simulated CO_2 in the fully coupled model runs was higher than the offline simulations, carbon uptake in the fully coupled runs was first corrected based on the offline uptake sensitivity to CO_2.

The effect of temperature on ocean and land uptake in the UVic model (for the standard A2 scenario run) is shown in Figure 5.12 in panels c) and d) (these are equivalent to Figure 5 in Friedlingstein et al. (2003)). The effect of temperature changes lead to a 115 GtC decrease in ocean uptake over the course of the model simulation. This result is not very different from the decreases in ocean carbon uptake seen in either the IPSL model (-100 GtC) or the Hadley model (-125 GtC).

The effect of temperature leads to a 200 GtC decrease in land uptake in the UVic model, indicating that the land carbon cycle provides a larger contribution to the carbon cycle-climate feedback than does the ocean. This decrease is slightly less than that seen in the IPSL model (−300 GtC), and much less than that seen in the HadCM3C model (−1000 GtC). As was also concluded by Friedlingstein et al. (2003), while the response of the ocean to changes in climate does contribute to the positive feedback between the carbon cycle and climate, it is the response of land uptake to climate changes that largely determines the differences in feedback magnitudes seen in the two models. Friedlingstein et al. (2003), however, concluded that the differences between the Hadley and IPSL terrestrial uptake sensitivities to climate change could be largely attributed to differences in the terrestrial carbon cycle components used by the two models. This conclusion is not supported by the present study, as the differences between the UVic and Hadley model results are equally large despite the use of a common terrestrial carbon cycle model.

The differences between the UVic and Hadley results must therefore be explained by differences in simulated climate changes between the two models. It is notable that Cox et al. (2000) overestimated 20^{th} century warming (they simulated a 1.4 °C increase from 1860 to 2000) due to the inclusion of non-CO_2 greenhouse gas warming. In addition, Cox et al. (2000) simulated a 21^{st} century global temperature increase of 4 °C, compared to the UVic A2 scenario temperature increase of 2.6 °C. While the higher temperatures simulated by the HadCM3C model are an obvious consequence of higher atmospheric CO_2, a higher modelled temperature response to a given CO_2 concentration (the model's climate sensitivity) would also amplify the strength of carbon cycle-climate feedbacks, and increase both simulated atmospheric CO_2 and temperature.

To test to what extent differences in model forcings and climate sensitivity can reconcile the UVic and HadCM3C model results, I introduce two new simulations

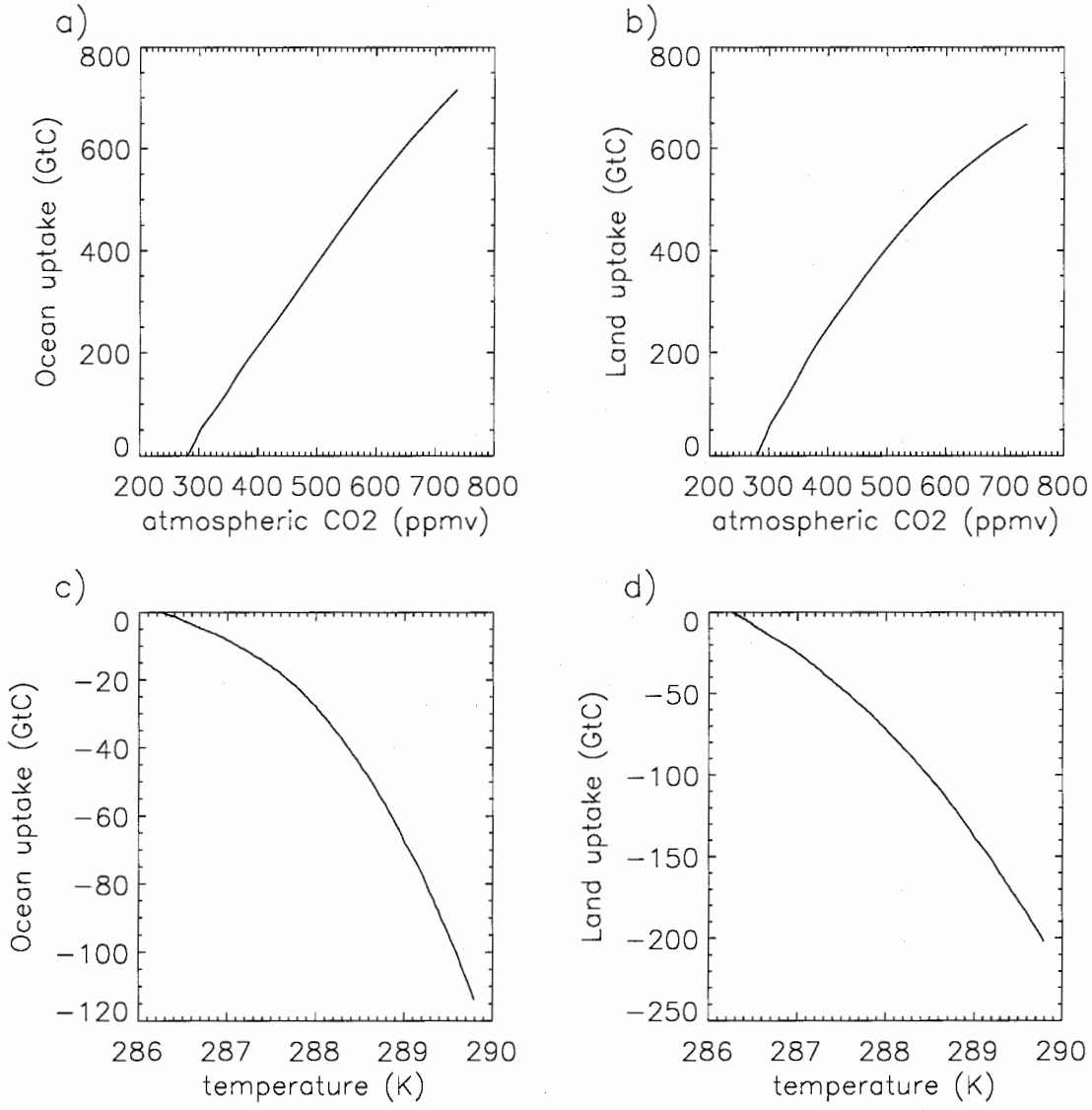

Figure 5.12: **Sensitivity of (a) ocean and (b) land carbon uptake to atmospheric CO_2 increases with constant climate, and sensitivity of (c) ocean and (d) land carbon uptake to changes in global temperature.**

forced by the A2 SRES scenario. The first included non-CO_2 greenhouse forcing as was done in Cox et al. (2000). The second further incorporated an increased climate response to CO_2, with the result that the climate sensitivity to doubled CO_2 was increased from 3 °C in the standard model configuration to 4.5 °C. This was done by multiplying the CO_2 increase used to calculate the CO_2 longwave forcing in Equation 2.1 by 1.8.

Simulated temperature and atmospheric CO_2 from these two model runs are shown in Figure 5.13, and compared to the standard A2 run and the no-feedbacks run discussed above. As can be seen in Figure 5.13a, including non-CO_2 greenhouse gas forcing increases 21^{st} century warming by 0.7 °C (dotted red line); further increasing the model's climate sensitivity generates an additional 0.85 °C temperature increase (dashed red line). Coupled with this temperature increase, is an increase in simulated atmospheric CO_2 at the year 2100 from 794 ppmv in the standard A2 run, to 826 ppmv when non-CO_2 greenhouse gas are included, and to 877 ppmv when climate sensitivity is also increased. Comparing this last result to the no-feedbacks case results in a 140 ppmv CO_2 difference at the year 2100 that can be attributed to the carbon cycle-climate positive feedback. This feedback is still substantially smaller than the 250 ppmv difference simulated by Cox et al. (2000).

Furthermore, as can be seen in Figure 5.14, while both of these two runs show a reduced terrestrial carbon sink compared to the standard A2 run (also shown in Figure 5.9), neither results in a sink-to-source transition during the 21^{st} century, as was found by Cox et al. (2000). It is also worth noting that in the increased climate sensitivity model run, the UVic model simulates a 4 °C warming over the 21^{st} century, which is consistent with the warming simulated by the Hadley model over the same period. However, this warming occurs in connection with a smaller CO_2 increase, indicating that the UVic model's climate sensitivity in this run slightly exceeds the climate sensitivity of HadCM3C. I conclude from this that differences in climate

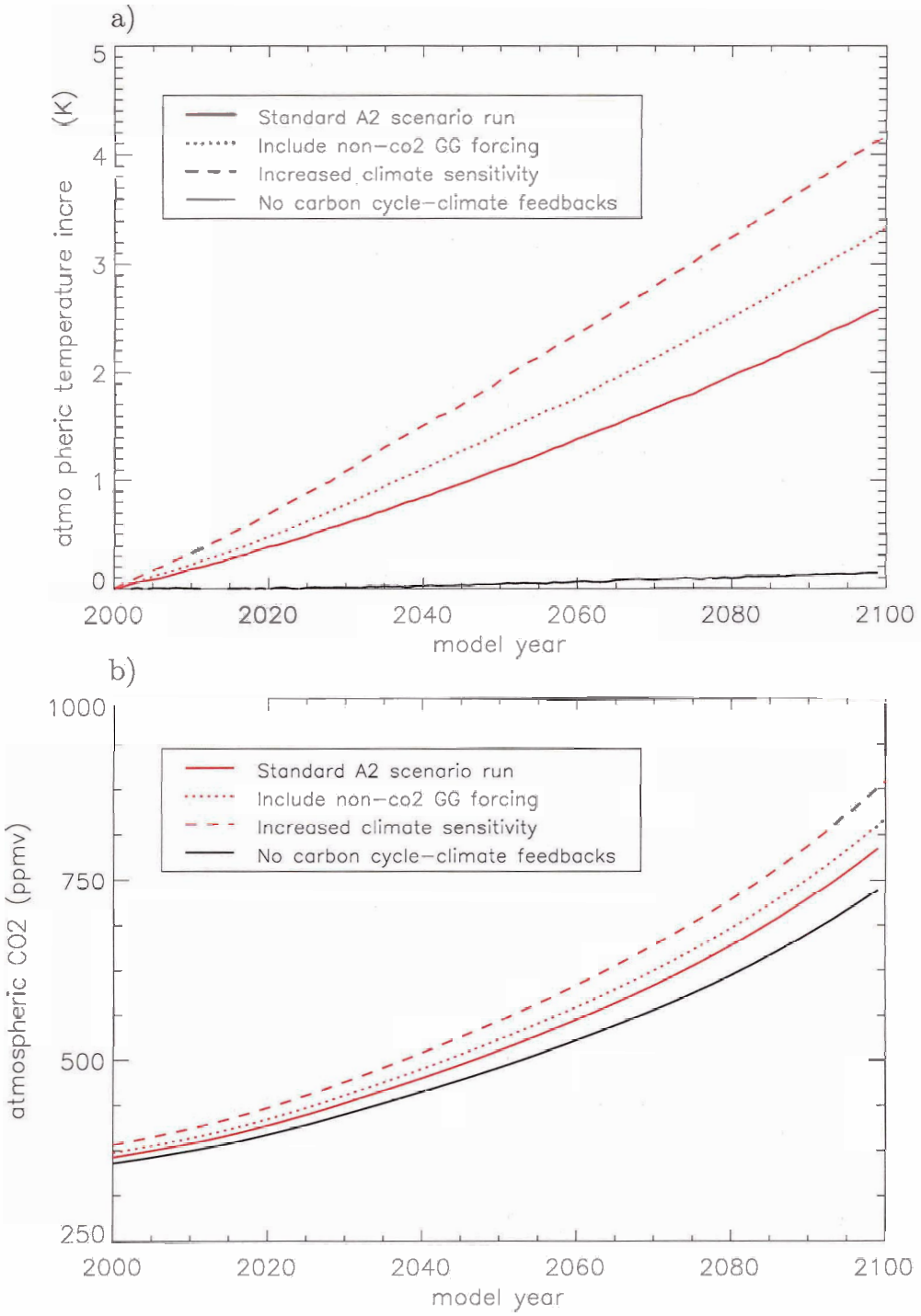

Figure 5.13: **Modelled (a) temperature and (b) atmospheric CO_2 changes from 2000 to 2100. The standard A2 scenario run (solid red line) is compared to a run that includes non-CO_2 greenhouse gas forcing (dotted red line) and a run that includes both non-CO_2 greenhouse gas forcing and increased climate sensitivity (dashed red line). The solid black line is the model run with constant pre-industrial climate; a small warming is evident in this run due to biogeophysical vegetation feedbacks.**

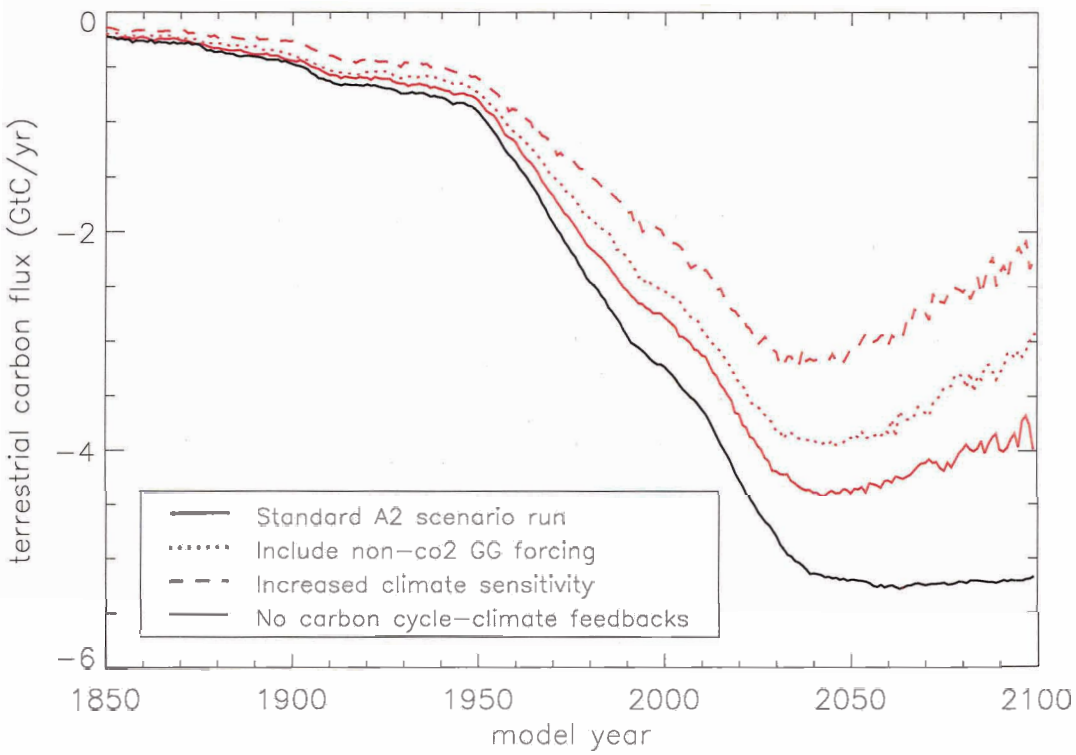

Figure 5.14: **As in Figure 5.13, showing here the net flux of carbon from the land to the atmosphere (excluding land cover change emissions). Negative values indicate a removal of carbon from the atmosphere.**

sensitivities between the UVic and Hadley models can account for some difference in the strength of simulated carbon cycle feedbacks, but cannot fully reconcile the results from the two models.

The remaining differences between the results presented in this chapter and those of Cox et al. (2000) must lie in differences in simulated climate variables other than globally averaged temperature. It was noted in the previous section that the UVic model does not simulate a die-back of South American forests as was seen in Cox et al. (2000). Dufresne et al. (2002) also do not simulate this die-back, although the IPSL model does not include vegetation dynamics, as do the UVic and Hadley models. Cox et al. (2000) attributed this forest decline to a combination of warming and drying in the Amazon basin, a conclusion that was supported by a recent analysis of

Amazon forest stability (Cowling et al. 2004). It seems likely that such a substantial climatically-induced decrease in vegetation productivity would play a critical role in reducing global NEP to the point where the terrestrial biosphere as a whole could become a carbon source.

An important difference between the UVic and Hadley models lies in their respective atmospheric components: the UVic ESCM has a simplified energy/moisture balance atmosphere, whereas HadCM3C includes a full atmospheric general circulation model. In the UVic model, present-day winds are specified in the atmosphere, and these (along with diffusion) are responsible for atmospheric moisture transport. While the UVic model does simulate precipitation changes over the 21^{st} century (notably a decrease in precipitation over most land areas, as shown in Figure 5.15a), these changes are not sufficient to decrease vegetation productivity, as occurred in Cox et al. (2000). Specifically, precipitation decreases over the Amazon basin do not result in decreases in soil moisture (Figure 5.15b) which would be necessary to push Amazon forests into a drought regime. Correspondingly, terrestrial NPP increases throughout the tropics between 2000 and 2100 (Figure 5.15c), indicating that increased CO_2 fertilization of vegetation growth overwhelms any constraints on NPP due to climate changes.

As shown in Figure 5.14, NEP in the UVic model plateaus around the year 2050 and declines towards the end of the model simulation. This pattern indicates that the rate at which NPP increases in the model slows in the latter half of the 21^{st} century, largely due to the diminishing effect of CO_2 fertilization at high CO_2 concentrations. Additionally, heterotrophic soil respiration increases exponentially as a function of temperature, and a declining NEP indicates that increases in soil respiration exceed increases in NPP over this period. Figure 5.16 shows the spatial distribution of NEP changes in the model from 2000 to 2050 (a) and from 2050 to 2100 (b). From 2000 to 2050, NEP increases virtually everywhere in the model, consistent with the

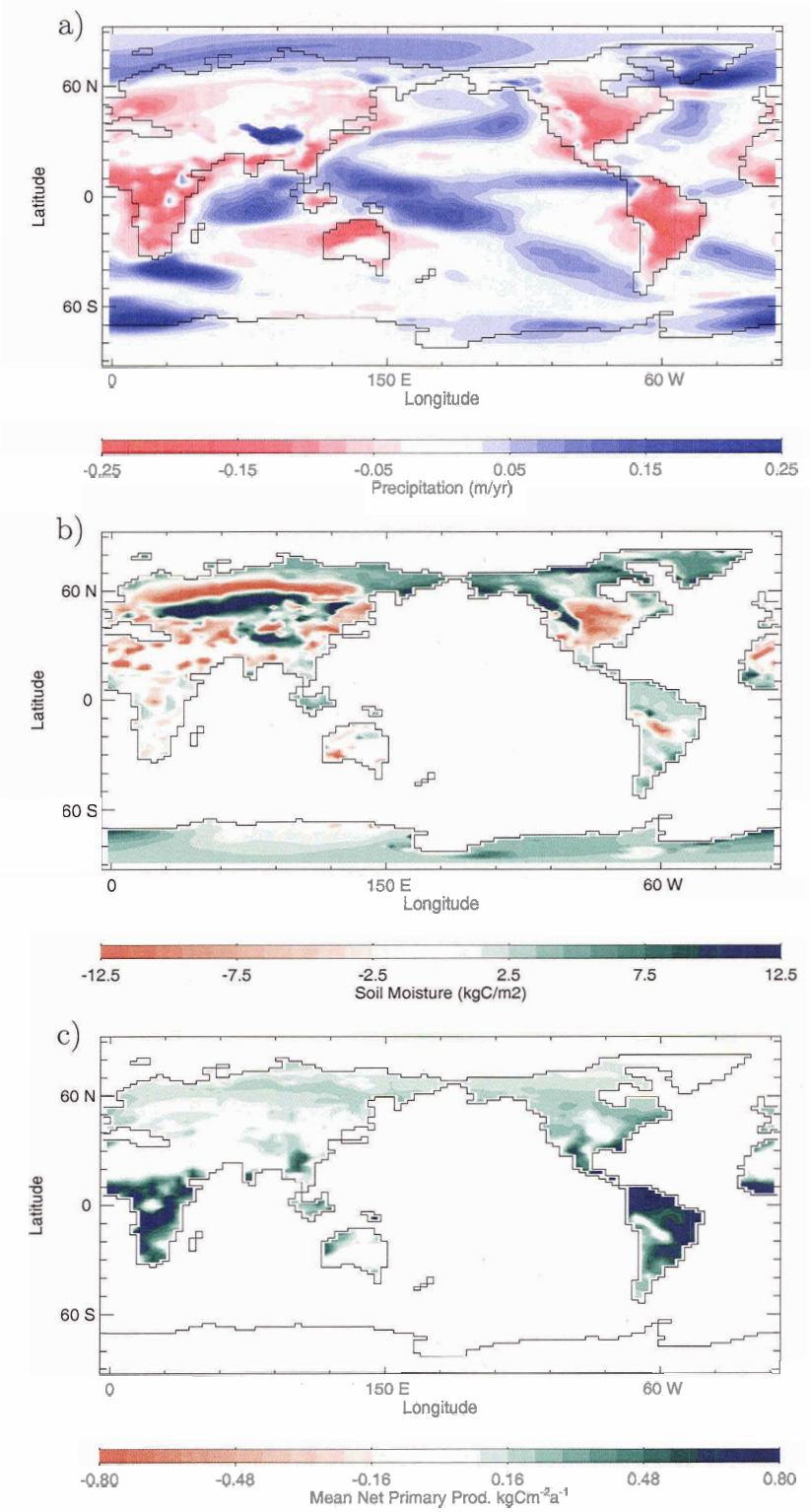

Figure 5.15: **Changes from 2000 to 2100 in (a) modelled precipitation, (b) soil moisture and (c) NPP from the A2 scenario run with non-CO_2 greenhouse gas forcing included.**

global trend shown in Figure 5.14. From 2050 to 2100, the NEP trend in the tropics is reversed, indicating a declining terrestrial sink in these regions. Though NEP declines in the latter half of the 21^{st} century, it remains predominantly positive (Figure 5.16c) indicating continued terrestrial carbon uptake.

In the Hadley simulations, NEP began to decline early in the 21^{st} century and reached zero around 2050, at which point vegetation and soil carbon pools began to lose carbon to the atmosphere. Decreasing NPP occurred as a result of declines in vegetation productivity from increased moisture stress and increasing plant respiration at high temperatures. Declines in vegetation productivity resulted in a decreased transfer of carbon through litterfall to the soil carbon pool, and in combination with temperature-enhanced soil respiration, this led to a large decrease in soil carbon (Cox et al. 2000, 2001). In the UVic model simulations, global vegetation carbon increases throughout the model simulation (as shown in Figure 5.6). As a result, carbon transfer through litterfall to soil carbon pools also increases, and the continued flux of carbon from vegetation to soil exceeds any temperature-driven soil respiration increases, leading to a continued soil carbon increase throughout the model simulation. The fact that the UVic model does not simulate large climatically-induced vegetation productivity decreases, necessitates a continued land carbon sink throughout the 21^{st} century.

It should be noted that the differences in modelled climatic conditions between the UVic and HadCM3C models are not simply a consequence of the reduced complexity of the UVic ESCM's atmosphere. Different general circulation models project widely varying climate conditions for the 21^{st} century (Houghton et al. 2001), and it would be expected that the response of the terrestrial carbon cycle to climate changes would vary depending on the climate model used. A recent study by Cramer et al. (2004) addressed this question by forcing the Lund-Potsdam-Jena (LPJ) dynamic vegetation model offline by 21^{st} century climate change scenarios from four different

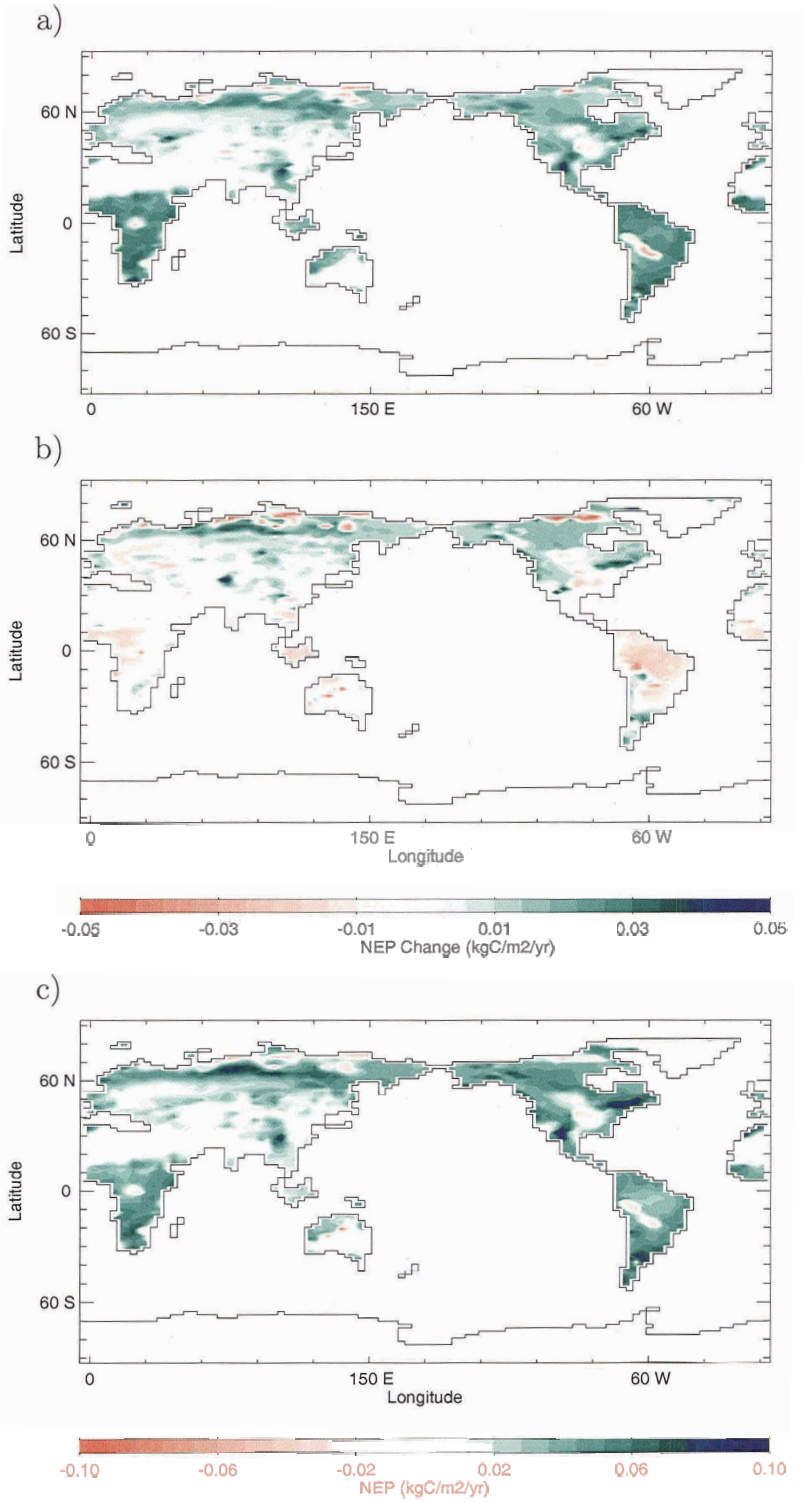

Figure 5.16: (a) NEP change from 2000 to 2050, (b) NEP change from 2050 to 2100 and (c) NEP at the year 2100, simulated by the A2 scenario run with non-CO_2 greenhouse gas forcing included.

climate models (HadCM3, ECHAM, CSIRO and CGCM1). When forced by HadCM3 climate changes, the LPJ model reproduced the die-back of Amazonian forests that was simulated by the TRIFFID model in Cox et al. (2000), indicating that this result is independent of the specific vegetation model used. However, this result was not reproduced when the LPJ model was forced by output from the other three climate models, and in two cases, Amazon forests increased in response to 21^{st} century climate changes. It can be concluded that the response of terrestrial vegetation to climate changes is highly sensitive to regional variation in simulated temperature and precipitation changes. The simulated vegetation response in the UVic model is well within the range of the results reported in Cramer et al. (2004).

5.4 Conclusions

This chapter makes use of the UVic ESCM as coupled interactively to a global carbon cycle model. In Section 5.3.1, I presented the results of model simulations of the 20^{th} century, forced by observed anthropogenic emissions from fossil fuel combustion and land cover change. These results are consistent with observational and model-based evidence of the behaviour of the global carbon cycle over the past two decades, and provide specific information from a modelling perspective on the ability of the terrestrial biosphere to take up anthropogenic CO_2. Furthermore, the UVic model was able to reproduce historical patterns of atmospheric CO_2 accumulation without the use of a biological ocean carbon cycle. This finding suggests that the assumption of constant biological ocean carbon cycle that does not play a large role in the uptake of anthropogenic CO_2, is a reasonable one to make in this study.

The results presented in Section 5.3.2 expand upon those presented in studies by Cox et al. (2000) and Dufresne et al. (2002), describing the behaviour of the carbon cycle in the coming century. Under six SRES projections of future CO_2 emissions,

the UVic model generated a range of climate scenarios showing continued increases in both land and ocean carbon sinks throughout the 21^{st} century. In particular, all simulations showed a sustained terrestrial carbon sink, although the evolution of annual terrestrial fluxes did vary between scenarios. Analysis of land and ocean uptake, as a fraction of anthropogenic emissions, highlighted a weakening of the terrestrial carbon sink relative to the ocean towards the end of the century.

Although I used the same vegetation model and a very similar land-surface model as Cox et al. (2000), our results are quite different; in particular, I was unable to reproduce the die-back of Amazonian forests or the terrestrial carbon sink-to-source transition seen in the 21^{st} century in Cox et al.'s (2000) simulations. The UVic model did simulate a positive feedback between the carbon cycle and climate, much of which can be attributed to declining terrestrial carbon uptake under increased global temperatures. This result is consistent with both Cox et al. (2000) and Dufresne et al. (2002), although the magnitude of the positive feedback in the UVic model is closer to that found by Dufresne et al. (2002). I showed that including non-CO_2 greenhouse gas forcing (as done by Cox et al. (2000)) and increasing the UVic model's climate sensitivity did increase the strength of this feedback, but I was nevertheless unable to reproduce the magnitude of the feedback found by Cox et al. (2000). Based on these results, I argue that the primary reason for the disparity with Cox et al.'s (2000) findings lies in the differences in model-simulated climate change over the coming century, notably regional changes in the hydrological cycle. In particular, I contend that large reductions in terrestrial productivity (as exemplified by the Amazon die-back in Cox et al.'s (2000) simulations) would be necessary to enable a terrestrial carbon sink-to-source transition in the coming century.

While the behaviour of the global carbon cycle in the coming century remains a subject open to debate, modelling studies are beginning to illuminate some of the outstanding areas of uncertainty in projections of future climate change. The

results presented here suggest that the terrestrial biosphere will continue to maintain a prominent role in the climate system, and has the potential to mitigate the effects of human-induced climate change. Given this result, it is vital that all attempts are made to preserve the ability of the terrestrial biosphere to absorb anthropogenic CO_2 by reducing the destructive influence of human activities on biological ecosystems around the world.

Chapter 6

Conclusions

In this dissertation, I have presented model simulations using the UVic Earth System Climate Model, to explore some of the interactions between human activities, terrestrial vegetation and climate change. These simulations have aimed to contribute to the scientific understanding of the effects of historical land cover change on climate, the role of natural and anthropogenic forcing of climate over the past 300 years, the importance of dynamic terrestrial vegetation as a positive feedback to climate, and the behaviour of the terrestrial carbon cycle under past and future climate change.

In Chapter 3, I assessed the role of anthropogenic land cover change as a contributor to the forcing of historical climate change. I found that the biogeophysical effects of changing land cover types are primarily due to surface albedo changes that have resulted from conversion of natural vegetation to croplands and pasture. Furthermore, surface albedo changes have an enhanced effect where human land cover changes have overlapped with areas of seasonal snow cover, as surface albedo changes are amplified by changes in vegetation snow-masking depths. I also found that changes in vegetation evapotranspiration are of secondary importance to global temperature, although regional effects on precipitation are notable. Global temperature changes associated with land cover changes over that past 300 years were found to vary from –0.06 to –0.22 °C for the range of land cover change datasets and model configurations used.

In this chapter, a global carbon cycle model was also used to assess the biogeochemical influence of historical land cover change on climate. By specifying CO_2 emissions from land cover change, it was found that 20^{th} century warming was increased

by 0.3 °C compared to the case where only fossil fuel emissions were considered. Combining this result with the biogeophysical cooling estimates determined previously, I concluded with an estimate that the net effect of historical land cover change has resulted in a warming of about 0.15 °C since 1850.

Chapter 4 incorporated a series of natural and anthropogenic climate forcings into simulations of the past 300 years to reproduce historical temperature records. The natural forcings considered were volcanic sulphate aerosols, solar orbital changes and solar insolation variability. Anthropogenic forcings included historical land cover change, greenhouse gases and tropospheric sulphate aerosols. These simulations revealed that although historical land cover change forcing is small in comparison to other anthropogenic forcings (and as such is not statistically detectable in 20^{th} century observations), it is of comparable magnitude to natural forcings such as solar insolation variability. In addition, the combination of all model forcings resulted in a good simulation of 20^{th} century temperature observations. Simulations forced by only anthropogenic and only natural climate forcings supported other published research in concluding that climate warming in the last several decades can only be simulated by incorporating anthropogenic emissions of greenhouse gases, whereas climate changes in the early portion of the 20^{th} century are likely to have been caused by a combination of natural and anthropogenic climate forcing.

This chapter also introduced a dynamic vegetation model coupled interactively to the UVic ESCM. Natural and anthropogenic climate forcings were used with this new version of the model to assess the role of vegetation as a dynamic feedback to climate. In the case of the all-forcings transient run, I found that dynamic vegetation amplified 20^{th} century warming by about 0.1 °C. When the model was forced by land cover changes alone, the resultant cooling was amplified by about 30%. In this case, I showed that the mechanism behind this magnification lies in high northern latitude vegetation changes and the resultant surface albedo changes. I also presented an

equilibrium simulation that indicated that the feedback between vegetation dynamics and climate takes several centuries of model simulation to achieve its full effect.

Finally, in Chapter 5, I analysed the behaviour of the terrestrial carbon cycle using an interactively coupled climate and carbon cycle model. Simulations from 1750 to 2000 forced by observed emissions of carbon dioxide (from fossil fuels, land-use change and from the decay of anthropogenic methane) revealed that the UVic ESCM does a good job of simulating the observed atmospheric CO_2 increase. Comparison with available data on land and ocean uptake of anthropogenic carbon indicated that the model is consistent with the observed behaviour of ocean and terrestrial carbon sinks for recent decades. The mechanisms behind the observed terrestrial carbon sink are highly uncertain, however, and it is not clear to what extent the effect of CO_2 fertilization on modelled terrestrial uptake reflects actual terrestrial uptake mechanisms.

I also performed simulations of the 21^{st} century using six SRES emissions scenarios to specify future emissions of carbon dioxide. These simulations resulted in a temperature increase over the next hundred years in the range of 1.4 to 3 °C, with simulated atmospheric CO_2 at the year 2100 falling between 500 and 885 ppmv. Both land and ocean carbon sinks continued to play important (and approximately equal) roles in taking up anthropogenic carbon, although there was some indication that the terrestrial biosphere weakens as a carbon sink toward the end of the century. There was no transition, however, from a terrestrial carbon sink to a carbon source.

Analysis of carbon cycle feedbacks revealed a small positive feedback between climate and the terrestrial carbon cycle. The notion of a positive carbon cycle feedback is consistent with previously published studies, although the UVic model does not reproduce the large positive feedback found in previous simulations that used the same terrestrial carbon cycle model (Cox et al. 2000). Inclusion of additional greenhouse gas forcing in the UVic model, and increasing the model's climate sen-

sitivity, increased the strength of the carbon cycle-climate feedback, but I was still unable to reproduce the results shown by Cox et al. (2000). While differences in the magnitude of simulated feedbacks between models have previously been attributed to differences in the terrestrial carbon cycle models, this conclusion is not supported by my research. I argue that differences in results stem primarily from differences in simulated 21^{st} century climate changes, notably changes in the hydrological cycle. In particular, I argue that large climatically-induced decreases in vegetation productivity play a key role in the carbon cycle-climate feedback, and are necessary to enable a terrestrial carbon source-to-sink transition during the 21^{st} century.

Taken collectively, these simulations highlight the important role that terrestrial ecosystems have played, and will likely continue to play, in the global climate system. It is evident that human modification of natural ecosystems has had a substantial impact on climate, and that biogeophysical changes have only partially offset the contribution that land-use change emissions of CO_2 have made to recent climate warming. In addition, it is possible that anthropogenic land cover change could hamper the ability of the terrestrial biosphere to act as a buffer to anthropogenic emissions of carbon dioxide.

Vegetation distributions can also be expected to change in response to climate change, and it is not clear how well ecosystems will be able to adapt to the combined pressure of human land-use and changing climatic conditions. Given the importance of terrestrial vegetation carbon sinks as a moderating force under present anthropogenic emissions, it is likely that this role will continue into the future. It is also evident that there is a substantial range of possible climate futures that depend primarily on the ability and the will of industrial human society to reduce future emissions of greenhouse gases, and secondarily on the character of feedbacks within the climate system.

Further research is required to resolve the remaining uncertainties in the behaviour

of the terrestrial carbon cycle in the future and to reconcile research presented here with other published modelling results. It is clear, however, that terrestrial ecosystems play a vital role as a carbon sink in the climate system and that preserving this capacity by reducing other human pressures on these ecosystems is of utmost importance as we move into a century of unprecedented anthropogenic climate change.

Bibliography

Adams, J. M. and G. Piovesan (2002). Uncertainties in the role of land vegetation in the carbon cycle. *Chemosphere*, 49: 805–819.

Bauer, E., M. Claussen and V. Brovkin (2003). Assessing climate forcings of the Earth system for the past millenium. *Geophys. Res. Lett.*, 30: 1296.

Berger, A. L. (1978). Long-term variations of daily insolation and quaternary climate change. *J. Atmos. Sci.*, 35: 2362–2367.

Berthelot, M., P. Friedlingstein, P. Ciais, P. Monfray, J. L. Dufresne, H. Le Treut and L. Fairhead (2002). Global response of the terrestrial biosphere to CO_2 and climate change using a couple climate-carbon cycle model. *Global Biogeochem. Cy.*, 16: 1084.

Bertrand, C., M. France Loutre, M. Crucifix and A. Berger (2002). Climate of the last millennium: a sensitivity study. *Tellus*, 54A: 221–244.

Betts, R. A. (2000). Offset of the potential carbon sink from boreal forestation by decreases in surface albedo. *Nature*, 408: 187–190.

Betts, R. A. (2001). Biogeophysical impacts of land use on present-day climate: near surface temperature and radiative forcing. *Atmos. Sci. Lett.*, 1: doi:10.1006/asle.2001.0023.

Bitz, C. M., M. M. Holland, A. J. Weaver and M. Eby (2001). Simulating the ice-thickness distribution in a coupled climate model. *J. Geophys. Res.*, 106: 2441–2464.

Bolin, B., R. Sukumar, P. Ciais, W. Cramer, P. Jarvis, H. Kheshgi, C. Nobre, S. Semenov and W. Steffen (2000). Global perspective. In Watson, R. T. et al., eds., *Land Use, Land-Use Change, And Forestry: A Special Report of the Intergovernmental Panel on Climate Change*, 23–51. Camb. Univ. Press.

Bopp, L., C. Le Quéré, M. Heinmann, A. C. Manning and P. Monfray (2002). Climate-induced oceanic oxygen fluxes: Implications for the contemporary carbon budget. *Global Biogeochem. Cy.*, 16: 1022.

Bounoua, L., R. DeFries, G. Collatz, P. Sellers and H. Khan (2002). Effects of land cover conversion on surface climate. *Climatic Change*, 52: 29–64.

Bousquet, P., P. Peylin, P. Ciais, C. Le Quéré, P. Friedlingstein and P. P. Tans (2000). Regional changes in carbon dioxide fluxes of land and oceans since 1980. *Science*, 290: 1342–1346.

Briegleb, B., P. Minnis, V. Ramanathan and E. Harrison (1986). Comparison of regional ckear-sky albedos inferred from satellite observations and model comparisons. *J. Climate Appl. Meteor.*, 25: 214–226.

Brovkin, V., A. Ganopolski, M. Claussen, C. Kubatzki and V. Petoukhov (1999). Modelling climate response to historical land cover change. *Global Ecol. Biogeogr.*, 8: 509–517.

Brutsaert, W. (1982). *Evaporation into the Atmosphere*. D. Reidel, Boston.

Charlson, R., J. Langner, H. Rodhe, C. Leovt and G. Warren (1991). Perturbation of the Northern Hemisphere radiative balance by backscattering from anthropogenic sulfate aerosols. *Tellus*, 43AB: 152–163.

Chase, T., R. Pielke, T. Kittel, R. Nemani and S. Running (2000). Simulated impacts of historical land cover changes on global climate in northern winter. *Clim. Dynam.*, 16: 93–105.

Chase, T., R. Pielke, T. Kittel, M. Zhao, A. Pitman, S. Running and R. Nemani (2001). Relative climatic effects of landcover change and elevated carbon dioxide combined with aerosols: A comparison of model results and observations. *J. Geophys. Res.*, 106: 31,685–31,691.

Clapp, R. B. and G. M. Hornberger (1978). Empirical equations for some soil hydraulic properties. *Water Resour. Res.*, 14: 601–604.

Claussen, M., V. Brovkin and A. Ganopolski (2001). Biogeophysical versus biogeochemical feedbacks of large-scale land cover change. *Geophys. Res. Lett.*, 28: 1011–1014.

Collatz, G. T., J. T. Ball, C. Grivet and J. A. Berry (1991). Physiological and environmental regulation of stomatal conductance, photosynthesis and transpiration. *Agric. and Forest Meteorol.*, 54: 107–136.

Collatz, G. T., M. Ribas-Carbo and J. A. Berry (1992). A coupled photosynthesis-stomatal conductance model for leaves of C_4 plants. *Aus. J. Plant Physiol.*, 19: 519–538.

Cowling, S. A., R. A. Betts, P. M. Cox, V. J. Ettwein, C. D. Jones, M. A. Maslin and S. A. Spall (2004). Contrasting simulated past and future responses of the Amazonian forest to atmospheric change. *Phil. Trans. R. Soc. Lond.*, 359: 539–547.

Cox, P. M. (2001). Description of the "TRIFFID" dynamic global vegetation model. In *Technical Note 24*. Hadley Center, Met Office.

Cox, P. M., R. Betts, C. Bunton, R. Essery, P. Rowntree and J. Smith (1999). The impact of new land surface physics on the GCM simulation of climate and climate sensitivity. *Clim. Dynam.*, 15: 183–203.

Cox, P. M., R. A. Betts, C. D. Jones, S. A. Spall and I. J. Totterdell (2000). Acceleration of global warming due to carbon-cycle feedbacks in a coupled climate model. *Nature*, 408: 184–187.

Cox, P. M., R. A. Betts, C. D. Jones, S. A. Spall and I. J. Totterdell (2001). Modelling vegetation and the carbon cycle as interactive elements of the climate system. In *Technical Note 23*. Hadley Center, Met Office.

Cramer, W., A. Bondeau, S. Schaphoff, W. Lucht, B. Smith and S. Sitch (2004). Tropical forests and the global carbon cycle: impacts of atmospheric carbon dioxide, climate change and rate of deforestation. *Phil. Trans. R. Soc. Lond.*, 359: 331–343.

Cramer, W., A. Bondeau, F. I. Woodward, I. C. Prentice, R. A. Betts, V. Brovkin, P. M. Cox, V. Fisher, J. A. Foley, A. D. Friend, C. Kucharik, M. R. Lomas, N. Ramankutty, S. Sitch, B. Smith, A. White and C. Young-Molling (2001). Global response of terrestrial ecosystem structure and function to CO_2 and climate change: results from six dynamic global vegetation models. *Glob. Change Biol.*, 7: 357–373.

Crowley, T. J. (2000). Causes of climate change over the past 1000 years. *Science*, 289: 270–277.

DeFries, R. and J. Townsend (1994). NDVI-derived land cover classification at global scales. *Int. J. Rem. Sen.*, 15: 3567–3586.

Dickinson, R. E. (2001). Biosphere-Atmosphere Transfer Scheme (BATS) version 1e as coupled to the NCAR Community Climate Model. *NCAR Technical Note NCAR TN 387 STR.*

Dufresne, J.-L., P. Friedlingstein, M. Berthelot, L. Bopp, P. Ciais, L. Fairhead, H. L. Treut and P. Monfray (2002). On the magnitude of positive feedback between future climate change and the carbon cycle. *Geophys. Res. Lett.*, 29: 1405.

Etheridge, D. M., L. P. Steele, R. L. Langenfelds, R. J. Francey, J.-M. Barnola and V. I. Morgan (1998). Historical CO_2 record from the Law Dome DE08, DE08-2, and DSS ice cores. In *Trends Online: A Compendium of Data on Global Change.* Carbon Dioxide Information Analysis Center.

Ewen, T. L., A. J. Weaver and M. Eby (2004). Sensitivity of the inorganic ocean carbon cycle to future climate warming in the UVic coupled model. *Atmos. Ocean*, 42: 23–42.

Flato, G. M. and G. J. Boer (2001). Warming asymmetry in climate change simulations. *Geophys. Res. Lett.*, 23: 195–198.

Folland, C. K., N. A. Rayner, S. J. Brown, S. S. P. S. T. M. Smith, D. E. Parker, I. Macadam, P. D. Jones, R. N. Jones, N. Nicholls and D. M. H. Sexton (2001). Global temperature change and its uncertainties since 1861. *Geophys. Res. Lett.*, 28: 2621–2624.

Friedlingstein, P., L. Bopp, P. Ciais, J.-L. Dufresne, L. Fairhead, H. LeTreut, P. Monfray and J. Orr (2001). Positive feedback between future climate change and the carbon cycle. *Geophys. Res. Lett.*, 28: 1543–1546.

Friedlingstein, P., J.-L. Dufresne, P. M. Cox and P. Rayner (2003). How positive is the feedback between future climate change and the carbon cycle? *Tellus*, 55B: 692–700.

Gill, A. E. (1982). *Atmosphere-Ocean Dynamics.* Academic Press, New York.

Govindasamy, B., P. Duffy and K. Caldeira (2001). Land use change and Northern Hemisphere cooling. *Geophys. Res. Lett.*, 28: 291–294.

Graves, C. E., W. Ho Lee and G. R. North (1993). New parameterizations and sensitivities for simple climate models. *J. Geophys. Res.*, 98: 5025–5036.

Gurney, K. R., R. M. Law, A. S. Denning, P. J. Rayner, D. Baker, P. Bousquet, L. Bruhwiler, Y.-H. Chen, P. Ciais, S. Fan, I. Y. Fung, M. Gloor, M. Heimann, K. Higuchi, J. John, T. Maki, S. Maksyutov, K. Masarie, P. Peylin, M. Prather, B. C. Pak, K. Randerson, J. Sarmiento, S. Taguchi, T. Takahashi and C.-W. Yuen (2002). Towards robust regional estimates of CO_2 sources and sinks using atmospheric transport models. *Nature*, 415: 626–630.

Haney, R. L. (1971). Surface thermal boundary conditions for ocean circulation models. *J. Phys. Ocean*, 1: 241–248.

Hansen, J. E., M. Sato, A. Lacis, R. Ruedy, I. Tegen and E. Matthews (1998). Climate forcings in the industrial era. *P. Natl. Acad. Sci. USA.*, 95: 12,753–12,758.

Hegerl, G. C., T. J. Crowley, S. K. Baum, K. Yul Kim and W. T. Hyde (2003). Detection of volcanic, solar and greenhouse gas signals in paleo-reconstructions of Northern Hemispheric temperature. *Geophys. Res. Lett.*, 30: 1242.

Houghton, J., Y. Ding, D. Griggs, M. Noguer, P. van der Linden, X. Dai, K. Maskell and C. Johnson, eds. (2001). *Climate Change 2001: The Scientific Basis*. Camb. Univ. Press, 944 pp.

Houghton, J., L. Meira Filho, B. Callander, N. Harris, A. Kattenberg and K. Maskell, eds. (1996). *Climate Change 1995: The Science of Climate Change*. Camb. Univ. Press, 592 pp.

Houghton, R. (2003a). Revised estimates of the annual net flux of carbon to the atmosphere from changes in land use and land management 1850–2000. *Tellus*, 55B: 378–390.

Houghton, R. (2003b). Why are estimates of the terrestrial carbon balance to different? *Glob. Change Biol.*, 9: 500–509.

House, J. I., I. C. Prentice, N. Ramankutty, R. A. houghton and M. Heimann (2003). Reconciling apparent inconsistencies in estimates of terrestrial CO_2 sources and sinks. *Tellus*, 55B: 354–363.

Johns, T., J. Gregory, W. Ingram, C. Johnson, A. Jones, J. Lowe, J. Mitchell, D. Roberts, D. Sexton, D. Stevenson, S. Tett and M. Woodage (2003). Anthropogenic climate change for 1860 to 2100 simulated with the HadCM3 model under updated emissions scenarios. *Clim. Dynam.*, 20: 583–612.

Jones, G. S., S. F. Tett and P. A. Stott (2003). Causes of atmospheric temperature change 1960–2000: A combined attribution analysis. *Geophys. Res. Lett.*, 30: 1228.

Jones, P. (1993). Hemispheric surface air temperature variations: a reanalysis and update to 1993. *J. Clim.*, 7: 1794–1802.

Joos, F., R. Meyer, M. Bruno and M. Leuenberger (1999). The variability in the carbon sinks as reconstructed for the last 1000 years. *Geophys. Res. Lett.*, 10: 1437–1440.

Kalnay, E., M. Kanamitsu, R. Kistler, W. Collins, D. Deaven, L. Gandin, M. Iredell, S. Saha, G. White, J. Woolen, Y. Zhu, M. Chelliah, W. Ebisuzaki, W. Higgins, J. Janowiak, K. C. Mo, C. Ropelewski, J. Wang, A. Leetma, R. Reynolds, R. Jenne and D. Joseph (1996). The NCEP/NCAR 40-year reanalysis project. *Bull. Am. Meteorol. Soc.*, 77: 437–471.

Karnosky, D. F. (2003). Impacts of elevated atmospheric CO_2 on forest trees and forest ecosystems: knowledge gaps. *Environment International*, 29: 161–169.

Keeling, C. D., T. P. Whorf et al. (2003a). Atmospheric CO_2 concentrations (ppmv) derived from flask and in situ air samples collected at the South Pole. In *Trends Online: A Compendium of Data on Global Change*. Carbon Dioxide Information Analysis Center.

Keeling, C. D., T. P. Whorf et al. (2003b). Atmospheric CO_2 concentrations (ppmv) derived from in situ air samples collected at Mauna Loa Observatory, Hawaii. In *Trends Online: A Compendium of Data on Global Change*. Carbon Dioxide Information Analysis Center.

Klein Goldewijk, K. (2001). Estimating global land use change over the past 300 years: the HYDE database. *Global Biogeochem. Cy.*, 15: 415–433.

Koch, D. (2001). Transport and direct radiative forcing of carbonaceous and sulfate aerosols in the GISS GCM. *J. Geophys. Res.*, 106: 20,311–20,332.

Lean, J., J. Beer and R. Bradley (1995). Reconstruction of solar irradiance since 1610: Implications for climate change. *Geophys. Res. Lett.*, 22: 3195–3198.

Levy, P. E., M. G. R. Cannell and A. D. Friend (2004). Modelling the impact of future changes in climate, CO_2 concentration and land use on natural ecosystems and the terrestrial carbon sink. *Global Environmental Change*, 14: 21–30.

Malhi, Y., P. Meir and S. Brown (2002). Forests, carbon and global climate. *Phil. Trans. R. Soc. Lond.*, 360: 1567–1591.

Manabe, S. (1969). Climate and the ocean circulation 1. The atmospheric circulation and the hydrology of the earth's surface. *Mon. Weather Rev.*, 97: 739–774.

Mann, M., R. Bradley and M. Hughes (1999). Northern Hemisphere temperature during the past millenium: inferences, uncertainties and limitations. *Geophys. Res. Lett.*, 26: 759–762.

Mann, M. E. and P. D. Jones (2003). Global surface temperatures over the past two millennia. *Geophys. Res. Lett.*, 30: 1820.

Marland, G., T. Boden and R. Andres (2002). Global, regional, and national annual CO_2 emissions from fossil-fuel burning, cement production, and gas flaring: 1751-1999. In *CDIAC NDP-030*. Carbon Dioxide Information Analysis Center.

Matthews, E. (1983). Global vegetation and land use: new high-resolution data bases for climate studies. *J. Clim. Appl. Meterol.*, 22: 474–487.

Matthews, H. D., A. J. Weaver, M. Eby and K. J. Meissner (2003). Radiative forcing of climate by historical land cover change. *Geophys. Res. Lett.*, 30: 1055.

Matthews, H. D., A. J. Weaver and K. J. Meissner (2004a). Terrestrial carbon cycle dynamics under recent and future climate change. *Submitted to: J. Clim.*.

Matthews, H. D., A. J. Weaver, K. J. Meissner, N. P. Gillett and M. Eby (2004b). Natural and anthropogenic climate change: incorporating historical land cover change, vegetation dynamics and the global carbon cycle. *Clim. Dynam.*, 22: 461–479.

McGuire, A., S. Sitch, J. Clein, R. Gargaville, G. Esser, J. Foley, M. Heimann, F. Joos, J. Kaplan, D. Kicklighter, R. Meier, J. Melillo, B. Moore III, I. Prentice, N. Ramankutty, T. Reichenau, A. Schloss, H. Tian, L. Williams and U. Wittenberg (2001). Carbon balance of the terrestrial biosphere in the twentieth century: analysis of CO_2, climate and land use effects with four process-based ecosystem models. *Global Biogeochem. Cy.*, 15: 183–206.

Meissner, K. J., A. J. Weaver, H. D. Matthews and P. M. Cox (2003). The role of land-surface dynamics in glacial inception: a study with the UVic Earth System Climate Model. *Clim. Dynam.*, 21: 515–537.

Melillo, J. M., P. A. Steudler, J. D. Aber, K. Newkirk, H. Lux, F. P. Bowles, C. Catricala, A. Magill, T. Ahrens and S. Morrisseau (2002). Soil warming and carbon-cycle feedbacks to the climate system. *Science*, 298: 2173–2176.

Myhre, G. and A. Myhre (2003). Uncertainties in radiative forcing due to surface albedo changes caused by land-use changes. *J. Clim.*, 19: 1511–1524.

Nakićenović, N., J. Alcamo, G. Davis, B. de Vries, J. Fenhann, S. Gaffin, K. Gregory, A. Grübler, T. Yong Jung, T. Kram, E. Lebre La Rovere, L. Michaelis, S. Mory, T. Morita, W. Pepper, H. Pitcher, L. Price, K. Riahi, A. Roehrl, H.-H. Rogner, A. Sankovski, M. Schlesinger, P. Shukla, S. Smith, W. Swart, S. van Rooijen, N. Victor and Z. Dadi (2000). *Special Report on Emissions Scenarios*. Cambridge University Press, Cambridge, 570 pp.

Nemani, R. R., C. D. Keeling, H. Hashimoto, W. M. Jolly, S. C. Piper, C. J. Tucker, R. B. Myneni and S. W. Running (2003). Climate-driven increases in global terrestrial net primary productivity from 1982 to 1999. *Science*, 300: 1560–1463.

Oren, R., D. S. Ellsmorth, K. H. Johnsen, N. Phillips, B. E. Ewers, C. Maier, K. V. Schäfer, H. MacCarthy, G. Hendrey, S. G. McNulty and G. G. Katul (2001). Soil fertility limits carbon sequestration by forest ecosystems in a CO_2-enriched atmosphere. *Nature*, 411: 469–472.

Orr, J., C. R. Najjar, C. L. Sabine and F. Joos (1991). *Abiotic-HOWTO. Internal OCMIP Report*. LCSE/CEA Saclay, Gif-sur-Yvette, France, 25 pp.

Pacanowski, R. (1995). *MOM 2 Documentation User's Guide and Reference Manual, GFDL Ocean Group Technical Report*. NOAA, GFDL, Princeton.

Petit, J. R., J. Jouzel, D. Raynaud, J. Barnola, I. Basile, M. Bender, J. Chappellaz, M. Davis, G. Delaygue, M. Delmotte, V. Kotlyakov, M. Legrand, V. Lipenkov, C. Lorius, L. Pépin, C. Ritz, E. Saltzman and M. Stievenard (1999). Climate and atmospheric history of the past 420,000 years from the Vostok ice code, Antarctica. *Nature*, 399: 429–436.

Plattner, G.-K., F. Joos and T. F. Stocker (2002). Revision of the global carbon budget due to changing air-sea oxygen fluxes. *Global Biogeochem. Cy.*, 16: 1096.

Prather, M., D. Ehhalt, F. Dentener, R. Derwent, E. Dlugokencky, E. Holland, I. Isaksin, J. Katima, V. Kirchoff, P. Matson, P. Migley and M. Wang (2001).

Atmospheric chemistry and greenhouse gases. In Houghton, J. et al., eds., *Climate Change 2001: The Scientific Basis*, 239–287. Camb. Univ. Press.

Prentice, C., G. Farquhar, M. Fasham, M. Goulden, M. Heimann, V. Jaramillo, H. Kheshgi, C. Le Quéré, R. Scholes and D. Wallace (2001). The carbon cycle and atmospheric carbon dioxide. In Houghton, J. et al., eds., *Climate Change 2001: The Scientific Basis*, 183–237. Camb. Univ. Press.

Ramankutty, N. and J. A. Foley (1999). Estimating historical changes in land cover: croplands from 1700 to 1992. *Global Biogeochem. Cy.*, 13: 997–1027.

Ramaswamy, V., O. Boucher, J. Haigh, D. Hauglustaine, J. Harwood, G. Myhre, T. Nakajima, G. Shi and S. Solomon (2001). Radiative forcing of climate change. In Houghton, J. et al., eds., *Climate Change 2001: The Scientific Basis*, 349–416. Camb. Univ. Press.

Ramaswamy, V. and C. Chen (1997). Linear additivity of climate response for combined albedo and greenhouse perturbations. *Geophys. Res. Lett.*, 24: 567–570.

Robock, A. (1994). Review of Year Without a Summer? World Climate in 1816. *Climatic Change*, 26: 105–108.

Robock, A. (2000). Volcanic eruptions and climate. *Rev. Geophys.*, 38: 191–219.

Robock, A. and M. Free (1995). Ice cores as an index of global volcanism from 1850 to the present. *J. Geophys. Res.*, 100: 11,549–11,567.

Sato, M., J. Hansen, M. McCormick and J. Pollack (1993). Stratospheric aerosol optical depth, 1980–1990. *J. Geophys. Res.*, 98: 22,987–22,994.

Saugier, B., J. Roy and H. A. Mooney (2001). Estimations of global terrestrial productivity: Converging toward a single number? In Roy, J., B. Saugier and H. Mooney, eds., *Terrestrial global productivity: past present and future*, 543–557. Academic Press.

Schimel, D. S., J. I. House, K. A. Hibbard, P. Bousquet, P. Ciais, P. Peylin, B. H. Braswell, M. J. Apps, D. Baker, A. Bondeau, J. Canadell, G. Churkina, W. Cramer, A. S. Denning, C. B. Field, P. Friedlingstein, C. Goodale, M. Heimann, R. A. Houghton, J. M. Melillo, B. Moore III, D. Murdiyarso, I. Noble, S. W. Pacala, I. C. Prentice, M. R. Raupach, P. J. Rayner, R. J. Scholes, W. L. Steffen and

C. Wirth (2001). Recent patterns and mechanisms of carbon exchange by terrestrial ecosystems. *Nature*, 414: 169–172.

Schlesinger, M. E. and S. Malyshev (2001). Changes in near-surface temperature and sea-level for the post-SRES CO_2-stabilization scenarios. *Integrated Assessment*, 2: 95–199.

Sellers, P., B. Meeson, J. Closs, J. Collatz, F. Corprew, D. Dazlich, F. Hall, Y. Kerr, R. Koster, S. Los, K. Mitchell, J. McManus, D. Myers, K.-J. Sun and P. Try (1996). The ISLSCP initiative I global datasets: Surface boundary conditions and atmospheric forcings for land-atmosphere studies. *B. Am. Meteorol. Soc.*, 77: 1987–2005.

Stern, D. I. and R. K. Kaufmann (1998). Annual estimates of global anthropogenic methane emissions: 1860–1994. In *Trends Online: A Compendium of Data on Global Change*. Carbon Dioxide Information Analysis Center.

Stocker, T., G. Clarke, H. le Treut, R. Lindzen, V. Meleshko, R. Mugura, T. Palmer, R. Pierrehumbert, P. Sellers, K. Tremberth and J. Willebrand (2001). Physical climate processes and feedbacks. In Houghton, J. et al., eds., *Climate Change 2001: The Scientific Basis*, 417–470. Camb. Univ. Press.

Stott, P., S. Tett, G. Jones, M. Allen, W. Ingram and J. Mitchell (2001). Attribution of twentieth century temperature change to natural and anthropogenic causes. *Clim. Dynam.*, 17: 1–21.

Stott, P., S. Tett, G. Jones, M. Allen and J. M. G. Jenkins (2000). External control of twentieth century temperature variations by natural and anthropogenic forcings. *Science*, 290: 2133–2137.

Tegen, I., D. Koch, A. A. Lacis and M. Sato (2000). Trends in tropospheric aerosol loads and corresponding impact on direct radiative forcing between 1950 and 1990: A model study. *J. Geophys. Res.*, 105: 26,971–26,989.

Tett, S. F. B., P. A. Stott, M. R. Allen, W. J. Ingram and J. F. B. Mitchell (1999). Causes of twentieth century temperature change near the Earth's surface. *Nature*, 399: 569–572.

Trudinger, C. M., I. G. Enting, P. J. Rayner and R. J. Francey (2002). Kalman filter analysis of ice core data 2. Double deconvolution of CO_2 and $\delta^{13}C$ measurements. *J. Geophys. Res.*, 107: 4423.

Weaver, A. J., M. Eby, E. C. Wiebe, C. M. Bitz, P. B. Duffy, T. L. Ewen, A. F. Fanning, M. M. Holland, A. MacFadyen, H. D. Matthews, K. J. Meissner, O. Saenko, A. Schmittner, H. Wang and M. Yoshimori (2001). The UVic Earth System Climate Model: Model description, climatology and applications to past, present and future climates. *Atmos. Ocean*, 39: 361–428.

Wilson, M. and A. Henderson-Sellers (1985). A global archive of land cover and soils data for use in general circulation climate models. *J. Climatol.*, 5: 119–143.

Zeng, N., J. D. Neelin, C. Chou, J. Wei-Bing Lin and H. Su (2000). Climate and variability in the first quasi-equilibrium tropical circulation model. In Randall, D. A., ed., *General Circulation Model Development*, 457–488. Academic Press.

Zhao, M., A. Pitman and T. Chase (2001). The impact of land cover change on the atmospheric circulation. *Clim. Dynam.*, 17: 467–477.